# EVAPORATION FROM A CANADIAN WEST COAST DOUGLAS-FIR FOREST: SEASONAL PATTERNS AND CONTROLS

by

**ELYN ROBIN HUMPHREYS**

B.Sc. (Plant Biology), University of Guelph, Guelph, Ontario, Canada, 1997

A THESIS SUBMITTED IN PARTIAL FULFILLMENT OF THE

REQUIREMENTS FOR THE DEGREE OF MASTER OF SCIENCE

in

THE FACULTY OF GRADUATE STUDIES

The Faculty of Agricultural Sciences

We accept this thesis as conforming

to the required standard

THE UNIVERSITY OF BRITISH COLUMBIA

September 1999

In presenting this thesis in partial fulfilment of the requirements for an advanced degree at the University of British Columbia, I agree that the Library shall make it freely available for reference and study. I further agree that permission for extensive copying of this thesis for scholarly purposes may be granted by the head of my department or by his or her representatives. It is understood that copying or publication of this thesis for financial gain shall not be allowed without my written permission.

Department of SOIL SCIENCE

The University of British Columbia
Vancouver, Canada

Date Oct 12, 1999

## ABSTRACT

In order to understand how forest functioning will respond to global climate change, long-term and direct measurements of water vapour and energy exchange over forested ecosystems are needed. Between October 15, 1997 and May 31, 1999, eddy covariance measurements of latent and sensible heat flux were made above a 50-year-old, 33-m tall Douglas-fir forest, part of the seasonal temperate rainforest located on Vancouver Island, B.C, on the west coast of Canada. Winters at this site are wet and mild while summers are warm and dry. Evaporation rates and energy exchange varied widely on annual, seasonal and diurnal time scales and were used to discern the processes involved in the evaporation of water from this forest canopy. Ultimately, these variations were integrally linked to the canopy wetness and the surface conductance.

Spectral analysis and turbulence characteristics were used to ensure measurement quality during inclement weather. The Gill Model 1012R2A sonic anemometer-thermometer used in this study performed well up to rainfall intensities of 4.6 mm $h^{-1}$. However, signal attenuation of the water vapour mixing ratio was observed during high humidity conditions due to water vapour adsorption/desorption effects on the sampling tube walls leading to the infrared gas analyzer. Total latent heat flux losses of up to 38% could be corrected using the sensible heat cospectra.

Significant evaporation rates occurred during the winter months at this site. The wet canopy acted as a sink for energy characterized by downward fluxes of sensible heat supporting evaporation of intercepted rainfall. Latent heat fluxes often exceeded available energy and equilibrium evaporation rates on a half hour basis throughout the day and night. Wet canopy evaporation required turbulent conditions and only a small non-zero saturation deficit.

Evaporation occurring between April and September, inclusively, accounted for 74% of the total annual evaporation of 402 mm for 1998. Summer evaporation rates were on average 1.57 mm $day^{-1}$ with a maximum of 3.56 mm $day^{-1}$. Sensible heat flux dominated energy exchange throughout the summer with $\beta$ values ranging from 1.3 to 3.5. Uncorrected midday Priestly-Taylor $\alpha$ values ranged from 0.20 to 0.55. Physiological control was important in limiting dry canopy evaporation or transpiration rates. Mean daytime canopy conductance was generally less than 6 mm $s^{-1}$ and was closely related to saturation deficit, soil water potential, and photosynthetic photon flux density. However, canopy conductance was found to have a weak negative linear relationship with transpiration rates only during late morning hours.

## TABLE OF CONTENTS

## LIST OF SYMBOLS AND ACRONYMS

| Variable | Units | Description |
|---|---|---|
| $\alpha$ | | ratio of $\lambda E/\lambda E_{eq}$, Priestly-Taylor coefficient |
| $\beta$ | | Bowen ratio, $\beta = H/\lambda E$ |
| $\gamma$ | g $m^{-3}$ °$C^{-1}$ | psychometric constant |
| $\zeta$ | | stability, $\zeta = (z\text{-}d)/L$ |
| $\theta_m$ | $m^3$ $m^{-3}$ | volumetric fraction of mineral soil |
| $\theta_{sat}$ | $m^3$ $m^{-3}$ | saturated volumeteric water content (equivalent to pororsity) |
| $\theta_v$ | $m^3$ $m^{-3}$ | volumetric water content |
| $\lambda$ | J $kg^{-1}$ | latent heat of vaporization |
| $\lambda E$ | W $m^{-2}$ | latent heat flux density |
| $\lambda E_{eq}$ | W $m^{-2}$ | equilibrium latent heat flux density, $\lambda E_{eq} = \frac{s}{(s+\gamma)} R_a$ |
| $\rho$ | kg $m^{-3}$ | density of dry air |
| $\rho_b$ | kg $m^{-3}$ | soil bulk density |
| $\rho_s$ | kg $m^{-3}$ | soil particle density |
| $\rho_t$ | kg $m^{-3}$ | density of wood |
| $\rho_v$ | kg $m^{-3}$ | water vapour density |
| $\sigma_x$ | units of $x$ | standard deviation of $x$ |
| $\sigma^2_x$ | units of $x^2$ | variance of $x$ |
| $\tau$ | N $m^{-2}$ | momentum flux density |
| $\phi_T$ | | non-dimensional variability in $T$ |
| $\phi_w$ | | non-dimensional variability in $w$ |
| $\chi_c$ | µmol $CO_2$/mol moist air | $CO_2$ mol fraction |

| | | |
|---|---|---|
| $\chi_w$ | mmol water vapour/mol dry air | water vapour mixing ratio |
| $\chi_{ww}$ | mmol water vapour/mol moist air | mole fraction of water vapour |
| $\Psi_h$ | | diabatic correction factor for heat and water vapour |
| $\Psi_{leaf}$ | MPa | leaf water potential |
| $\Psi_m$ | | diabatic correction factor for momentum |
| $\Psi_{soil}$ | MPa | soil water potential (specifically, soil matric potential) |
| $\Omega$ | | McNaughton and Jarvis atmospheric decoupling coefficient |
| *a, b, c* | various units | general symbols for various coefficients (these are not exclusive for any given relationship) |
| $c_p$ | J $kg^{-1}$ $°C^{-1}$ | specific heat of air |
| $c_s$ | μmol $mol^{-1}$ | carbon dioxide concentration at the leaf surface |
| $C$ | mm | depth of water stored on canopy |
| $d$ | m | zero-plane displacement, $d$ = 20.55 m |
| $d_{bh}$ | m | tree diameter at breast height |
| $d_i$ | m | tree diameter at height interval $i$ |
| $D$ | kPa | saturation deficit of the air |
| $E$ | mm $h^{-1}$ | rate of total evaporation (includes evaporation of surface water and transpiration) |
| $E_{eq}$ | mm $h^{-1}$ | equilibrium evaporation rate, $E_{eq} = \lambda \frac{s}{(s+\gamma)} R_a$ |
| $E_m$ | mm $h^{-1}$ | empirical coefficient representing maximum evaporation rates, Equation (2.9) |
| $F_f$ | | tree form factor, $F_f$ = 0.49 |
| $g$ | m $s^{-2}$ | acceleration due to gravity, $g$ = 9.8 m $s^{-2}$ |
| $g_c$ | mm $s^{-1}$ | canopy conductance to water vapour |
| $g_m$ | mm $s^{-1}$ | empirical coefficient representing maximum conductance, Equation (2.9) |

| | | |
|---|---|---|
| $g_a$ | mm $s^{-1}$ | aerodynamic conductance for heat and water vapour, $g_a = 1/r_{ah}$ |
| $g_s$ | mm $s^{-1}$ | stomatal conductance to water vapour |
| $G$ | W $m^{-2}$ | soil heat flux density |
| $H$ | W $m^{-2}$ | sensible heat flux density |
| $h$ | m | canopy height, $h$ = 33 m |
| h | | hour in Pacific Standard Time (PST) |
| $J$ | W $m^{-2}$ | rate of total energy storage in the air and the forest biomass, $J = S_h + S_l + S_{nb} + S_t$ |
| $J_p$ | W $m^{-2}$ | rate of energy consumed in photosynthesis |
| $k$ | | von Karman constant, $k$ = 0.4 |
| $L$ | m | Obukhov scaling length |
| $n$ | Hz | frequency |
| $p$ | mm | proportion of rainfall which is not intercepted by the forest canopy or stems, "free" throughfall coefficient |
| $P$ | mm/30 min | rates of gross rainfall (precipitation) |
| $P_d$ | mm/30 min | rates of drainage from the canopy |
| $P_{st}$ | mm/30 min | rate of stemflow |
| $P_{th}$ | mm/30 min | rate of throughfall |
| $Q$ | μmol $m^{-2}$ $s^{-1}$ | photosynthetic photon flux density |
| $r$ | m | radius |
| $r_a$ ($r_{a,h}$) | s $m^{-1}$ | aerodynamic resistance for heat and water vapour |
| $r_{a,m}$ | s $m^{-1}$ | aerodynamic resistance for momentum |
| $R_a$ | W $m^{-2}$ | available energy flux density , $R_a = R_n - G - J$ |
| $R_n$ | W $m^{-2}$ | net radiation flux density |
| s | | time: seconds |
| $s$ | g $m^{-3}$ °$C^{-1}$ | change of saturation density with temperature |
| $S$ | mm | canopy water storage capacity |
| $S\downarrow$ | W $m^{-2}$ | global solar radiation |
| $S_x(n)$ | units of variance/Hz | spectral energy density of variable $x$ at frequency $n$ |

| | | |
|---|---|---|
| $S_{wx}(n)$ | units of variance/Hz | cospectral energy density of variable $w$ and $x$ at frequency $n$ |
| $S_D$ | stems $ha^{-1}$ | stand density = 1054 stems $ha^{-1}$ |
| $S_h$ | W $m^{-2}$ | rate of sensible heat storage in the air between 0 m and z = 42.7 m |
| $S_l$ | W $m^{-2}$ | rate of latent heat storage in the air between 0 m and z = 42.7 m |
| $S_{nb}$ | W $m^{-2}$ | rate of heat storage in the needles and branches |
| $S_t$ | W $m^{-2}$ | rate of heat storage in the tree boles |
| $t$ | s, h, min | time (All times are Pacific Standard Time) |
| $T$ | °C | air temperature |
| $T_s$ | °C | soil temperature |
| $T_e$ | | empirical transfer function |
| $T_t$ | °C | bole annulus temperature |
| $T_v$ | °C | virtual temperature |
| $u$ | m $s^{-1}$ | streamwise wind speed, or average horizontal wind speed at measurement height, $z$ |
| $u_*$ | m $s^{-1}$ | friction velocity, $u_* = \left[\overline{u'w'}^2 + \overline{v'w'}^2\right]^{1/2}$ |
| $v$ | m $s^{-1}$ | cross-streamwise wind speed |
| $w$ | m $s^{-1}$ | vertical wind speed |
| $x$ | m | distance |
| $z$ | m | eddy covariance flux measurement height, $z$ = 42.7 m |
| $z_{o,h}$ | m | roughness length for heat and water vapour |
| $z_o$ | m | roughness length for momentum, $z_o$ = 3.3 m |
| $\frac{(1/Q_o)dQ}{dx}$ | | relative flux density for footprint analysis |
| s.d. | | standard deviation |
| HMP | | Vaisala humidity sensor |
| IRGA | | Infrared gas analyzer |
| LAI | $m^2$ $m^{-2}$ | projected one-sided leaf area index, LAI ≅ 4 $m^2$ $m^{-2}$ |
| RH | % | relative humidity |
| SE | | standard error |

## LIST OF TABLES

## LIST OF FIGURES

## ACKNOWLEDGMENTS

I wish to acknowledge my advisor, Dr. Andy Black, who's dedication and enthusiasm throughout this research project was truly motivating and very much appreciated. These past two years have been tremendously enjoyable and stimulating thanks to Andy's friendship and guidance throughout all aspects of my M.Sc. studies.

The Campbell River research project was funded by the Forest Renewal British Columbia (FRBC), the National Sciences and Engineering Research Council (NSERC), and the Atmospheric Environment Service (AES) (Canadian Climate Research Network). Personal funding during the past two years was provided by an NSERC Postgraduate Scholarship.

I would like to thank my committee members, Drs. Tim Oke and Mike Novak for their time and assistance throughout my studies.

This research was a truly collaborative effort. Technical expertise was provided by Zoran Nesic and Rick Ketler. I am very grateful to both for all the time spent introducing me to all aspects of the data collection process. Dave Spittlehouse (Research Branch, BC Ministry of Forests) generously gave access to his throughfall and stemflow data. Nigel Livingston and Gilbert Ethier (University of Victoria) provided TDR data. In addition, thanks must be extended to all the Annex 3 crew: Altaf Arain, Jess Britt, Bill Chen, Gord Drewitt, Eva Jork, Scott Krayenhoff, Mike LaGrange, Alberto Orchansky, Rob Swanson, Aisheng Wu, and Paul Yang for making these two years so enjoyable. I wish to thank Paul for all his invaluable help with programming and theory when I first arrived. I am especially grateful to Gord, Eva and Gilbert for their wonderful friendships and generous assistance with all the instrumentation, tower work and programming.

I would like to thank my parents, Glenn and Suzanne Humphreys who have encouraged me to explore since I was young. Also to my entire family and friends who were always interested in my progress and tales from the tower. I would like to gratefully acknowledge Dr. Robert Fleming, (Canadian Forest Service, Sault Ste. Marie) who introduced me to the joys of field work, biometeorology and soil science over four summers of field work in Northern Ontario and sent me on my way to BC. Finally, I wish to extend my love and thanks to my husband, Michael Treberg for his support and caring throughout the successes and setbacks of our academic pursuits. His willingness to take care of so much during my thesis-writing phase, including the time spent in the field, editing my work and preparing the map of our site was truly appreciated.

# 1. INTRODUCTION

In order to predict the consequences of climate change on forest functioning and productivity, an understanding of the processes involved in the evaporation of water from forest canopies over the long-term is required. The extensive stands of highly productive and economically important Douglas-fir on the eastern coast of Vancouver Island are the focus of this study. Due to the characteristically wet, mild winters and dry, warm summers experienced by this ecosystem, this study provides a unique opportunity to investigate how the factors limiting evaporation may vary on annual, seasonal, and diurnal time scales.

Water loss from forest ecosystems depends on physical and physiological processes. These processes governing water loss depend in part upon the presence of intercepted water on leaf surfaces (McNaughton and Jarvis, 1983; Stewart, 1988). Under dry canopy conditions, transpiration, or evaporation of water from the leaf interior, is a function of saturation deficit and radiation and the physiological control exerted by stomata. Stomatal control of water loss can be expressed in terms of an aggregate leaf conductance known as a "big leaf" canopy conductance which responds to the environmental factors of light, ambient $CO_2$ concentration, temperature, leaf and soil water status, humidity, atmospheric pollutants, time of day, and physiological conditions in the plant (Collatz et al., 1991; Jones, 1992). In particular, the canopy conductance ($g_c$) of Douglas-fir stands has been found to depend strongly on soil water potential ($\Psi_{soil}$) and saturation deficit of the air ($D$) (Tan and Black, 1976). Recent experimental evidence supporting a direct, mechanistic stomatal response to transpiration rates rather than $D$ (Mott and Parkhurst, 1991) has been suggested to be applicable to canopy-scale conductance responses (Monteith, 1995a). However, only a few field studies have shown the required decrease in $g_c$ with increasing latent heat flux ($\lambda E$) to occur on a regular basis in order to verify Monteith's (1995b) formulation of canopy conductance (Lhomme, 1998; Pataki et al., 1998). In order to illustrate the important controls on dry canopy evaporation from this Douglas-fir stand, the functional relationships between $g_c$, evaporation rates and these environmental variables are developed (Jarvis, 1976; Stewart, 1988).

When the canopy is wet, water evaporates directly from the leaf surfaces as a function of atmospheric demand ($D$), available energy, and turbulent transport. Under completely saturated conditions, $g_c$ approaches infinity and no longer limits evaporation rates such that the

equilibrium evaporation ($\lambda E_{eq}$), evaporation proportional to the available energy, may be approached. In order for $\lambda E$ to exceed $\lambda E_{eq}$, a non-zero $D$ must be maintained above the evaporating surface (McNaughton and Jarvis, 1983). Over rough forests, efficient turbulent transport of heat and water vapour with adequate wind speeds allows for significant, sustained evaporation rates as water vapour gradients are maintained and very stable atmospheric conditions are avoided (McNaughton and Jarvis, 1983). Possible mechanisms whereby air above extensive evaporating surfaces avoids reaching saturation include advection of dry air from local or large-scale sources (McNaughton and Spriggs, 1989; Singh and Szeicz, 1979; Stewart, 1977) or by the addition of heat directly from the air and/or forest biomass (McNaughton and Jarvis, 1983; Moore, 1976). These mechanisms would be characterized by a downward flux of sensible heat (Rutter, 1967). Significant nighttime $\lambda E$ provides further evidence that a wet canopy may act as a sink for energy supplied by other means than through incoming radiant energy (Pearce and Rowe, 1980; Thom and Oliver, 1977).

Few studies have investigated year-round controls on evaporation and the possibility for rapid transitions between the controls discussed above with the wetting and drying of canopies in winter and summer. Fewer still have attempted to measure $\lambda E$ directly during wet conditions. Forest canopy evaporation has been investigated using a variety of interception methods (Pearce and Rowe, 1980; Rutter et al., 1971), gamma ray attenuation (Calder and Wright, 1986), lysimeter (Calder, 1976), tree weight (Teklehaimanot and Jarvis, 1991), and micrometeorological techniques such as the energy balance/Bowen ratio technique (Stewart, 1977) and energy balance/eddy covariance technique (Gash et al., 1999; Mizutani et al., 1997). None, however report long-term measurements of $\lambda E$ during rainfall using a direct eddy covariance method.

Since the fall of 1997, continuous measurements of surface energy fluxes using the eddy covariance method have been carried out over a 50-year-old, 33-m tall coastal Douglas-fir (*Pseudotsuga menziesii* (Mirbel) Franco) stand, part of the seasonal temperate rainforest located on Vancouver Island, B.C, on the Canadian west coast. With long term measurements of surface fluxes, issues arise related to the reliability of the instrumentation under extremely challenging weather conditions. In this particular climate, specific concerns include the ability of the sonic anemometer to measure velocity components and the acoustic temperature in heavy and constant rainfall conditions. The effects of high humidity on signal attenuation as a result of water vapour adsorption/desorption on the walls of the sampling tube when using a closed-path infrared gas

analyzer are also of concern. The former issue has recently been addressed for rainfall (Gash et al., 1999; Mizutani et al., 1997) and fog/dew conditions (Laubach and Teichmann, 1996). The latter issue has been discussed for water vapour signal attenuation in unsaturated atmospheric conditions (Laubach and Teichmann, 1996). Whether $\lambda E$ may be measured accurately using a closed-path analyzer during conditions of high relative humidity has yet to be addressed.

This study reports on the measurements of water and energy exchange between the atmosphere and this Douglas-fir stand, made year-round between October 15, 1997 and May 31, 1999. In order to provide insight into the nature of evaporation from this ecosystem, encompassing both evaporation of intercepted water and transpiration, the following objectives were addressed:

1. Investigate the reliability and nature of turbulent fluxes of latent and sensible heat measured using the eddy covariance method during non-ideal conditions.
2. Quantify the seasonal and diurnal variations in convective energy fluxes over a west-coast forest.
3. Establish relationships between fluxes of latent heat and environmental variables in order to investigate the physical factors and physiological processes limiting evaporation on a diurnal and seasonal basis.

# 2. THEORETICAL CONSIDERATIONS

The controls on evaporation from a forest canopy may be investigated using a variety of analysis techniques and descriptive parameters. On a seasonal basis, general trends may be observed using the Bowen ratio, the evaporative fraction $\lambda E/R_a$, (where $R_a$ is the available energy flux), the Priestley-Taylor $\alpha$ value, and the McNaughton and Jarvis atmospheric decoupling coefficient, $\Omega$.

Water loss from the canopy through the process of evaporation may be expressed as the latent heat flux component of the forest surface energy budget,

$$R_n = H + \lambda E + G + J \qquad (2.1)$$

where net radiation ($R_n$) is balanced by the sum of the convective fluxes of sensible ($H$) and latent heat ($\lambda E$), soil heat flux ($G$), and the rate of energy storage ($J$). Not included in the analysis in this thesis are the energy budget terms for the rate of energy consumption during photosynthesis and for the advection of sensible and latent heat. The rate of energy consumption rarely exceeds 1% to 4% of $R_n$ in most forests (Blanken, 1997; Stewart and Thom, 1973). Advection effects are assumed to be negligible, as this forest is extensive and homogeneous, and will be discussed further in Section 4.2.

The Bowen ratio is used to describe the partitioning of $R_a$, the net radiative energy not distributed into energy storage or soil heat flux ($R_a = R_n - G - J$) into sensible and latent heat fluxes and is defined as,

$$\beta = \frac{H}{\lambda E} \qquad (2.2)$$

where $\beta$ is the Bowen ratio.

The evaporative fraction, $\lambda E/R_a$ simply describes the proportion of available energy used in the change of state of liquid water into water vapour for either intercepted rainfall on the surfaces of the forest canopy or for water from within the stomatal cavities.

The Priestley-Taylor $\alpha$ represents the ratio of measured $\lambda E$ to the equilibrium latent heat flux ($\lambda E_{eq}$) which is the evaporation rate expected for extensive, well-watered surfaces (Priestley and Taylor, 1972) shown as,

$$\alpha = \lambda E / \lambda E_{eq} = \lambda E / \left[ \frac{s}{(s+\gamma)} R_a \right] \tag{2.3}$$

where $s$ is the rate of change of saturation vapour density with temperature and $\gamma$ is the psychrometric constant. This relationship is useful for demonstrating the degree of dependence evaporation rates have on available energy (Thompson et al., 1999). Values for $\alpha$ have been found to be about 1.26 for a wide variety of surface types not experiencing water stress (McNaughton and Spriggs, 1989). The 26% increase from $\lambda E_{eq}$ has been suggested to result from entrainment of dry, warm air from the inversion at the top of the planetary boundary layer increasing the total demand for evaporation slightly above that supported by the available energy (de Bruin, 1989).

The McNaughton and Jarvis atmospheric decoupling coefficient has also been used to quantify the relative importance of $R_a$ and $D$, the driving variables for evaporation. This coefficient is defined as,

$$\Omega = \left[ 1 + \frac{\gamma}{s+\gamma} \frac{g_a}{g_c} \right]^{-1} \tag{2.4}$$

where $g_a$ is the aerodynamic conductance and $g_c$ is the canopy conductance discussed further in Section 2.1.3. Small values of $\Omega$ indicate that the surface $D$ is a function of regional conditions due to efficient mixing of air between the evaporating surface and the atmosphere representative of conditions extending into the boundary layer (McNaughton and Jarvis, 1983). Alternatively, large values of $\Omega$ indicate that the surface is isolated from overlying atmospheric conditions due to a smaller aerodynamic conductance. As a result, surface $D$, in the latter case, is controlled principally by incoming radiation independently of changes to surface conductance or regional atmospheric conditions (McNaughton and Jarvis, 1983).

The nature of the canopy surface conductance to water vapour is critical to seasonal variations in evaporation rates. When the canopy is dry, the importance of the physiological control of transpiration is increased, while evaporation of intercepted rainfall from a wet canopy is ultimately linked only to the atmospheric demand, energy inputs, and turbulence required to transport heat and water vapour to and from the source of water (Oke, 1987). These physical and physiological controls on evaporation from a forest canopy are discussed below.

### 2.1.1 Evaporation and the Penman-Monteith Combination Equation

The Penman-Monteith combination equation describes evaporation from a vegetated surface as a function of the meteorological driving variables and the surface properties of the vegetation in the following manner (Monteith, 1965),

$$\lambda E = \frac{sR_a + \rho c_p D g_a}{s + \gamma(1 + g_a / g_c)} \tag{2.5}$$

where $R_a$ is the available energy flux density, $s$ is the change in saturation vapour density with temperature, $\gamma$ is the psychometric constant, $\rho$ and $c_p$ are the density and specific heat of air, $D$ is the saturation deficit of the air, $g_a$ is the aerodynamic conductance, and $g_c$ is the surface or canopy conductance to water vapour. Equation (2.5) assumes that the canopy behaves as one "big leaf", that this "big leaf" is isothermal, that saturation vapour pressure is a linear function of air temperature, enabling surface temperature to be eliminated from the equation (i.e. Penman transformation), and that the boundary layer conductances to water vapour and heat transfer are equal (Monteith and Unsworth, 1990). Thus, for turbulent conditions in forests when $g_a \gg g_c$, $\Omega$ values are small and transpiration is closely linked to $D$ and $g_c$ (i.e. $\lambda E$ approaches $\rho c_p D g_c / \gamma$)(McNaughton and Jarvis, 1983).

### 2.1.2 Wet Canopy Conditions

Under saturated canopy conditions, $g_c$ is expected to approach infinity so that Equation (2.5) may be expressed as,

$$\lambda E = \frac{s}{s+\gamma} R_a + \frac{\rho c_p D g_a}{s+\gamma} \tag{2.6}.$$

Evaporation rates from wet forest canopies may exceed equilibrium evaporation rates ($\lambda E_{eq}$) as defined in Equation (2.3) and shown as the first term of Equation (2.6), when the second term is significant. Equation (2.6) has been referred to as the potential or free evaporation rate (McNaughton and Black, 1973). With a significant $D$ and adequate wind speeds over aerodynamically rough forests ($g_a$ can become large), situations arise where $\lambda E$ from a wet canopy may be large enough to produce $\alpha$ values in excess of 11 (Shuttleworth and Calder, 1979), $\lambda E/R_a$ ratios up to 4 and $\beta$ values in the range of -0.5 to 0.5 (McNaughton and Jarvis,

1983). Similarly, $\lambda E$ from a wet canopy may be considerable during the night, despite a lack of downwelling net radiative energy, when the second term of Equation (2.6) is significant and the required energy input is supplied by downward $H$.

### 2.1.3 Dry Canopy Conditions and Canopy Conductance

Equation (2.5) describes the "big leaf" model of canopy evaporation. In this form, the aggregate responses of all the stomata within a canopy experiencing different light, humidity and temperature regimes are described in terms of a single canopy stomatal conductance ($g_c$). Using measurements of transpiration from a dry canopy, $g_c$ can be computed using a rearrangement of Equation (2.5),

$$\frac{1}{g_c} = \left[\frac{s}{\gamma}\left(\frac{R_a}{\lambda E} - 1\right) - 1\right]\left(\frac{1}{g_a}\right) + \frac{\rho c_p D}{\gamma \lambda E} \qquad (2.7)$$

Canopy conductance has been shown to respond similarly to the same factors which influence the conductance of a single leaf or coniferous shoot (Tan and Black, 1976). Control of stomatal conductance ($g_s$) is effected by the adjustment of stomatal aperture in a complex response to environmental conditions (Leuning, 1995). Jarvis-type phenomenological models describe $g_s$ as a function of limiting abiotic factors presumed to act independently on $g_s$ in a multiplicative manner (Jarvis, 1976; Stewart, 1988). The common form for this model is,

$$g_s = g_{\max} f_1(Q) f_2(T_s) f_3(D_s) f_4(c_s) f_5(\Psi_{leaf}) \qquad (2.8)$$

where $f_1$, $f_2$, ... are linear or non-linear functions of the various environmental variables; $Q$ is photosynthetic photon flux density, $T_s$ is leaf surface temperature, $D_s$ is the saturation deficit at the leaf surface, $c_s$ is carbon dioxide concentration at the leaf surface, and $\Psi_{leaf}$ is leaf water potential (Jarvis, 1976). Another series of more readily available environmental variables often substituted for those listed above include global solar radiation ($S\downarrow$), saturation deficit ($D$) and temperature ($T$) of the air, and soil water potential ($\Psi_{soil}$) (Stewart, 1988). Of these variables, both $g_s$ and $g_c$ in Douglas-fir stands have been found to be closely related to $D$ and $\Psi_{soil}$ (Tan and Black, 1976).

Another type of model used to predict $g_s$ are the semi-empirical, coupled photosynthesis-stomatal constraint models (Ball et al., 1987; Leuning, 1995). These are based on the idea that stomatal control has evolved to optimize carbon gain through photosynthesis while minimizing

water loss through transpiration (Collatz et al., 1991). Support for these models has come from the strong correlation observed between carbon assimilation rates and $g_s$ (Wong et al., 1979).

Both types of models incorporate environmental factors such as $T$, $Q$ and $c_s$ which have a direct, physiological effect on the plant's ability to sequester carbon through photosynthesis. Soil or leaf water potential may also be interpreted as the direct control of stomatal aperture through guard cell water status. Both types of models also depend heavily on humidity response functions. However, $D$ has never been shown to have a direct effect on stomatal functioning despite the many examples of the high degree of correlation between the two (Monteith, 1995b).

Mott and Parkhurst's (1991) pivotal gas-exchange measurements using air and helox provided experimental evidence that a mechanism for control of $g_s$ is based on stomatal responses to the water-loss rate of the leaf rather than one based on $D$ of the air. One interpretation is that changes in the demand ($D$) and supply of water ($\Psi_{soil}$) may be 'sensed' as well as mediated by the guard cells and surrounding epidermal cells as water evaporates from them (Grantz, 1990).

Based on these findings, Monteith (1995b) reinterpreted 52 sets of laboratory-based measurements on 16 species to illustrate how $g_s$ can be interpreted as a linearly decreasing function of evaporation or transpiration rates ($E$) under non-limiting soil water and light conditions as,

$$\frac{g_s}{g_m} = 1 - \frac{E}{E_m} \tag{2.9}$$

where $g_m$ is an empirical coefficient representing the maximum conductance obtained by extrapolation to zero $E$ and $E_m$ is an empirical coefficient representing the maximum transpiration rate obtained by extrapolation to zero $g_s$. Experimental evidence for a linearly decreasing relationship between $g_s$ and $E$ was suggested to support the existence of a direct mechanistic link between $g_s$ and $E$ (Monteith, 1995b). Essentially, this reinterprets the negative feedback model for stomatal response to $D$. This response is based on a mechanism whereby an increase in $D$ results in an increase in $E$ and a corresponding decrease in leaf water potential. As a result, decreasing guard cell turgor decreases stomatal aperture leading to a reduction in $E$. With each feedback loop, $E$ is not reduced proportionally to the increase in the driving force for evaporation such that an overall gain leads to a saturation-type curve. Experiments show that as $D$ increases, stomatal regulation of water loss from the leaf maintains leaf water potential just above the value predicted to cause incipient turgor loss (Saliendra et al., 1995). In fact, a

decreasing hyperbolic relationship between $g_c$ and $D$ such as $g_c = \frac{a}{1+cD}$ is consistent with both a negative feedback response to $D$ and Monteith's (1995b) formulation of $g_c$. However, only a few studies have attempted to scale Equation (2.9) experimentally or theoretically to canopy-level processes (Lhomme, 1998; Meinzer et al., 1997; Pataki et al., 1998).

Investigations into the nature of the functional relationships between $g_c$ and the environmental variables $Q$, $\Psi_{soil}$ and $D$ as well as the evaporation rate itself will be used to illustrate the significant, underlying mechanistic processes which control $g_c$ and thus dry canopy evaporation rates from this particular forest canopy.

# 3. METHODS

## 3.1 SITE DESCRIPTION

This study, which is part of an ongoing, long-term carbon dioxide and water vapour exchange monitoring project within the Ameriflux Network, was carried out on the eastern coast of Vancouver Island near Campbell River, BC, Canada (49°51'N, 125°19'W) between October 15, 1997 and May 31, 1999 (Fig. 3.1). The site was located approximately 9 km from Georgia Straight on a 5 to 10° terrain slope at an elevation of 300 m and was covered by a dense (1054 trees $ha^{-1}$), even-aged, naturally regenerated, second-growth stand of 50-year-old Douglas-fir. The forest also contained 17% Western Redcedar (*Thuja plicata* Donn ex D. Don) and 3% Western Hemlock (*Tsuga heterophylla* (Raf.) Sarg.) with a sparse understory consisting of moss species, ferns, and herbaceous species such as Salal (*Gaultheria shallon* Pursh), Dull Oregon-grape (*Berberis nervosa* Pursh), and Vanilla-leaf deer foot (*Achlys triphylla* (Smith) DC). This forest was part of the coastal temperate rainforest, specifically the drier seasonal rainforest particular to the low and middle elevations of eastern and central Vancouver Island extending south through Oregon (Pojar and MacKinnon, 1994).

The canopy height was 33 m with a canopy base beginning at 15 m. Mean tree bole diameter at breast height was 23.2 ± 0.9 cm (± 1 SE) determined through a census of all trees within a 0.12 ha square. Canopy cover was estimated to be 70% (from 1 - $p$, Section 3.3.3) with a one-sided leaf area index (LAI) of 4.0 $m^2$ $m^{-2}$ measured using a LICOR 2000 canopy analyzer (LI-COR, Lincoln, Nebraska, USA). The LAI was likely underestimated since the measurement was not corrected for slope angle or leaf clumping as Douglas-fir canopies tend to be very clumped with a strongly planophile leaf inclination (Black et al., 1991).

The soil was a deep humo-ferric podzolic soil with a loamy sand texture in the upper 40 cm developing to sand with increasing depth (Appendix B). On average, the mean coarse fragment content (particle size diameter > 2 mm) was 31.4 ± 2.4% (± 1 SE) by volume throughout the profile to a depth of 80 cm. This was determined using 1 to 1.5 kg samples at four depths extending from the surface to 80 cm. A shallow LFH organic layer of mor type, between 1 to

10 cm in depth, overlay a mineral soil with a mean total bulk density of 1352 ± 51 kg $m^{-3}$ (± 1 SE) and a mean porosity of 49.0 ± 1.1% (± 1 SE) determined from soil 10 cm below the surface to a depth of 80 cm. Density increased slightly with depth while the mineral soil between the LFH layer and 10 cm was quite variable with a mean density of 971 ± 221 kg $m^{-3}$ (± 1 SE). Bulk density was determined using two to three soil core samples with a volume of $3.54 \times 10^{-4}$ $m^3$ or $6.62 \times 10^{-5}$ $m^3$ at 10-cm depth intervals throughout the soil profile.

The eddy covariance system and supporting micrometeorological equipment were installed on a 45-m tall open-lattice triangular communication tower 0.5 m in width, erected on site. A minimum fetch of 400 m was determined by the limits of the 50-year-old stand to the SW (Fig. 3.1). There was about 700 to 800 m of fetch to the NE, in the direction of the prevailing daytime winds. The stand was surrounded on all sides by Douglas-fir stands ranging in age from 24 to 57 years. Approximately 1.5 km WSW of the tower towards Mount Washington and Forbidden Plateau in the center of the island, a plateau was followed by a descent into a marsh area. The remaining area was very homogeneous (Fig. 3.1)

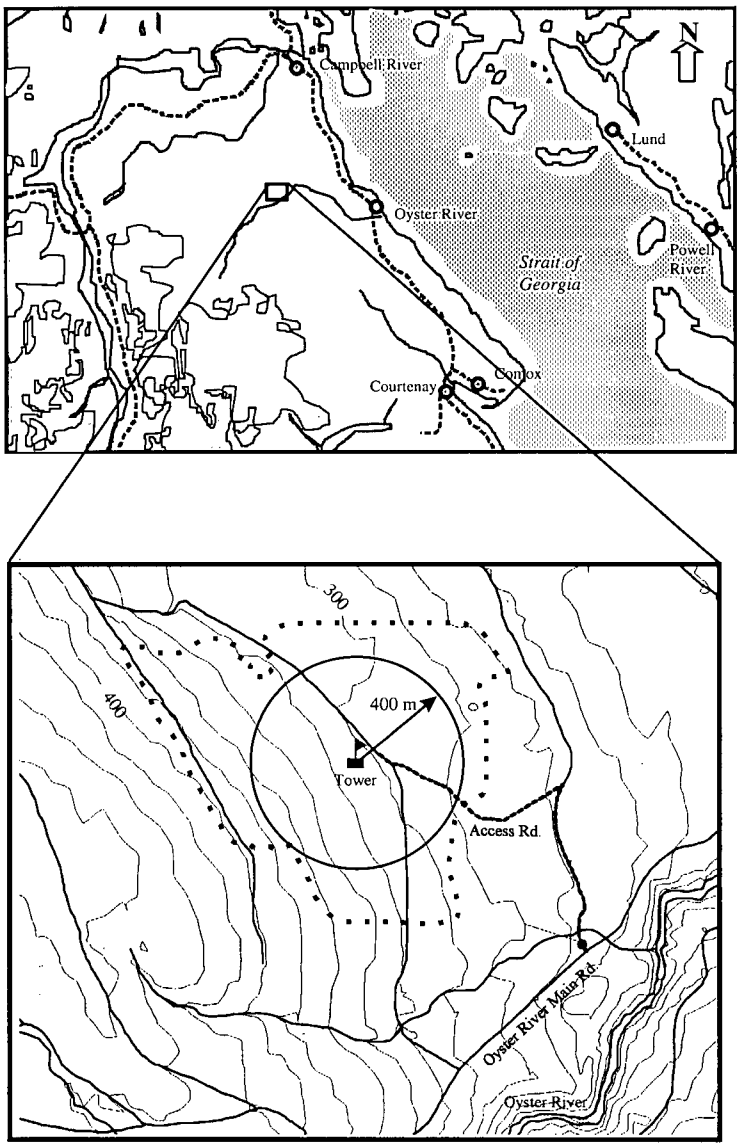


Fig. 3.1 Location of the experimental site (shown as a square) on Vancouver Island between Campbell River and Oyster River, B.C illustrating the site's proximity to the mountains (shaded areas) to the west and to Georgia Straight towards the east. The lower diagram indicates the tower location with respect to the Douglas-fir forest planted in 1949 (dashed line) and elevation in meters. Surrounding stands are Douglas-fir with ages varying from 38 - 40 years to the west, 24 - 54 years to the south, 47-57 years to the east and north.

## 3.2 TURBULENT FLUX MEASUREMENTS

Total flux densities of latent heat ($\lambda E$), sensible heat ($H$) and momentum ($\tau$) were measured by an eddy covariance system located 9.7 m above the canopy at 42.7 m on the 45-m tall triangular tower. These eddy fluxes were calculated using 30 min covariances of high-frequency measurements of vertical wind speed ($w$) and the appropriate scalar or wind speed in the following manner,

$$\lambda E = \lambda \rho \overline{w' \chi_w'} \tag{3.1}$$

$$H = \rho c_p \overline{w' T_a'} \tag{3.2}$$

$$\tau = -\rho \overline{u' w'} \tag{3.3}$$

where primes denote deviations from the linearly detrended mean, overbars indicate a time average, $\lambda$ is the latent heat of vaporization, $\chi_w$ is the mixing ratio for water vapour (mmol mol$^{-1}$ dry air) derived as $\chi_w = \chi_{ww} / (1 - \chi_{ww} / 1000)$, where $\chi_{ww}$ is the mole fraction of water vapour (mmol mol$^{-1}$ moist air), $\rho$ is the dry air density, $c_p$ is the specific heat of air, $T$ is the air temperature and $u$ is the streamwise wind velocity. A three-dimensional sonic anemometer-thermometer with a vertically asymmetric sensor array and 15-cm path length (model Solent 1012R2A, Gill Instruments, Lymington, UK) was used to measure $u$, $v$, $w$, and $T$. Air temperature was concurrently measured using fine wire thermocouples (25 µm chromel-constantan thermocouple wire, OMEGA Engineering Inc., Laval, Quebec). A closed-path infrared gas analyzer (IRGA) (model 6262, LI-COR Inc., Lincoln, Nebraska, USA) measured $\chi_w$. All high frequency measurements were recorded at 125 Hz and subsampled to 20.83 Hz in order to prevent signal aliasing and to reject 60 Hz AC power line noise (Yang, 1998).

Latent heat flux was also periodically measured as $\lambda \overline{w' \rho_v'}$ with water vapour density fluctuations ($\rho_v'$) determined using a krypton hygrometer (model KH20, Campbell Scientific Inc., Edmonton, Alberta). Oxygen corrections (Tanner et al., 1993) and corrections to account for the effects of temperature and humidity on air density were applied to $\lambda \overline{w' \rho_v'}$ (Webb et al., 1980).

To minimize errors due to sensor separation, the inlet to the IRGA sampling tube was located within 50 cm of the sonic anemometer (Kristensen et al., 1997; Lee and Black, 1993). Air was drawn at 8 to 10 L min$^{-1}$ through the sampling tube, which was 4-m long, heated (15 W), and

connected to the IRGA via a 1 μm PTFE filter (GelmanSciences, Ann Arbor, Michigan, USA). This ensured that turbulent flow was achieved within the polyethylene coated tubing with an inner diameter of 4 mm (Dekabon Type 1300, Dekoron, Furon Brands, Aurora, Ohio, USA) and that condensation would not occur. Turbulent flow also limited the effects of velocity profiles within the tube which cause signal attenuation of high-frequency fluctuations of $\chi_w$ and carbon dioxide mole fraction ($\chi_c$) (Massman, 1991). The IRGA was housed within a thermostatted box in which temperatures were held at a constant 27 to 31°C with temperature variations of less than 0.3 °C within each half hour. Sample cell pressure and optical bench temperature were used in corrections applied to the IRGA signals prior to the application of the calibration polynomial (LI-COR, 1996)(see Appendix A).

Delay times were calculated online as the delay in $T$ required to maximize the cross correlation of $\chi_w$ and $T$ using the first 3 to 4 minutes of samples within each half hour. The $w$ signal from the sonic anemometer was digitally lagged using this delay time to ensure the $w$ signal remained in phase with the $\chi_w$ signal which was delayed due to the time required for the air stream drawn in through the sampling tube to reach the IRGA. The delay times used throughout the measurement period were 1.10 s (equivalent to 23 samples) for October 15, 1997 to November 10, 1998 and 0.96 s (equivalent to 20 samples) for November 10, 1998 to June 9, 1999. These were determined in good weather under normal operating conditions. Delay time changes were due to differences in sampling flow rates and resistance within the IRGA system following pump and tubing changes. These delay times were applied consistently to each half hour in order to account for the delay caused solely by the transit time. This was necessary as $\chi_w$ fluctuations were damped by reactions at the tube walls under certain weather and setup conditions (see Section 4.1), while $\chi_c$ measured with the same IRGA was affected to a much lesser degree (Laubach and Teichmann, 1996).

Co-ordinate rotation was also applied to the sonic anemometer wind vectors in order to bring the x, y plane parallel to the average upwind slope (Tanner and Thurtell, 1969) and minimize apparent mass flow errors associated with a non-zero mean vertical velocity (Moncrieff et al., 1996). This procedure involved mathematically rotating the three wind vectors to obtain $\bar{v} = \bar{w} = 0$ and $\overline{u'v'} = 0$ where the resulting vertical velocity vector ($w$) is normal to the mean wind streamline (Tanner and Thurtell, 1969).

### 3.2.1 IRGA Calibration Procedures

The IRGA was calibrated every 24 h at midnight using nitrogen gas to zero both $\chi_w$ and $\chi_c$ measurements, while $\chi_c$ was spanned using 350 μmol $CO_2$ per mol dry air. The offset and gain calculated for $\chi_c$ were then applied to the mV readings of both $\chi_c$ and $\chi_{ww}$ prior to applying the calibration polynomial for the calculation of $\chi_{ww}$ and $\chi_c$ mol fractions (see Appendix A). During May 1999, the ability for the span of $\chi_c$ to properly calibrate $\chi_w$ readings was tested using a dew point hygrometer (Model HYGRO M4, General Eastern Instruments, Woburn, Massachusetts, USA). Half an hour before midnight, an average of the ambient humidity above the canopy (within 5 m of the IRGA intake tube) was used to calculate the $\chi_w$ gain and compared with subsequent $\chi_c$ calibration gains. Gains for $\chi_w$ were found to vary from those of $\chi_c$ by less than 1.41% with a mean increase of 0.39 ± 0.41% (± s.d.) between May 15 and June 6, 1999. As a result, $\lambda E$ would generally be underestimated by approximately 0.39% by assuming the same calibration gains for $\chi_w$ and $\chi_c$ measurements.

## 3.3 SUPPORTING MEASUREMENTS

### 3.3.1 Weather and Soil Variables

Net radiation flux density ($R_n$) was measured using two net radiometers at 41.3 m (type S-1, Swissteco, Switzerland) one of which was heated in order to prevent nighttime errors due to dewfall on the sensor domes (McGinn et al., 1989). Downward short-wave radiation (S↓) was measured using a solarimeter (type CM5, Kipp & Zonen, Delft, Holland). Downward and reflected photosynthetic photon flux density ($Q$) were measured using two quantum sensors (Model LI-190SB, LI-COR, Lincoln, Nebraska, USA) all located at the top of the tower at 45.2 m. In addition, a solarimeter (type CM5, Kipp & Zonen, Delft, Holland) was placed on the ground throughout the summer and fall of 1998.

Two tipping bucket rain gauges with a 5 tip/mm (Texas Electronics Inc., Dallas, Texas, USA) and 1.25 tip/mm sensitivity (Sierra Weather Instrument Corp., Nevada City, California, USA) measured rates of gross rainfall. These were installed on the tower at the 24-m height, just below the canopy top in order to minimize wind losses. Agreement with a storage rain gauge

located in a gap in the canopy ~500 m from the tower was generally good. Snow depth was monitored using air temperature measurements at 1, 5, 10, 20, and 50 cm above the ground using chromel-constantan thermocouples made by twisting and soldering 36 gauge thermocouple wire (OMEGA Engineering Inc., Laval, Quebec). Diurnal temperature amplitudes were strongly damped and temperatures tended towards zero when snow covered the thermocouples.

Soil heat flux density ($G$) was measured using three spatially separated soil heat flux plates (Model Middleton CN3, Carter-Scott Design, Victoria, Australia) buried at a depth of 2 cm, at the interface between the LFH and mineral soil layers. Soil heat flux at the surface ($G$) was computed by adding the rate of heat storage within the top 2 cm of soil to the measured flux ($G_{2cm}$) as,

$$G = G_{2\mathrm{cm}} + C_s \frac{\Delta T_s}{\Delta t} \tag{3.4}$$

where $C_s$ is the total soil volumetric heat capacity ($C_s = C_o\theta_o + C_w\theta_w$). The heat capacity for soil organic matter, $C_o$ is equal to 2.5 MJ $m^{-3}$ $°C^{-1}$, the volumetric fraction of soil organic matter is $\theta_o = \rho_b / \rho_o$ = 500 kg $m^{-3}$ / 1300 kg $m^{-3}$ = 0.38, where $\rho_b$ and $\rho_o$ bulk and organic particle size densities, respectively. The heat capacity for water, $C_w$ is 4.18 MJ $m^{-3}$ $°C^{-1}$ and $\theta_v$ is the volumetric water content measured by the Water Content Reflectometer located in the top 2 to 3 cm of soil (see below). $\Delta T_s / \Delta t$ is the change in temperature in the top 2 cm of soil measured using three soil thermocouples buried at 0.5, 1 and 2 cm depths. Accounting for storage increased half hourly values of $G$ by 17 to 20% on average.

Volumetric water content was measured every half hour using four Water Content Reflectometers (Model CS615, Campbell Scientific, Inc., Edmonton, Alberta) installed diagonally at one location to sample the soil layers at four depth intervals: 2-3 cm, 10-12 cm, 35-48 cm, and 70-100 cm. These measurements were integrated over a 100-cm depth by multiplying the values by 5, 20, 35, and 40 cm, respectively to obtain a total soil volumetric water content. These measurements were accompanied by eleven stations, each with a pair of TDR parallel probes (2 mm diameter stainless steel rods) 30 cm and 76.2 cm long buried vertically and measured three to four times per month between April and November each year. Gravimetric samples were also taken during the summer on a bi-monthly basis throughout the soil profile to a depth of 100 cm. A linear relationship was determined between the TDR and CS615 measurements and applied to the CS615 measurements integrated over 100 cm to obtain

an averaged site soil volumetric water content for analysis purposes. The CS615 values were increased by a factor of 1.88 and offset by -0.036 $m^3 m^{-3}$.

Soil water potential, specifically soil matric potential, was measured manually during the summer months using a tensimeter (Soil Measurement Systems, Tuscon, Arizona, USA) and tensiometers at eight stations. Each station consisted of four tensiometers at 10, 25, 45, and 70 cm depths. Predawn water potentials of ten to twelve shoots between 24 and 28.5 m above the ground were measured using a pressure chamber (Plant Water Status Console, Soil Moisture Equipment Corp., Goleta, California, USA) between 04:30 h and 06:00 h August 13 and 20, 1998 in order to evaluate an integrated soil water potential experienced by the trees. Laboratory soil water release measurements were also fitted with van Genuchten's (1980) relationship between volumetric water content and matric potential (see Appendix B). These non-linear relationships were determined using an optimization procedure known as the Nelder-Mead simplex (direct search) method (The MathWorks, 1996). The curves indicated that this soil had an average available water content of 0.14 $m^3 m^{-3}$ in the sandy 70 to 100 cm layer (-0.01 to -1.5 MPa associated with water contents of 0.19 and 0.05 $m^3 m^{-3}$, respectively). In the upper loamy sand soil layer from 6 cm to 50 cm, the average available water content was 0.16 $m^3 m^{-3}$ (-0.01 to -1.5 MPa associated with water contents of 0.25 and 0.09 $m^3 m^{-3}$, respectively). These two functions were then applied to only the CS615 measurements according to soil depth and weighted for the four depths (using 6, 20, 35, and 40% for the four probes in descending order) to give an estimate of soil water potential for analysis over the measurement period. The resultant soil water potential was verified to be representative at high and low water contents by comparisons with the tensiometer and predawn measurements, respectively.

Soil temperature was measured using burial-type copper-constantan thermocouples (Model 105T, Campbell Scientific Inc., Edmonton, Alberta) at 2, 5, 10, 20, 50, and 100 cm depths at one location, a mini profile of 0.5, 1, and 2 cm depths at a second location and a single third replicate of the 2 cm depth at a third location.

A profile of eight 76 μm wire chromel-constantan thermocouples were installed at 2, 5, 9, 15, 21, 27, and 44 m above the ground. A thermistor and Vaisala capacity relative humidity sensor (Model HMP35CF, Campbell Scientific Inc., Edmonton, Alberta) were mounted in an aspirated shield (Model 105C, Met-One Instruments, Grant Pass, OR) 4 and 40 m above the ground and used to measure air temperature and relative humidity, respectively. An additional thermistor

was located at 27 m in a non-aspirated shield (model 41004-5 Gill Radiation Shield, Campbell Scientific Inc, Edmonton, Alberta).

Tree bole temperature was measured using chromel-constantan thermocouples made by twisting and soldering 0.254 mm diameter thermocouple wire (OMEGA Engineering Inc., Laval, Quebec). Two trees boles were installed with three thermocouples 2, 50, and 150 mm and 2, 82, and 164 mm below the bark surface on the north side of the bole 3 m above the ground. The second tree had a second set of thermocouples installed 2 and 27.9 mm below the bark surface at a height of 27 m.

Wind direction and wind speed was measured at 40 m and at 3.5 m above the ground using wind monitors (Model 05103, R.M. Young Co., Traverse City Michigan, USA). The Gill sonic anemometer also provided wind speed and direction measurements at 42.7 m.

All automated weather and soil measurements were sampled every 2 to 5 s using dataloggers (Models CR10, CR7 and 21X, Campbell Scientific Inc., Edmonton, Alberta) and averaged over half hour intervals.

### 3.3.2 Evaporation from the Forest Floor

Rates of evaporation of water from the forest floor were determined over nine days in August 1998. Total soil moisture evaporation included water which evaporated from within the surface soil, from free-standing water on the soil surface and understory vegetation, and through transpiration from the ground vegetation. Two cylindrical plastic lysimeters 12 cm deep with a 188.6 $cm^2$ surface area were weighed three to five times daily to determine water lost through evaporation. Soil within the lysimeter was replaced about once every two to three days to avoid losing soil contact with the sides or bottom of the lysimeter as the soil dried.

In total 1.35 mm of water was lost over 402 half hours for lysimeter #1 while 0.66 mm of water was lost over 354 half hours for lysimeter #2. Matching the time intervals for lysimeter measurements with evaporation measured with the eddy covariance system, evaporation of water from the forest floor using the two lysimeters amounted to 7.5% and 4.2% of the total evaporation, respectively, over both daytime and nighttime periods.

### 3.3.3 Canopy Wetness

Canopy wetness was determined using a combination of leaf wetness sensors, water balance calculations using throughfall and stemflow measurements and a 'waterbox' model based on the Rutter et al. (1971) interception model. Electrical grid leaf wetness sensors (Model 237, Campbell Scientific Inc., Edmonton, Alberta) were painted off-white, treated to reduce responses to high humidity (Gillespie and Kidd, 1978) and cut to 2.0 cm × 7.7 cm. These were installed on the tower at three heights with two replicates at the base of the canopy (15 m), mid-canopy (24 m) and canopy height (33 m) with the sensors tipped about their long axis at about 30°. Resistance values corresponding to wet conditions were determined by identifying the maximum possible resistance measures associated with canopy saturating rainfalls and verified visually. To avoid any possibility of high humidity resulting in erroneous canopy wetness measurements, the sum of the rainfall measurements for 6 h prior and 1 h after the time a saturated canopy was identified could not equal zero. Five 6 m long, 0.1 m wide, and 0.1 m deep gutter troughs with 20 mm high vertical sides and a V-shaped bottom to minimize water loss through splashing were used to determine the rates of total throughfall ($P_{th}$). Stemflow ($P_{st}$) was determined using five spiral rubber collars fixed to tree trunks. The water balance calculation method and the 'waterbox' model for determining canopy wetness required estimates of characteristic canopy parameters as defined by Rutter et al. (1971). These were determined using measurements between May 16, 1998 to November 23, 1998 and April 20, 1999 to May 31, 1999 when the throughfall apparatus was known to be in good working order. Following Leyton et al. (1965), the proportion of rainfall for individual storms not intercepted by needle or stem surfaces, known as the free throughfall coefficient ($p$), was found to be 0.28 and the minimum depth of water required to saturate the entire canopy surface, known as storage capacity ($S$) was 1.0 mm (see Appendix C).

When the throughfall and stemflow measurements were available, a running water balance was calculated as,

$$C_i = C_{i-1} + P_i - E_i - P_{th_i} - P_{st_i} \qquad (3.5)$$

where $C$ is the amount of water (mm) stored on the canopy at the end of each time step ($i$). Note that evaporation ($E$) measurements may have been underestimated due to problems with IRGA measurements during conditions with high humidity (Section 3.3.24.1) and strong atmospheric

stability, characteristic of rainy periods (Section 4.3). Therefore, $E$ was crudely estimated as the residual of the energy budget for this particular calculation to minimize excessive $C$ values. During half hour periods when $C \geq S$, the canopy was considered saturated with water, when $0 < C < S$, the canopy was considered partially wet and when $C = 0$, the canopy was considered dry.

For the study period between October 1997 and April 1998, when neither leaf wetness sensors nor throughfall apparatus were in place, Equation (3.5) was modeled as a simple 'waterbox' based on the Rutter interception model (Rutter et al., 1971) where throughfall was expressed as a total of the proportion of gross rainfall which did not hit the canopy and that which drains from the canopy ($P_d$), $\sum P_{th} = p\sum P + \sum P_d$. For each time step, $P_d$ was calculated as (Valente et al., 1997),

$$P_{di} = \begin{cases} C_{i-1} - S, & C_i \geq S \\ 0, & C_i < S \end{cases} \quad (3.6).$$

For each time step, $i$, $C$ was calculated as

$$C_i = \max\left[0,\ C_{i-1} + (1-p)P_i - E_i - P_{di}\right] \quad (3.7)$$

where $E$ was again estimated as the residual of the energy budget. Equation (3.7) ensured that the minimum value of $C_i$ was zero for cases when the combination of the other terms resulted in unrealistic negative values.

There was some concern with using a Rutter model throughout the winter when it had been developed with spring and summer data as $p$ and $S$ may vary with orientation of the foliage (Rutter et al., 1971). During the winter of 1997/98, which experienced only four days of snow on the ground, these changes were likely small, while in 1998/99 the ground was covered with at least 1 cm of snow for approximately eighty days. As a result, the greater number of heavy snowfalls on the canopy would have caused greater changes in these coefficients and parameters.

Good agreement was found between both the measured and modeled water balance method and the leaf wetness sensors as illustrated for six days in October, 1998 (Fig. 3.2).

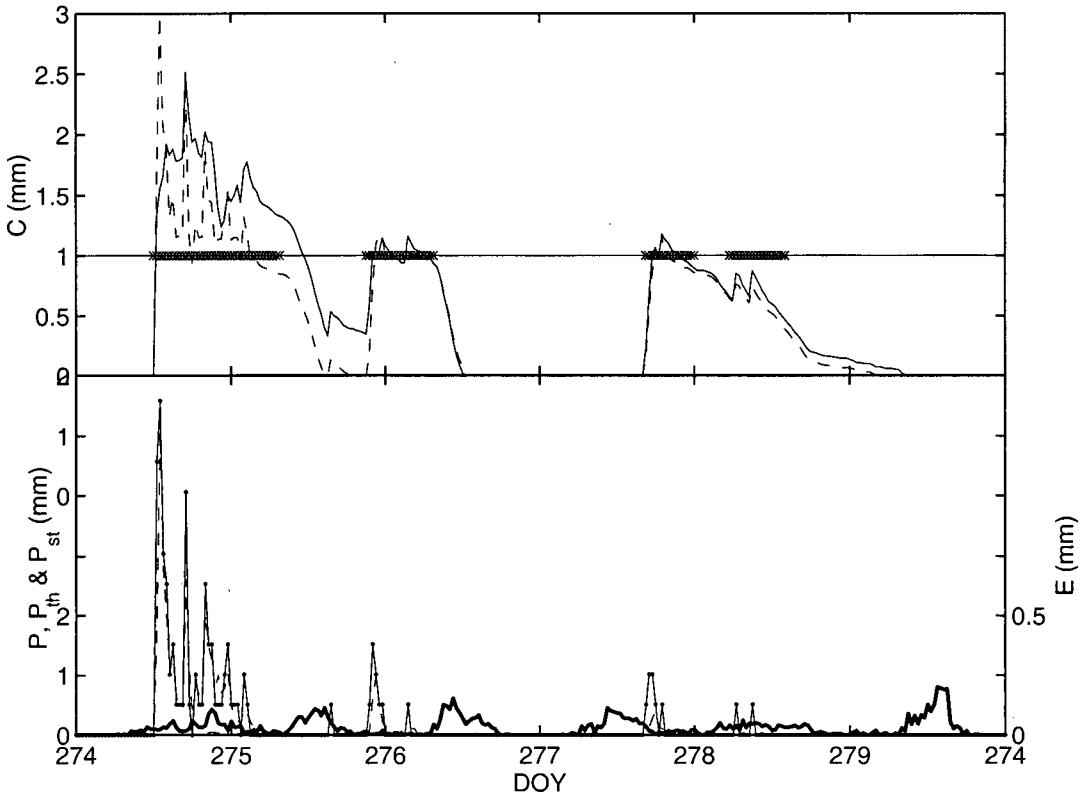


Fig. 3.2 Canopy storage and times of canopy saturation (top panel) for October 1 to 7, 1998 determined using the measured water balance (solid line), modeled water balance (dashed line) and leaf wetness sensors (heavy line) (top panel). The bottom panel shows the measured values of gross rainfall ($P$) (solid line with dots), throughfall ($P_{th}$) and stemflow ($P_{st}$) (dashed line) used in these calculations. $E$ (thick solid line) was calculated as the residual of the energy budget terms.

## 3.4 METHODS OF ANALYSIS

### 3.4.1 Calculation of Zero-Plane Displacement

Zero-plane displacement ($d$) is the height above the ground at which momentum is absorbed (Monteith and Unsworth, 1990). This parameter is expected to be approximately 0.6 to 0.7$h$ and depends heavily on vegetation height and structure and to some extent, wind speed (Monteith and Unsworth, 1990). In order to investigate $d$ for this forest, a manipulation of the log wind profile was performed in order to express $d$ as a function of measurable meteorological variables.

The log wind profile is expressed as,

$$u = \frac{u_*}{k}\left[\ln\left(\frac{z-d}{z_o}\right) + \Psi_m\right] \tag{3.8}$$

where $u$ is the average horizontal wind speed, $k$ is the von Karman constant ($k$ = 0.4), $u_*$ is friction velocity ($u_* = \left[\overline{u'w'}^2 + \overline{v'w'}^2\right]^{1/2}$), z is the measurement height (42.7 m), $z_o$ is the roughness length for momentum, and $\Psi_m$ is the integral diabatic correction factor for momentum applied under non-neutral conditions. Under unstable conditions, $\Psi_m$ is negative, indicating that the wind speed at some height would be less than in neutral conditions, while a stable atmosphere has the opposite effect (Campbell and Norman, 1998). In order for $\Psi_m$ to be neglected in Equation (3.8), neutral conditions were selected when the non-dimensional stability variable, $\zeta$, was > -0.02 and < 0.02. Stability was defined as $\zeta = \frac{z-d}{L}$, where $L$ is the non-dimensional Obukhov length, $L = \frac{T_v u_*^3}{kg\overline{w'\theta_v'}}$, where $T_v$ is the virtual temperature, $g$ is acceleration due to gravity and $\overline{w'\theta_v'}$ is the covariance of vertical velocity and the virtual potential temperature.

Rearranging Equation (3.8) assuming near-neutral conditions and setting $z_o$ to an arbitrary proportion of $d$, given by $a = z_o/d$, resulted in the following expression (Simpson, 1996),

$$d = \frac{z}{1 + a\exp\left(ku / u_*\right)} \qquad (3.9).$$

Zero-plane displacement was then determined using an iterative solution to Equation (3.9) as described by Simpson (1996). Near-neutral half hours, where $|\zeta| < 0.02$, were selected between October 15, 1997 and May 31, 1999 using an initial $d$ equivalent to $0.67h$. The $u/u_*$ ratios measured during these half hours were grouped chronologically in bins of 20 and averaged. The average $u/u_*$ values were input to Equation (3.9) to find $d$. The values of $d$ were then averaged to obtain a new $d$ with which near-neutral half hours were re-selected and the calculations repeated. This iteration was continued until $d$ no longer changed significantly.

When $a = z_o/d$ was set to 0.10, 0.15 and 0.19 and held constant through each iteration, mean $d$ for the measurement period was found to be 24.74 ± 0.11 m, 20.55 ± 0.12 m, and 18.14 ± 0.13 m after 2 iterations with a final n = 108, 84, and 72, respectively. Zero-plane displacement was consistent throughout both summer and winter months. Assuming $z_o$ to be $0.15d$ for this forest, $d$ was chosen to be 20.55 m, or about $0.62h$ with the resultant $z_o$ equal to $0.09h$. These were similar to the values of $d = 0.61h$ and $z_o = 0.11h$ found using wind profile measurements over a 10.4 m tall *Larix leptolepsis* forest with a similar tree form and LAI of 3.6 (Allen, 1968, cited by Jarvis et al. 1976). Typical values for $d$ have been found to be $0.67h$ (Oke, 1987) and specifically for forests, in the range from $0.61h$ to $0.92h$ (Jarvis et al., 1976). However, the spired nature of the closed Douglas-fir canopy likely accounts for the increased depth at which momentum is absorbed despite the high density of this stand. The value of $z_o$ was ultimately taken as 3.3 m for subsequent analyses based on $0.1h$ (Campbell and Norman, 1998).

### 3.4.2 Calculation of Aerodynamic Conductance

The transfer of heat and water vapour between the forest canopy and the atmosphere depends upon turbulent diffusion processes whereas momentum is transferred primarily by pressure forces (Verma, 1989). As a result, an excess resistance to the transfer of heat and mass should be accounted for. The aerodynamic resistance for momentum ($r_{a,m}$) may be calculated using a manipulation of Fick's Law (flux gradient form) and the log wind profile,

$$r_{a,m} = \frac{\left(\ln\left[(z-d)/z_o\right] + \Psi_m\right)^2}{k^2 u} \tag{3.10}$$

where $z_o$ is the roughness length for momentum, specifically. Using direct measurements, aerodynamic resistance for momentum may be expressed as,

$$r_{a,m} = \frac{u}{u_*^2} \tag{3.11}$$

where $u$ is the average horizontal wind speed and $u_*$ incorporates the effects of stability. To account for the excess resistance for the transfer of heat and water vapour transfer, the aerodynamic resistance for heat and water vapour transfer ($r_{a,h}$) is expressed as,

$$r_{a,h} = \frac{u/u_* + 2/k + (\Psi_h - \Psi_m)/k}{u_*} \tag{3.12}$$

where $\Psi_h$ is the integral diabatic correction factor for sensible heat transfer. This is a manipulation of the transfer equation for heat, the log wind profile and includes the assumption that the relationship between the roughness length for momentum and for heat and water vapour is $\ln(z_o/z_{o,h}) = 2$ (Garratt and Francey, 1978). This is an approximation since Garratt and Francey (1978) found $\ln(z_o/z_{o,h})$ in the range of 0.8 to 1.8 for pine forested areas. All aerodynamic conductance ($g_a$) or resistance values in this study, where $g_a = 1/r_a$, were determined with Equation (3.12). To avoid unreasonably large $r_a$ due to low $u_*$ measurements, $u_*$ was recomputed when less than 0.2 m $s^{-1}$ using $u$ and the log wind profile accounting for stability shown in Equation (3.8).

## 3.5 RELIABILITY OF EDDY FLUXES

### 3.5.1 Spectral Analyses

In order to determine if reliable measurements of $u$, $v$, $w$ and $T$ by the sonic anemometer and of $\chi_w$ by the IRGA were obtained during variable weather conditions, power spectra and cospectra for each of these variables were analyzed. Three case studies were chosen representing successive half hours measured during the daytime under rain-free, light and heavy rainfall conditions. Spectral densities, $S(n)$ of $u$, $v$, $w$, $T$ and $\chi_w$ were calculated using a fast Fourier transform with a boxcar filter (rectangular window) for each half hour and block-averaged over the logarithmic scale. Non-dimensional spectral densities were achieved by normalizing with frequency, $n$ and variance, $\sigma^2$, as $nS(n)/\sigma^2$. Co-ordinate rotation and detrending procedures were not applied to the time series prior to spectral analysis. Plots of frequency weighted spectral densities, $nS(n)$ vs. $n$ indicated possible spectrum distortion at the low frequency range (Kaimal and Finnigan, 1994) for $T$ only. These were confirmed by observable trends in the time series figures for $T$. Trends were not physically expected for the velocity components and were not found within the spectral plots or time series selected for this analysis. However, trend removal had no discernible effect on $S(n)$ for any variable recorded during the ideal conditions case study on June 8, 1998. As a result, for a worse case situation, the location of spectral peaks may be unreliable within the power spectra plots for $T$ (Kaimal and Finnigan, 1994). Cospectra of $\overline{u'w'}$, $\overline{w'T'}$ and $\overline{w'\chi_w'}$ were calculated using the above method and normalized using $n$ and the covariance. In order to make comparisons between different times and stability regimes, spectral peaks were successfully matched using $n(z - d)/u$ scaling derived as a mean over the measurement period for each case study where $z - d$ corresponded to 22.2 m.

### 3.5.2 Closed Path vs. Open Path $\lambda E$

Latent heat flux was measured using both a closed path IRGA and an open path krypton hygrometer. To ensure that signal loss was not occurring within the closed path system due to

inadequate flow rates or tubing problems, cospectra of $w\chi_w$ measured using the IRGA and $w\rho_v$ measured using the open path krypton hygrometer were compared with cospectra of $wT$ measured using the sonic anemometer during sunny, clear sky conditions (Fig. 3.3). Sensible heat fluxes derived from sonic anemometer measurements were free from sensor separation errors and signal attenuation problems due to the sampling tube, while $\lambda E$ derived from the open path krypton hygrometer were free from problems associated with the sampling tube such as flow distortion and signal attenuation effects (Blanken et al., 1997). There was excellent agreement between the open and closed path measurements of $\lambda E$, especially in the high frequency range (Fig. 3.3). Blanken et al. (1997) found similar agreement using the same instruments within the understory of an aspen forest. These results indicated that under ideal conditions with low humidity and strong atmospheric turbulence (RH = 53.8 ± 0.8 %, $u_* = 0.42$ ± 0.02 m $s^{-1}$, $\zeta$=-1.45 ± 0.38 where means are reported to ± 1 SE), the closed path measurements did not suffer from significant signal attenuation in the sampling tubes. Furthermore, comparisons of $wT$ and $w\chi_w$ indicated that there was no apparent flux loss in the high frequency range such that sensor separation errors did not appear to be significant.

Thus, Moore's (1986) corrections dealing with sensor separation effects were apparently not required under these conditions and were not applied. Corrections for non-ideal instrumentation frequency response and flow distortion due to the sampling tube were not applied (Massman, 1991; Moore, 1986). Other studies have found the need to use these corrections following Moore (1986) (Gash et al., 1999; Kelliher et al., 1998). However, Laubach and Teichmann (1996) determined that corrections for signal attenuation effects most likely due to adsorption and desorption of water vapour on the tube walls during high humidity conditons (see Section 4.1) resulted in corrections of $\lambda E$ between 2% and 14%, while the effect for corrections for velocity profiles within sampling tube and gas analyzer frequency response characteristics were less than half of these.

Comparable $wT$ and $w\chi_w$ cospectra shapes and peaks at the same frequencies suggest similar transfer mechanisms of $H$ and $\lambda E$ during unstable, daytime conditions (Yang, 1998). The discrepancy between the normalized peak values of $wT$ and $w\chi_w$ or $w\rho_v$ (Fig. 3.3) was likely a result of some differences in the contribution of low frequency fluctuations to the mean covariance. At low frequencies, few repetitions within the half hour were possible such that errors were more heavily weighted and resulted in an erroneous negative correlation between $w$

and $\chi_w$, for example. In addition, as there was little contribution to the total covariance at frequencies ($n$) beyond 1 Hz, no loss of covariance in the high frequency range was likely with a sampling rate of 20.83 Hz allowing 10 Hz signals to be resolved. However this was limited by the IRGA itself, which has a response time of 0.1 s allowing signals of up to 5 Hz to be resolved in a best-case situation (LI-COR, 1996).

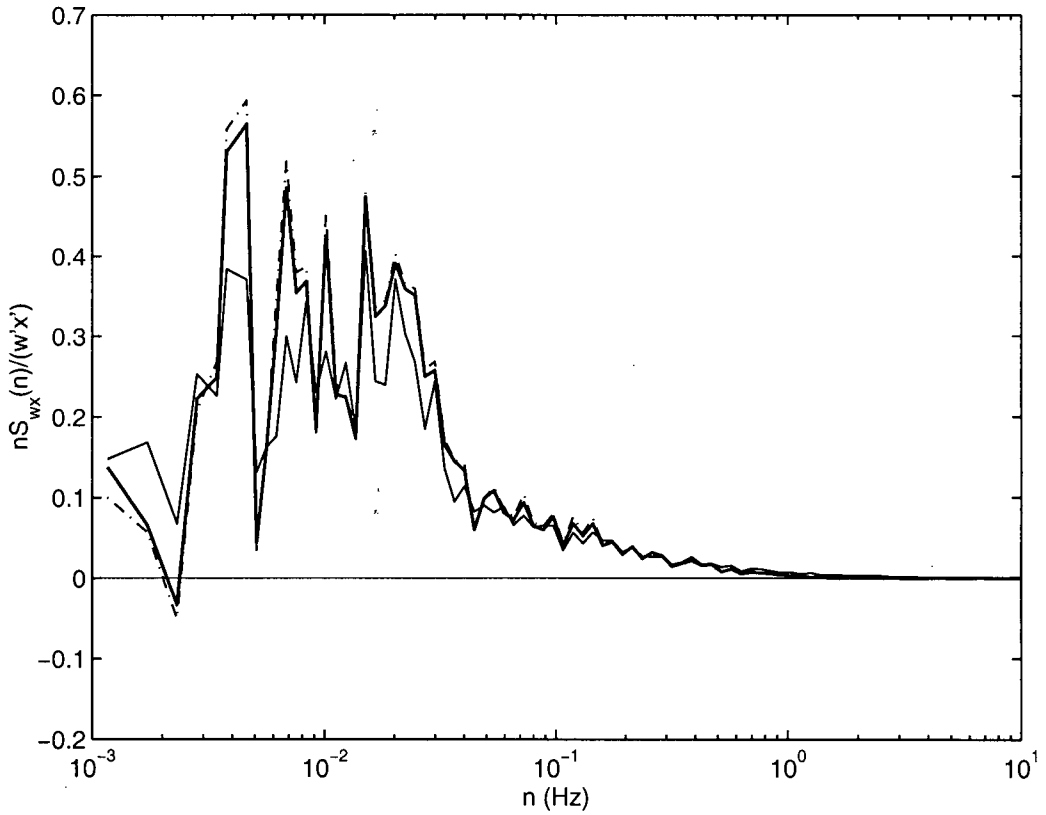


Fig. 3.3 Normalized cospectra of $wT$ (solid thin line), $w\rho_v$ measured using an open path krypton hygrometer (dash-dotted line) and $w\chi_w$ measured using a closed path IRGA (thick solid line). All traces are means of 7 half hour fluxes measured at 42.7 m ($z$) above the ground during clear sky conditions June 8, 1998 between 08:30 h and 14:30 h.

### 3.5.3 Monin-Obukhov Similarity

Monin-Obukhov similarity theory was also used to investigate the sonic anemometer performance in inclement weather. Measurements of the non-dimensional standard deviations of $w$ and $T$, $\phi_w = \sigma_w / u_*$ and $\phi_T = \sigma_T / T_*$, respectively, where $T_* = -\left(\overline{w'T'}\right) / u_*$, were compared with the values predicted by the Businger-Dyer formulations (Kaimal and Finnigan, 1994). Data which deviated by more than 20 to 30% from the values predicted by these functions were suggested by Foken and Wichura (1996) to indicate periods of poor data quality. However, these periods were not removed from the data set outright.

### 3.5.4 Energy Budget Closure and Storage terms

Energy budget closure on a half-hourly basis is an important independent method used to ascertain the quality of the measurements of the turbulent fluxes. Fractional energy budget closure was expressed as

$$\text{Closure} = \frac{H + \lambda E}{R_n - \left(G + J + J_p\right)} \tag{3.13}$$

where $R_n$ subtracted by $G$, the rate of energy storage in the air and the biomass ($J$) and the rate of energy consumption during photosynthesis ($J_p$) is balanced by the sum of convective fluxes $\lambda E$ and $H$.

The total storage term, $J$ was expressed as

$$J = S_h + S_l + S_{nb} + S_t \tag{3.14}$$

where $S_h$ is the rate of sensible heat storage in the air, $S_l$ is the rate of latent heat storage in the air, $S_{nb}$ is the rate of heat storage in the needles and branches, and $S_t$ is the rate of heat storage in the tree boles. The first two storage components were expressed as (Lee and Black, 1993),

$$S_h = \int_0^{42.7m} \rho c_p \frac{dT}{dt} dz \tag{3.15}$$

$$S_l = \int_0^{42.7m} \lambda \frac{d\rho_v}{dt} dz \tag{3.16}.$$

Equation (3.15) was determined using the profile of eight air thermocouples ($S_{h\text{-tc}}$) and the three shielded thermistors ($S_{h\text{-HMP}}$) when the thermocouple profile was unavailable. These two

methods were very similar where $S_{h\text{-HMP}} = 1.05\ S_{h\text{-tc}} + 0.01$ W m$^{-2}$, $R^2 = 0.76$. Measurements of RH using the HMP35CF at three levels within the canopy were generally used to calculate $S_l$. The following relationship was found for $S_l$ calculated using a four-level profile measured with the IRGA for a two week period, $S_{l\text{-HMP}} = 0.77\ S_{l\text{ IRGA}} + 0.08$ W m$^{-2}$, $R^2 = 0.78$. The rate of storage in the branch and needle biomass, $S_{nb}$ was approximated using 30% of $S_h$ as,

$$S_{nb} = 0.3 S_h \tag{3.17}$$

based on the method of Lee and Black (1993) in a Douglas-fir forest. This was reasonable within the error of this measurement as thin branches and needles followed air temperature quite closely. The method for determining $S_t$ used direct measurements of the change in temperature within the tree boles. Dividing the boles into concentric volumes of wood with associated temperatures, the heat storage was then calculated using the density and heat capacity of the wood in each annulus and scaled on a per meter basis using tree height, a tree form factor to account for bole tapering, $F_f$ (see Appendix D) and stand density, $S_D$ as expressed in the following equation (Blanken, 1997),

$$S_t = S_D F_f h \pi \sum_{i=1}^{n} (r_i^2 - r_{i-1}^2) \rho_t C_t \frac{\partial T_{t\,i}}{\partial t} \tag{3.18}$$

where $S_D = 1054$ trees ha$^{-1}$, $h$ is the height of the canopy = 33 m, $r$ is the radius of each annuli, $\rho_t$ is the wood density and $C_t$ is the wood heat capacity associated with each annuli and $dT_{ti}/dt$ is the rate of change in annulus temperature with respect to time, $t$. Forest characteristics such as $S_D$ and mean diameter were determined using a 33 m by 33 m plot at the site. Tree thermal characteristics were taken from Cohen et al. (1985) and are listed in Table 3.1. Measurements from two reference trees with the properties described in Table 3.1 were used to calculate $S_t$ and averaged when both measurements were available. The second reference tree was measured at 3 and 27 m above the ground in order to account for any differences in heat storage with height. On average, the difference between the absolute values of $S_t$ calculated using both top and bottom values scaled for 1/3 and 2/3 of the tree respectively, and $S_t$ calculated using the bottom only was 1.29 ± 0.01 W m$^{-2}$. The mean absolute values of $S_t$ for the top and bottom between August 20, 1998 and May 31, 1999 was 7.64 ± 0.07 W m$^{-2}$, while for the bottom only, the mean was 6.34 ± 0.06 W m$^{-2}$, all with n = 12592. Maximum differences never exceeded ± 15 W m$^{-2}$ such that tree temperature measurements at the 3 m height was adequate. It was necessary to assume that the thermal behaviour of these two reference trees represented the whole canopy as suggested by McCaughey and Saxton (1988). The mean difference found between the absolute

values of $S_t$ calculated for the two reference trees was significant at 2.04 ± 0.03 W $m^{-2}$ with the mean absolute values of $S_t$ for the first reference tree lower at 5.60 ± 0.05 W $m^{-2}$, n = 12592. Thus, with half hour differences between the two trees occasionally as great as -42 to +49 W $m^{-2}$ (generally during sunrise or sunset), it was important to be wary of the homogeneity assumption and include some replication regardless of the appearance of this relatively homogeneous, even-aged stand.

Table 3.1 Tree thermal characteristics associated with tree annuli (Cohen et al., 1985). $F_f$ is the ratio of "true" volume to cylindrical volume using the radius at the thermocouple location (Appendix D).

| Tree (thermocouple location) | Annuli Radii, $r$ (m) | Wood density, $\rho_t$ (kg $m^{-3}$ tree) | Heat capacity, $C_t$ (J $kg^{-1}$ $°C^{-1}$) | $F_f$ |
|---|---|---|---|---|
| Tree #1 | 0.164 | 1148 | 2686 | 0.49 |
| (3 m) | 0.124 | 757 | 1400 | |
| | 0.064 | 757 | 1400 | |
| Tree #2 | 0.15 | 1148 | 2686 | 0.72 |
| (3 m) | 0.10 | 757 | 1400 | |
| | 0.03 | 757 | 1400 | |
| Tree #2 | 0.0279 | 1148 | 2686 | 3.5 |
| (27 m) | 0.0254 | 757 | 1400 | |

The final term in the energy budget, $J_p$ was not included in energy budget analyses or available energy calculations. This term may account for 1% to 4% of $R_n$ (Stewart and Thom, 1973) and was determined to not exceed 5 W $m^{-2}$ in an aspen forest (Blanken, 1997) where $J_p$ would likely be larger than in this particular coniferous forest.

### 3.5.5 Flux Footprints

Various methods are available to estimate the upwind source area of the flux to address concerns that local advection of flux from surrounding areas may be influencing measurements determined using the eddy covariance method (Leclerc and Thurtell, 1990; Schuepp et al., 1990). Using an analytical solution of the diffusion equation, the upwind area which is most likely to

affect flux measurements was determined following a procedure developed for neutral conditions by Gash (1986) and outlined by Schuepp et al. (1990). Taking the derivative of an approximate solution for diffusion of a scalar resulting from an "infinite crosswind line source" and assuming a logarithmic profile for wind speed with height, the following expression describing the relative contribution from an upwind distance ($x$) to the vertical flux at a given height $z$ is obtained (Schuepp et al., 1990),

$$\frac{1}{Q_o}\frac{dQ}{dx} = -\frac{u(z-d)}{ku_* x}\exp\left[-u(z-d)\Big/\left(ku_* x\right)\right] \tag{3.19}$$

where $(1/Q_o)(dQ/dx)$ is the relative flux density per unit distance, $u$ is the average horizontal wind speed at measurement height ($z$) assumed to be constant, $u_*$ is friction velocity, $k$ is von Karman's constant and $d$ is the zero-plane displacement. The distance upwind at which the vertical flux will most strongly influence the measured flux, i.e. the position of the peak of the footprint ($x_{max}$), is obtained by setting the first derivative of Equation (3.19) to zero, which gives (Schuepp et al., 1990),

$$x_{\max} = \frac{u}{u_*}\frac{(z-d)}{2k} \tag{3.20}.$$

Integrating Equation (3.19) describes the cumulative normalized contribution of source areas to the flux measurement, from a distance $x$ upwind (Schuepp et al., 1990),

$$\frac{Q(x)}{Q} = \exp\left(\frac{-u}{u_*}\frac{(z-d)}{k\,x}\right) \tag{3.21}.$$

The upwind distance predicted to account for 80% of the flux will contract under unstable conditions and increase under neutral and stable conditions. Rather than apply corrections for stability to the $u/u_*$ ratios in the above formulations which were developed using neutral condition assumptions (Schuepp et al., 1990), the linear relationship between $u$ and $u_*$ was determined for this site stratified by stability under conditions of adequate turbulence ($u_* >$ 0.2 m s$^{-1}$). The resultant $u/u_*$ ratios (taken as the slope of the regressions) for stable, neutral and unstable conditions were then used in Equations (3.20) and (3.21) to determine average flux footprint characteristics for the site.

### 3.5.6 Data Screening and Corrections for Latent Heat Fluxes

All flux measurements were screened to remove obvious eddy covariance instrumentation and sampling problems. This consisted of removing half hours with 1) excessive spikes in the sonic anemometer data when $\sigma^2_w > 5\ m^2\ s^{-2}$ and $\overline{w'T'} > 1\ m\ s^{-1}\ °C$, 2) the occurrence of calibrations, and 3) mechanical problems with instrumentation. Fluxes were also rejected when unreasonably large magnitudes of $H$ ($-400\ W\ m^{-2} > H > 600\ W\ m^{-2}$) or $\lambda E$ ($-100\ W\ m^{-2} > \lambda E > 500\ W\ m^{-2}$) were observed. Periods were flagged when sampling flow rates for the IRGA were low due to pump problems but not removed outright. Unlike other groups using the eddy covariance technique, periods with rainfall were not rejected as will be discussed in Section 4.1 (Anthoni et al., 1999). These procedures removed 3% of the eddy flux measurements throughout the study period between October 15, 1997 and May 31, 1999. For seasonal and annual totals of $\lambda E$ , missing half hour $\lambda E$ values were calculated as the residual of the energy budget when $H$ was available or simply interpolated when energy budget components were not available.

A variety of methods are available with which $\lambda E$ may be corrected when it is believed to be underestimated. When poor energy budget closure indicates convective fluxes may have been underestimated, a Bowen ratio correction may be applied as follows (Blanken et al., 1997),

$$\lambda E_{new} = \frac{R_a}{1+\beta}\ ;\ H_{new} = \frac{\beta}{1+\beta} R_a \qquad (3.22)$$

where $\beta = H/\lambda E$ and is used to make the same relative increase in both $\lambda E$ and $H$ in order to equal the available energy flux, $R_a$. The Bowen ratio correction is not useful for periods when $1.2 > \beta > -0.8$ as the small denominator can cause $|\lambda E|$ to become unreasonably large. Anticipating our results of Section 4.1, $\lambda E$ may also be corrected for high frequency losses associated with signal attenuation due to adsorption/desorption in the sampling tube walls for rainfall and high humidity conditions. Corrections can be accomplished using an empirical transfer equation based on sonic-measured $T$ spectra or $wT$ cospectra over the entire frequency range (Laubach and Teichmann, 1996) or by accounting for the flux loss in only the high frequency range. However, under conditions when possible flux loss to only the $\lambda E$ measurements may occur, the Bowen ratio method, which assumes both $H$ and $\lambda E$ are underestimated by equal proportions, does not apply. Finally, all of these methods require the sonic anemometer-thermometer to perform adequately under rainfall and high humidity

conditions. Support for this is discussed in Section 4.1 and has been found by other groups in wind tunnel experiments (Mizutani et al., 1997) and field studies (Gash et al., 1999; Laubach and Teichmann, 1996). Fig. 3.4 illustrates the different effects of applying a Bowen ratio and a signal attenuation correction associated with a 38% total flux loss for a 24 h period during dry and wet summer conditions (see Table 4.1 for detailed information regarding June 8 and July 14, 1998). These corrections had virtually no effect on fluxes recorded during the dry conditions, as little correction was needed, while fluxes recorded during the wet day were significantly increased.

Unless indicated, the original fluxes were used in figures and analyses. For cumulative and total values, the following correction steps were followed:

1. Choose $\lambda E$ values associated with delay times > 40 or < 0 samples.
2. Multiply $\lambda E$ by 1.62 to account for maximum possible 38% flux loss due to signal attenuation (see Section 4.1).
3. Choose to apply the Bowen ratio correction or not. If not, proceed to Step 6.
4. Choose all $\lambda E$ values when $S\downarrow$ is greater than 0 W $m^{-2}$ and apply the Bowen ratio correction using Equation (3.22).
5. Remove $\lambda E$ values produced by Step 4 when -10 W $m^{-2}$ > $\lambda E$ > 600 W $m^{-2}$.
6. Fill removed values due to Step 5 and/or data screening procedure using energy budget method (i.e. $\lambda E = R_a - H$).
7. Fill remaining missing values by linear interpolation.

Reported means, ratios and typical values include the range of values possible using the various corrections not including filled or interpolated values unless otherwise indicated.

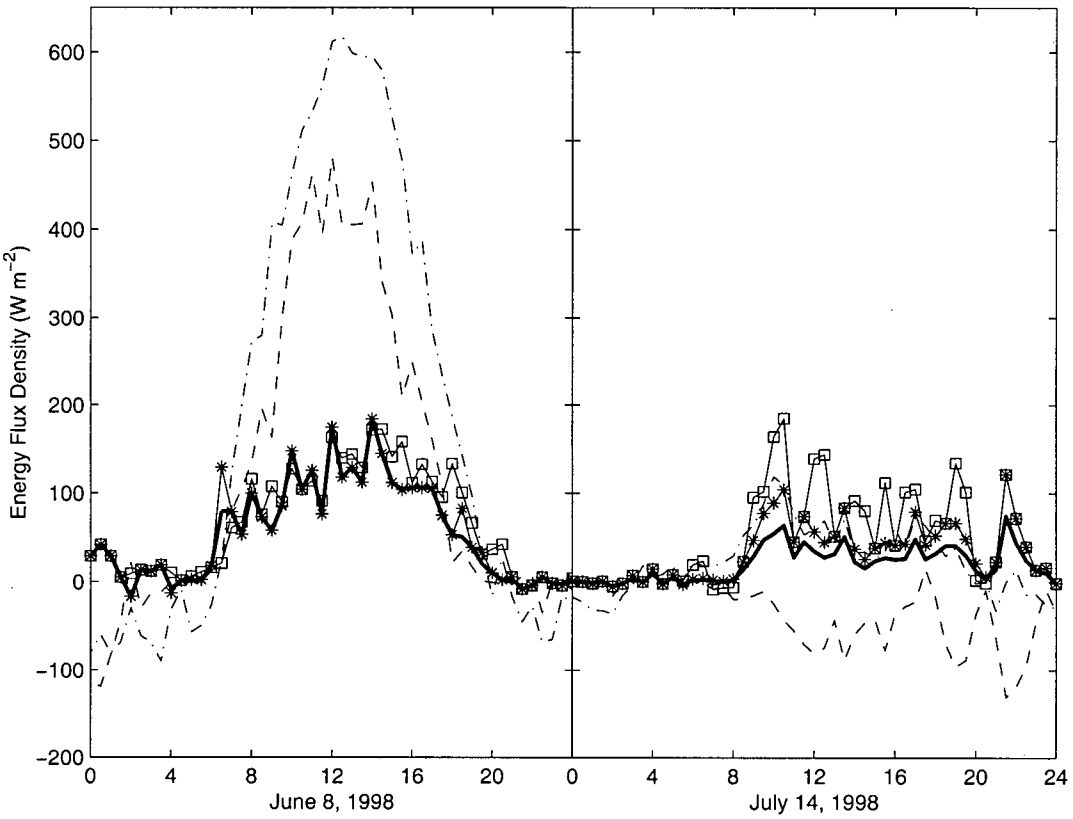


Fig. 3.4 Effects of $\lambda E$ corrections for two days. Measured $\lambda E$ is shown (heavy solid line) with $R_a$ (dash-dotted line) and $H$ (dashed line). $\lambda E$ corrected for a maximum possible 38% flux loss (✳) due to signal attenuation when calculated delays > 40 samples or < 0 samples are shown with $\lambda E$ corrected with the Bowen ratio correction (□) subsequent to the attenuation correction if needed.

# 4. RESULTS & DISCUSSION

## 4.1 EDDY COVARIANCE INSTRUMENTATION PERFORMANCE DURING RAINFALL AND HIGH HUMIDITY CONDITIONS

During the winter months of this study (November to March), 17% and 23% of the half hours recorded rainfall during the 1997/98 and 1998/99 seasons, respectively. To avoid excluding these measurements, it is critical to be confident in the performance of the eddy flux instrumentation, namely the sonic anemometer and the IRGA, under rainfall conditions.

The sonic anemometer is susceptible to problems during rainfall as rain drops crossing the array may appear as spikes in the time series, increasing the variance of the velocity and temperature signals and therefore, causing false contributions to the cospectral density throughout the frequency range. In addition, a depth of water covering a sonic transducer affects arrival time of the sonic wave because sound travels 4.2 times faster in water than in air (Mizutani et al., 1997). The Gill sonic anemometer used in this study is specifically designed to minimize the influence of rainfall on the measurements. The sonic transducers are arranged such that none are horizontal and are coated in a hydrophobic material with drip points on the undersides (Gash et al., 1999). Results from wind tunnel experiments investigating the response of velocity components and sonic-derived air temperature using the Kaijo Denki, DAT 300/TR-61C and DA-600/TR-61A models indicated that errors were not evident in either power spectra or standard deviations with water sprinkling intensities $\leq 3$ mm $h^{-1}$ (Mizutani et al., 1997). In the field, Mizutani et al. (1997), found that the power spectra of $T$ deviated from the -2/3 slope in the high frequency range above 3 Hz; however, the cospectral density in this range was essentially zero and did not result in over or underestimation of flux. Field investigations with the Gill Solent Model A101R2's velocity components showed no significant deviations from the -2/3 power law when plotted as power spectra during both dry and rainy periods under near neutral conditions ($-0.1 \leq \zeta \leq 0.1$) (Gash et al., 1999).

The reliability of a closed-path IRGA to measure scalar components such as $\chi_w$ and $\chi_c$ is dependent on the tubing and air flow rates into the sample cell as the IRGA itself is isolated from

ambient conditions by way of a thermostatted box and heated sampling tube. However, there is an increased likelihood of attenuation of the signal by water vapour condensation and evaporation or adsorption and desorption at the walls of the sampling tube under high humidity conditions typical of rainfall periods (Laubach and Teichmann, 1996). As a result, fluctuations in the high frequency range would be damped and result in a loss of flux attributable to these frequencies.

Generally, rainfall intensities at Campbell River were less than 3.0 mm $h^{-1}$. About 64% of the half hours with recorded rainfall had rainfall intensities $\leq$ 1.0 mm $h^{-1}$. However, 11% of these half hours had rainfall intensities in excess of 3.0 mm $h^{-1}$. In order to investigate the sonic anemometer and IRGA performance during rainfall and high relative humidity, power spectra and cospectra associated with these measurements and the behaviour of turbulence statistics within the surface layer were analyzed.

### 4.1.1 Spectral Analyses

#### 4.1.1.1 Power Spectra

"Spectral analysis allows examination of the various frequency contributions to the time series" (Amiro, 1990). Of particular interest is the inertial subrange within surface layer spectra where energy is neither produced nor destroyed but is found to cascade to smaller and smaller scales (Kaimal and Finnigan, 1994). Within this range, the frequency normalized energy density ($nS(n)/\sigma^2$ ) decreases as $n^{-2/3}$, where $n$ may be expressed in Hz or as a non-dimensional frequency, $n(z-d)/u$ for steady-state turbulent flow conditions (Kaimal and Finnigan, 1994). This expected behaviour is useful in order to test the ability of eddy covariance instrumentation to function in variable weather and weak turbulence conditions. Groups of relatively unchanging half hours during the daytime were chosen to represent (i) ideal, dry conditions, (ii) conditions with moderate humidity and light rain ( $P \geq 0.25$ mm $h^{-1}$, mean $P < 2.0$ mm $h^{-1}$ ) and (iii) conditions with high humidity and heavy rain ( $P \geq 0.25$ mm $h^{-1}$, mean $P \geq 2.0$ mm $h^{-1}$ ) (Table 4.1). Power spectra of $w$, $T$ and $\chi_w$ for these situations are compared in Fig. 4.1.

Vertical velocity spectra demonstrated no significant measurement problems during rainfall conditions (Fig. 4.1). Within the inertial subrange, $w$ spectra were found to decrease as $n^{-2/3}$ (with slopes equal to -0.66, -0.70, and -0.66 for dry, light and heavy rainfall conditions for non-dimensional frequencies between 2 and 20). Although measurements were only 9.7 m above the canopy and therefore, within the roughness sublayer, these results suggested that turbulence structure at this level was similar to that of the inertial sublayer generally believed to be attained at heights near 2 to 3$h$ (Kaimal and Finnigan, 1994; Wilson and Schuepp, 1987). In addition, normalized spectral peaks were observed to shift to higher frequencies with increasingly stable conditions (Kaimal et al., 1972). This was likely a result of lower frequency turbulent motions being more strongly damped by buoyancy forces (Stull, 1988). Spectra of $u$ and $v$ (not shown) appeared to have slightly steeper slopes within the inertial subrange for non-dimensional frequencies between 2 and 20 (-0.67, -0.70, -0.73 and -0.72, -0.67, -0.74 under rain-free, light and heavy rainfall for $u$ and $v$ respectively). However, these varied little with rainfall conditions and continued to indicate satisfactory measurements during inclement weather.

Table 4.1 Mean energy budget, weather conditions and turbulence conditions measured during sessions chosen for spectral analysis. Overbars indicate means followed by ± 1 SE. The half hours used for mean spectra calculations were recorded during the daytime (when $S\downarrow > 0$)

| Case | Ideal | Light rain | Heavy rain |
|---|---|---|---|
| Study | June 8, 1998 | March 30, 1999 | July 14, 1998 |
| No. of half hours | 12 | 5 | 19 |
| $\overline{P}$ (mm/30 min) | 0.0 ± 0.0 | 0.81 ± 0.22 | 1.04 ± 0.16 |
| $P_{max}$ (mm/30 min) | 0.0 | 1.52 | 2.28 |
| $\overline{u}$ (m s$^{-1}$) | 2.26 ± 0.09 | 1.71 ± 0.25 | 4.77 ± 0.16 |
| $\overline{u_*}$ (m s$^{-1}$) | 0.42 ± 0.02 | 0.36 ± 0.05 | 0.98 ± 0.05 |
| $\overline{\zeta}$ | -1.454 ± 0.380 | -1.232 ± 0.378 | 0.014 ± 0.002 |
| $\overline{\mathrm{RH}}$ (%) | 53.8 ± 0.8 | 71.1 ± 2.8 | 100.0 ± 0.0 |
| $\overline{H}$ (W m$^{-2}$) | 349.5 ± 29.9 | 159.3 ± 24.3 | -51.4 ± 5.8 |
| $\overline{\lambda E}$ (W m$^{-2}$) | 102.0 ± 9.7 | 145.8 ± 13.7 | 36.5 ± 3.0 |
| $\overline{R_a}$ (W m$^{-2}$) | 511.4 ± 45.9 | 413.2 ± 40.8 | 60.6 ± 6.1 |
| $\overline{\left(\frac{H+\lambda E}{R_a}\right)}$ (%) | 89.2 ± 2.4 | 74.0 ± 5.0 | -41.8 ± 12.9 |

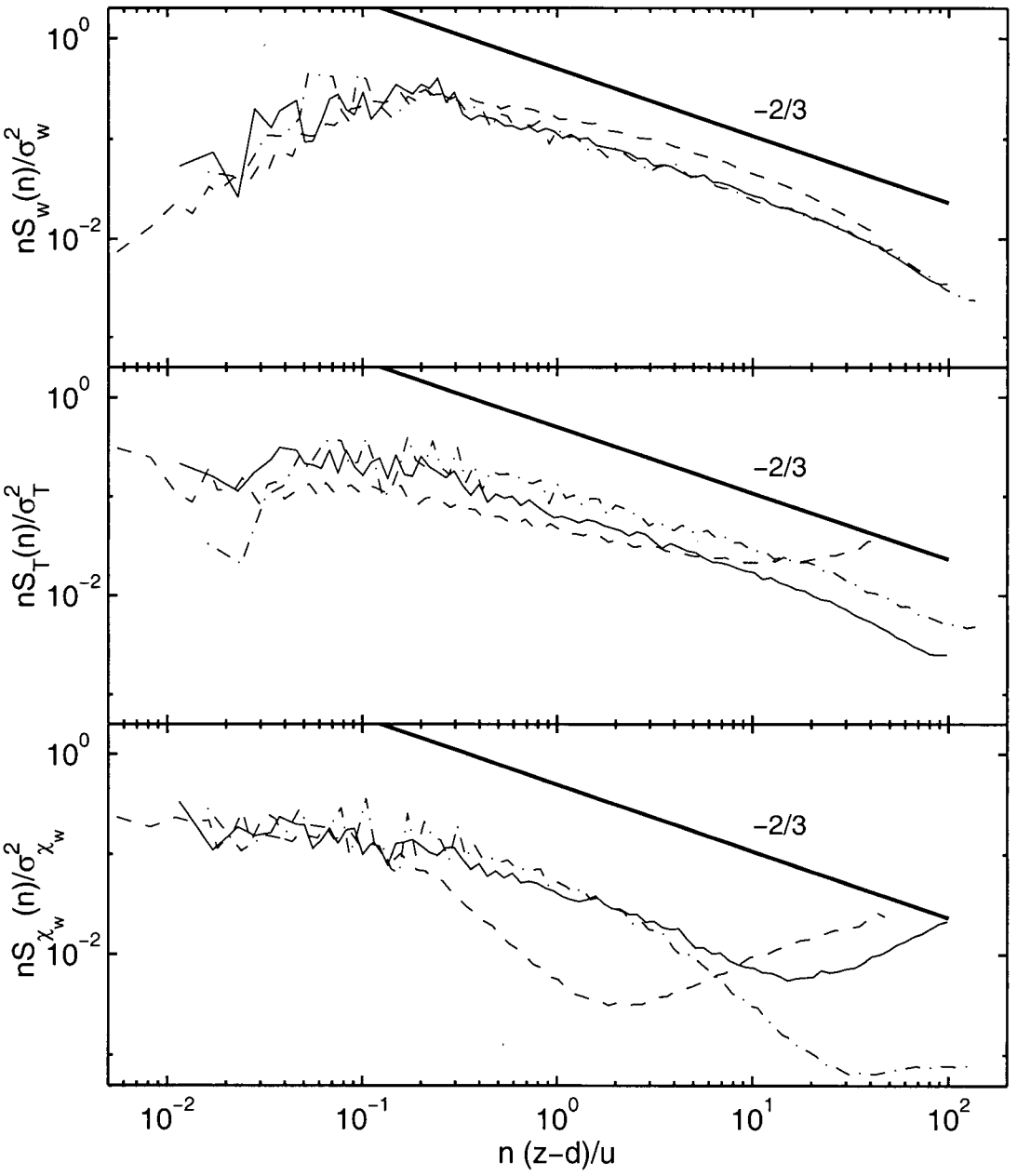


Fig. 4.1 Normalized logarithmic power spectra for vertical velocity ($w$), air temperature ($T$) and water vapour ($\chi_w$) during the daytime experiencing zero rainfall on June 8, 1998 (solid line), light rainfall on March 30, 1999 (dash-dotted line) and heavy rainfall on July 14, 1998 (dashed line). The -2/3 slope is shown for the inertial subrange. Non-dimensional frequency was derived using the mean wind speed recorded during these measurements: 2.24, 1.71, and 4.77 m $s^{-1}$, respectively (Table 4.1) and the difference between the measurement height and zero-plane displacement, ($z$-$d$ = 22.2 m).

Under rain-free and light rain conditions $T$ spectra were found to roll off near $n^{-2/3}$ in the inertial subrange for the non-dimensional frequencies between 2 and 20 (-0.661 and -0.594, respectively) (Fig. 4.1). However at the higher end of this range, spectra began to rise under heavy rainfall conditions. Spectra approached the -2/3 slope at lower non-dimensional frequencies (0.2 to 10) for rain-free, light and heavy rainfall conditions as -0.60, -0.55, and -0.39, respectively (Fig. 4.1). The deviation from a -2/3 slope in the high frequency range for $T$ spectra was also observed in field measurements by Mizutani et al. (1997). However, as in this study, the rise was found to have little effect on $H$ as the proportion of covariance attributed to the high frequency range (> 10, non-dimensional frequency) was negligible (Fig. 4.5). The rise in the spectrum under rainfall conditions was likely due to sporadic spikes in the signal from "mistriggering" in the transducers (Kaimal and Finnigan, 1994). Fig. 4.2 illustrates the high frequency time series of sonic-measured $T$ and velocity components when rainfall intensity was 4.06 mm/hr. During 30 min of measurements, only 2 isolated spikes were observed in the $T$ time series including a possible fluctuation from the mean due to a depth of water temporarily on the sonic transducer (Fig. 4.2). No spikes were found in any of the velocity time series (Fig. 4.2). When the spike was removed from the $T$ time series and replaced by a neighboring value, the rise in the $T$ spectrum was minimized.

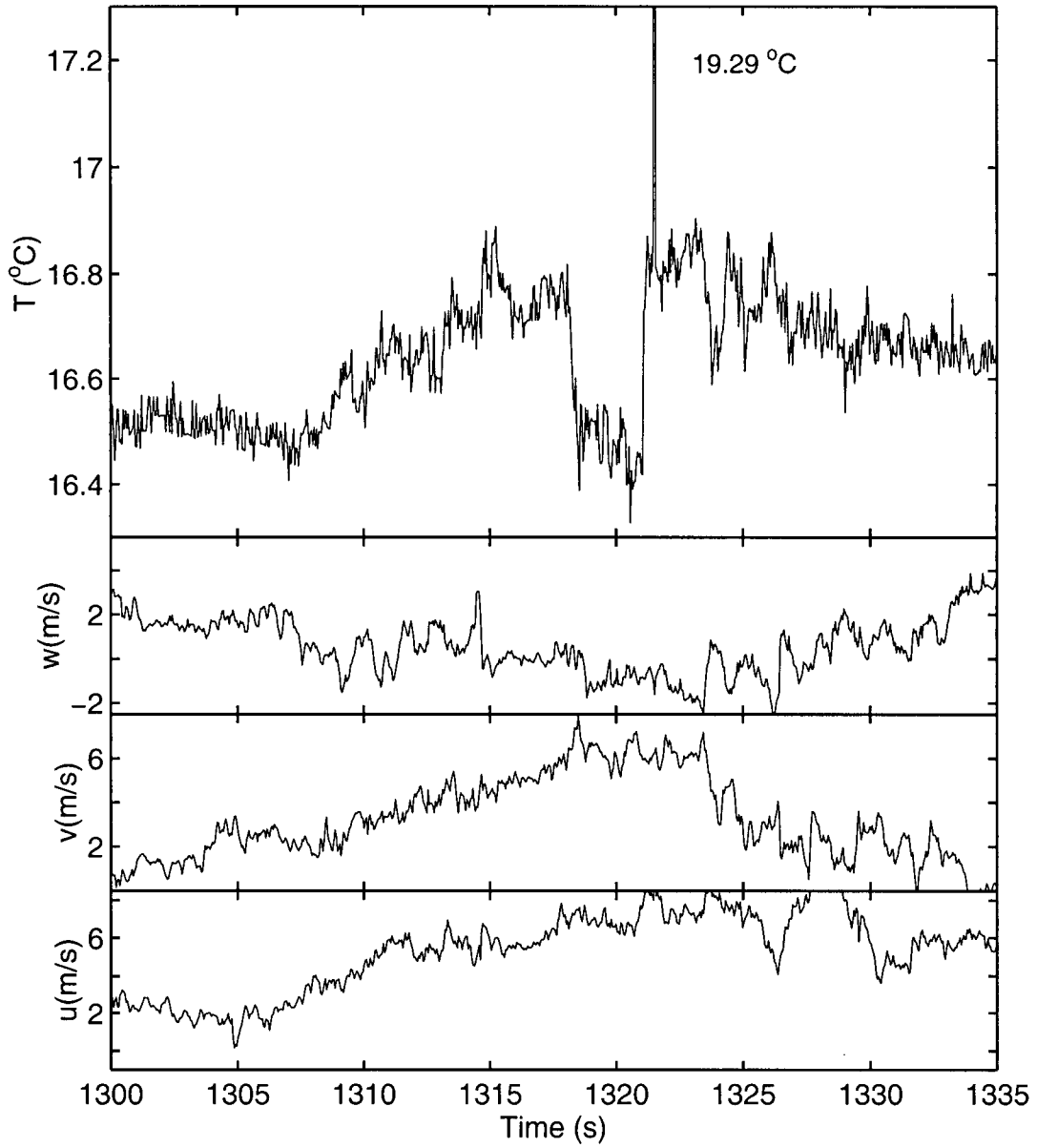


Fig. 4.2 Spikes and square wave fluctuations in $T$ associated with rainfall conditions on July 14, 1998. Velocity components generally appear unaffected. Rainfall intensity was 2.03 mm/30 min (4.06 mm $h^{-1}$) during the half hour beginning at 13:00 h.

The power spectra of $\chi_w$ were characterized by two problems with rainfall and high humidity conditions (Fig. 4.1). Slopes exceeded the -2/3 expected within the inertial subrange (Kaimal and Finnigan, 1994) and high noise levels in the high frequency range appeared to be exacerbated during rainfall conditions. For heavy rainfall, the slope was -1.47 while for light rainfall, it was -1.13 over non-dimensional frequencies of 0.1 to 1.0 compared to -0.70 over non-dimensional frequencies of 0.2 to 10, during ideal conditions. This signal loss in the high frequency range likely resulted from damping of water vapour fluctuations by adsorption/desorption or condensation/evaporation effects as the sampling tube walls approached dew point temperature under high humidity conditions. Comparisons with the power spectra for sonic-measured $T$ (Fig. 4.1), assumed to be free from signal attenuation problems, highlighted the probable effects of the tubing and air flow associated with a closed path analyzer under rainfall and high humidity conditions. It is important to note that an increased $\chi_w$ spectral slope in the high frequency range was also observed under high humidity conditions with no rainfall indicating that high humidity rather than rainfall was the condition necessary to cause this effect (see Appendix G). Throughout the measurement period, the sampling tube was held at least 10 °C higher than air temperature and did not fall below the dew point temperature of the air. The Dekabon Type 1300 tubing is a metal/plastic composite with an inner ethylene copolymer coating an aluminium layer encased by a high-density polyethylene jacket. The ethylene copolymer has minimal absorption characteristics (0.01 % dry weight gain/day, Modern Plastic Encyclopedia 1993 cited by Gramann, 1996). However the filter and a small portion of the sampling tube just prior to the IRGA were not heated until the system was replaced June 9, 1999. As a result, absorption and condensation could have occurred with high humidity within these parts of the sampling tube system.

During dry, ideal conditions, the rise in the high-frequency end of the spectrum extended just under a decade beginning at ~ 1.5 Hz, or at the non-dimensional frequency of ~15, while spectra during light rain and moderate humidity conditions began to rise at a non-dimensional frequency of ~ 30 (Fig. 4.1). During heavy rain and high humidity conditions, the rise in the spectrum began much earlier at a non-dimensional frequency between 1 and 2 (0.21 to 0.42 Hz) extending for almost two decades. The rise in the spectrum where it should be falling off had the characteristics of white noise with a slope approaching 1 in an $nS(n)$ vs $n$ plot beyond 2 Hz (slopes were 0.86 for ideal conditions and 0.62 for heavy rainfall, respectively). Evidence of white noise in the spectra can be traced to either a spike in the time series or random noise with a

normal distribution translating into equal amplitude spectral energies across the whole range of frequencies (Stull, 1988). High noise levels at the high frequency end during ideal conditions reflected the limitations of the measurement system consisting of the IRGA and data acquisition system (DaqBook 200, IOTech, Inc. Cleveland, Ohio, USA). The IRGA's signal-to-noise threshold appeared to be ~ 1.5 Hz, beyond which signal levels fell below noise levels (Kaimal and Finnigan, 1994). The IRGA had a specification response time of 0.1 s (LI-COR, 1996). This translated to a Nyquist Frequency of 5 Hz, beyond which the signal-to-noise ratio of the sensor alone would be exceeded under best-case conditions (LI-COR, 1996).

Turbulence is often weak in rainfall conditions as it is during the night resulting in reduced spectral densities throughout the frequency spectrum (Stull, 1988). This may have accounted for the spectral rise appearing at lower frequencies in rainfall conditions (Fig. 4.1). Fig. 4.3 uses simple curves representing $S(n)$ for water vapour to simulate the occurrence of the spectral rise in $\chi_w$. In Fig. 4.3 (top panel), a curve was reduced over the entire frequency range to simulate the possible reduction in $S(n)$ for night or rainfall conditions vs. the larger $S(n)$ characteristic of dry, daytime conditions. By adding the white noise to the reduced $S(n)$ curve in the frequency domain, the early rise of the final spectra was achieved (Fig. 4.3, bottom panel). However, the spectral rise in the $\chi_w$ measurements contributed little to the total flux because the proportion of flux beyond a non-dimensional frequency of 2 was small (2.4% under ideal conditions, 1.6% under light rainfall conditions, and 0.4% under heavy rainfall conditions)(Fig. 4.5).

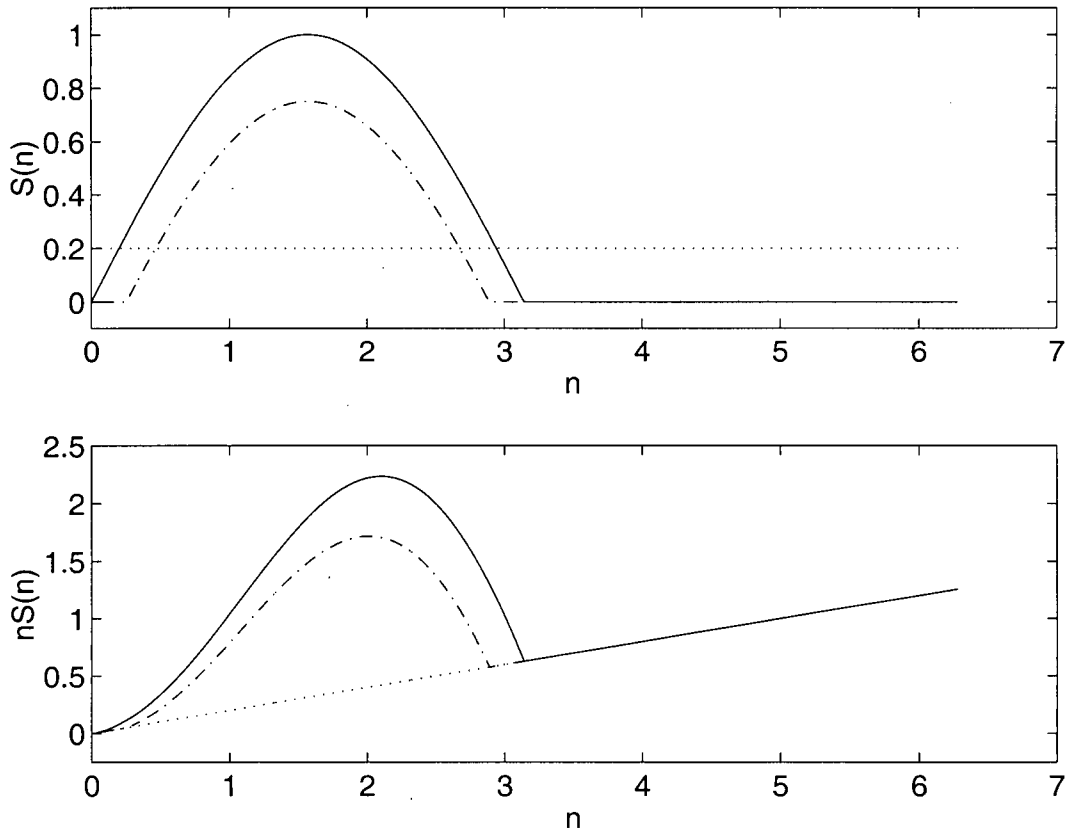


Fig. 4.3 Simulation of the effects white noise (dotted line) would have on power spectral estimates with a normal intensity (solid line) and reduced intensity (dash-dotted line). The top panel represents spectral density, $S(n)$ against frequency, $n$. The bottom panel represents frequency weighted spectral density, $nS(n)$ against $n$ where the white noise signal has been applied to the two power spectra curves.

### 4.1.1.2 Cospectra

The spectral features illustrated above are related to $\tau$, $H$, and $\lambda E$ through analysis of their cospectra, $wu$, $wT$, and $w\chi_w$, respectively (Fig. 4.4 and Fig. 4.5). Cospectra are expected to exhibit a -4/3 slope in the inertial subrange in a log-log plot (Kaimal and Finnigan, 1994). However, a spectral slope of -4/3 was not expected in the case of $w\chi_w$ and $wT$ when a clearly defined inertial subrange was not observed during rainfall conditions. During ideal conditions, it was found that over two decades between non-dimensional frequencies 0.2 to 20, cospectral

slopes for $wu$, $wT$, and $w\chi_w$ were -1.07, -0.90 and -1.27 with a tendency to become less steep in the high frequency part of the cospectrum (Fig. 4.4). Cospectra of momentum flux measured above four different boreal forests were also found to be closer to -1 than -4/3 indicating that if energy production or dissipation does not occur in the inertial subrange, then the eddy cascade of momentum and heat transport is not as rapid as expected (Amiro, 1990; Blanken, 1997). Under rainfall conditions, cospectral slopes for momentum continued to be closer to -1.

Over most of the frequency range beyond the spectral peaks, cospectral slopes for $wT$ in heavy rainfall conditions were less steep than during ideal and light rainfall conditions (Fig. 4.4). This may have resulted from the spectral rise in the high frequency end of the spectral curve for $T$ beyond a non-dimensional frequency of 10 during heavy rain (Fig. 4.1). However, the cospectral slope for $wT$ in heavy rain deviated from -1, found in ideal conditions, much earlier at a non-dimensional frequency of 0.3 with a slope of only -0.51 between non-dimensional frequencies 0.2 to 2. Using semi-log plots where the covariance is proportional to the area under the curve, Fig. 4.5 illustrates an increase in the proportion of the total flux attributed to non-dimensional frequencies beyond 0.3 in rainfall conditions. As suggested above for the power spectra curves, this may be expected as conditions become increasingly stable causing cospectral peaks to shift to higher frequencies. However, in this instance, a slight overestimation in flux was possible and may have been due to the additions to $S_T(n)$ by spikes and square waves from rain drops falling through the array paths and onto the sonic transducers.

With respect to IRGA performance during light and heavy rainfall conditions, the influence of damped high-frequency $\chi_w$ fluctuations (Fig. 4.1) on $w\chi_w$ cospectra was evident as slopes exceeded -1 to -4/3. Between the non-dimensional frequencies of 0.2 to 2, cospectral slopes in light rain and heavy rain were -1.11 and -1.95, respectively, while slopes during ideal conditions were -0.96. Beyond a non-dimensional frequency of 2, the noise-induced rise in the $\chi_w$ spectrum may have caused the cospectral curve to level somewhat for all three cases (Fig. 4.4). Again, the rise in the $\chi_w$ spectral curves in the high frequency end (beyond 2) (Fig. 4.1) had a negligible effect on the total $\lambda E$ (Fig. 4.5). However, the possible loss of flux between non-dimensional frequencies 0.2 and 2 could be considerable. The proportion of the total $\lambda E$ attributable to non-dimensional frequencies greater than 0.2 (~ 0.02 Hz) was significant. Under ideal, unstable conditions, frequencies in this range contributed 27.1% of the flux while the contribution was 33.3% under slightly unstable, light rainfall conditions and 13.8% under slightly stable, humid

conditions without rainfall (see Appendix E), and 17.5% under slightly stable, heavy rainfall conditions.

Evidence of damped high frequency $\chi_w$ fluctuations under high humidity conditions was virtually eliminated following the replacement of the sampling tube and thermostatted IRGA box with an improved system consisting of clean tubing and filters and better heating. With the new system, power spectra slopes for $\chi_w$ approached -2/3 in the inertial subrange under ideal, high humidity, and high humidity with heavy rainfall conditions (see Appendix H).

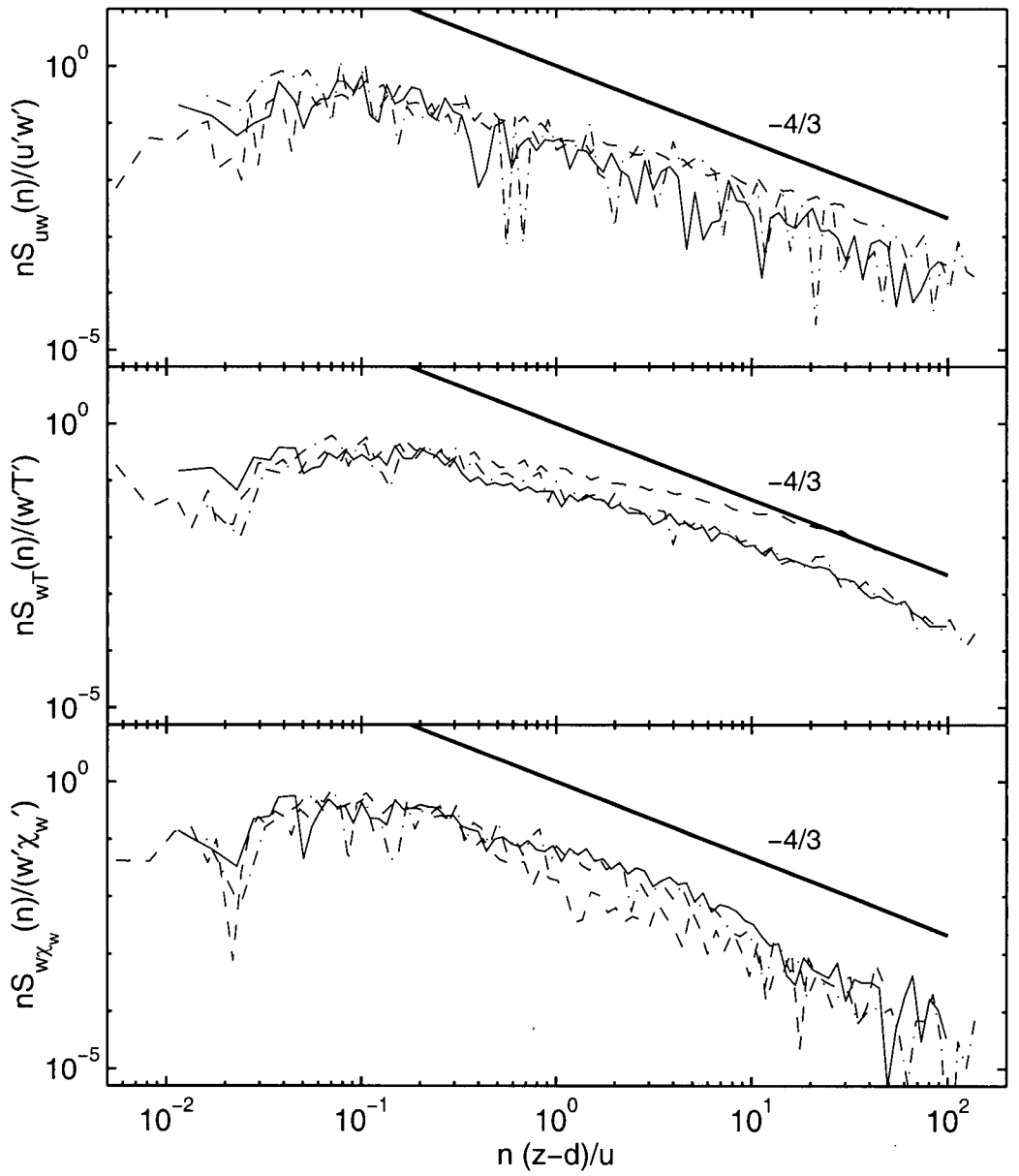


Fig. 4.4 Log-log plots of cospectra of *uw*, *wT*, and $w\chi_w$ against non-dimensional frequency during daytime conditions experiencing zero rainfall on June 8, 1998 (solid line), light rainfall on March 30, 1999 (dash-dotted line) and heavy rainfall on July 14, 1998 (dashed line) (Table 4.1). The expected -4/3 slope is shown for the inertial subrange. The non-dimensional frequency was derived as in Fig. 4.1.

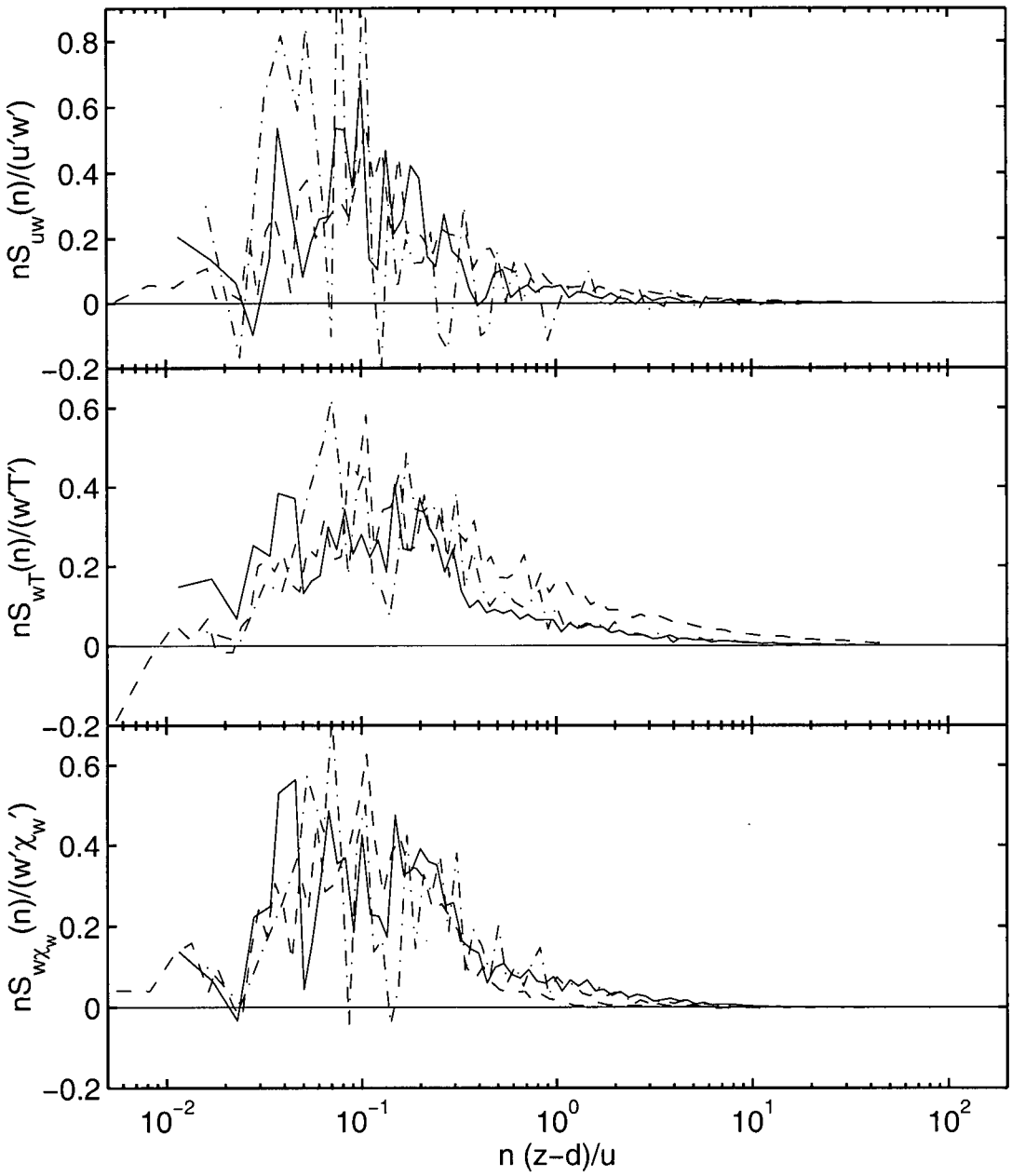


Fig. 4.5 Semilog plots of cospectra of $uw$, $wT$, and $w\chi_w$ against non-dimensional frequency during daytime conditions experiencing zero rainfall on June 8, 1998 (solid line), light rainfall on March 30, 1999 (dash-dotted line) and heavy rainfall on July 14, 1998 (dashed line) (Table 4.1). In this form, the area under any portion of the curve is proportional to the covariance. The non-dimensional frequency was derived as in Fig. 4.1.

#### 4.1.1.3 Flux Loss and Corrections

Total latent heat flux loss due to damped high frequency $\chi_w$ fluctuations was quantified and corrected using three different methods. Flux loss was calculated using the following equation,

$$R = \frac{1-b}{1-a} \tag{4.1}$$

where $R$ is the ratio of the flux with high frequency loss to the flux with no high frequency loss and $a$ and $b$ are the proportions of flux attributable to the high frequency range with and without high frequency loss, respectively, i.e. $a < b$ (see Appendix F for the derivation).

*Use of the $w\chi_w$ cospectra for a clean sampling tube*:

The cospectral forms of $w\chi_w$ after installation of the new clean tubing and heating system were used as the correct forms without flux loss. Flux loss from the case studies described in Table 4.1 could then be quantified. Since the measurements were taken at different times and stability regimes, cospectra were scaled by $n(z\text{-}d)/u$. As mentioned earlier, this is important under neutral to stable atmospheric stability, characteristic of rainfall conditions, since cospectral density peaks are shifted towards higher frequencies as lower frequency turbulent motions are more strongly damped by buoyancy forces (Kaimal and Finnigan, 1994; Stull, 1988). As a result, a greater relative proportion of the flux can be expected to be attributable to high frequency fluctuations.

In this situation, $a$ ranged from 0.175 (heavy rain) to 0.333 (light rain) and $b$ ranged from 0.306 (71% RH on June 6, 1999) to 0.378 (98% RH on June 7, 1999) beyond a non-dimensional frequency of 0.2 (see Fig H.1 for $w\chi_w$ cospectra after installation of the new tubing). As a result, $\lambda E$ measured under neutral to stable, high humidity conditions prior to the sampling tube replacement may have experienced total flux losses (i.e. 1 - $R$) of -4.1% to 6.8% (light rain) (i.e. small loss) and of 15.9% to 24.6% (heavy rain) (i.e. significant loss) when compared to the $\lambda E$ measured using the new tube.

*Use of the wT cospectra*:

Assuming similar transfer mechanisms for sensible and latent heat (Denmead and Bradley, 1985), $wT$ cospectra measured at the same time as $\lambda E$ for the case studies reported in Table 4.1 and shown in Fig. 4.5 may be used as the correct forms. This method does not require scaling to account for the different atmospheric conditions as in the first method. In addition, it does not have to be assumed that identical sensor conditions existed for either the anemometer or IRGA

between the two measurements. After applying Equation (4.1), estimates of $w\chi_w$ losses were -1.0% for ideal conditions, 5.7% for light rain and 38.3% for heavy rain conditions.

*Empirical Transfer Functions*:

Laubach and Teichmann (1996) suggested using an empirical transfer function ($T_e(n)$) to correct for high frequency loss in $\overline{w'\chi'_w}$ based on the square root of the ratio of the Fourier coefficients for $T$ and $\chi_w$ normalized by their variances,

$$T_e(n) = \left( \frac{S_{\chi_w}(n) / \sigma^2_{\chi_w}}{S_T(n) / \sigma^2_T} \right)^{1/2} \tag{4.2}$$

where the "true" covariance is determined by applying the above transfer function to the measured cospectrum, $S_{w\chi_w}(n)$ as follows,

$$\overline{w'\chi'_w} = \int_0^\infty \frac{S_{w\chi_w}(n)}{T_e(n)} dn \tag{4.3}.$$

A slightly modified form of $T_e(n)$ may be obtained by setting $T_e(n) = 1$ for frequencies less than a non-dimensional frequency of 0.2 where flux loss due to water vapour reactions at the tube walls is not expected. In addition, $S_T(n) / \sigma^2_T$ values were adjusted so that the magnitude of the low frequency values (0.01 Hz > $n$ > 0.004 Hz) matched those of $S_{\chi_w}(n) / \sigma^2_{\chi_w}$ to avoid increases in $\overline{w'\chi'_w}$ based on offsets rather than real flux losses. Since $S_{\chi_w}(n) / \sigma^2_{\chi_w}$ tended to rise at a particular frequency, $T_e(n)$ was limited to frequencies less than this. The resulting $T_e(n)$ for the three case studies are shown as thin lines smoothed using zero-phase forward and reverse digital filtering (The MathWorks, 1996) in Fig. 4.6. Application of Equation (4.3) with the modified $T_e$ resulted in corrections of 1.6% for ideal conditions, 3.9% for light rain, and 18.4% for heavy rain conditions (see Table 4.1 for conditions). These were associated with flux losses of 1.5%, 3.8%, and 15.5%, respectively. This flux loss for heavy rain conditions was smaller than the loss found using $wT$ cospectra and Equation (4.1), while losses were similar for ideal and light rain conditions.

The empirical transfer functions were also determined using $S_{w\chi_w}(n)$ and $S_{wT}(n)$ normalized by their covariances in Equation (4.2). The resulting $T_e(n)$ for the three case studies are shown as thick lines in Fig. 4.6. Corrections were slightly smaller at 1.8% for ideal conditions, 2.0%

for light rain, and 11.1% for heavy rain conditions. These were associated with flux losses of 1.8%, 2.0%, and 10.0%, respectively.

Differences in the results from the methods of Equation (4.1) and Equation (4.3) using the cospectra of $wT$ to correct $\overline{w'\chi'_w}$ were likely attributable to the influence of the proportion of the total flux from the low frequency range. Fig. 4.5 illustrates how negative contributions to the total covariance in the low frequency range were not identical for the $wT$ and $w\chi_w$ cospectra during the same periods. The assumption in Equation (4.1), that low frequency contributions to the total flux are equal for both $\lambda E$ and $H$, appears imperfect. In the heavy rain situation, $b$ of Equation (4.1) would be inflated as there were more low frequency contributions to $\overline{w'T'}$ than $\overline{w'\chi'_w}$ resulting in a larger correction. However, the 38% flux loss determined using Equation (4.1) was used throughout these analyses as the maximum likely loss of flux for $\lambda E$ measured during high humidity conditions.

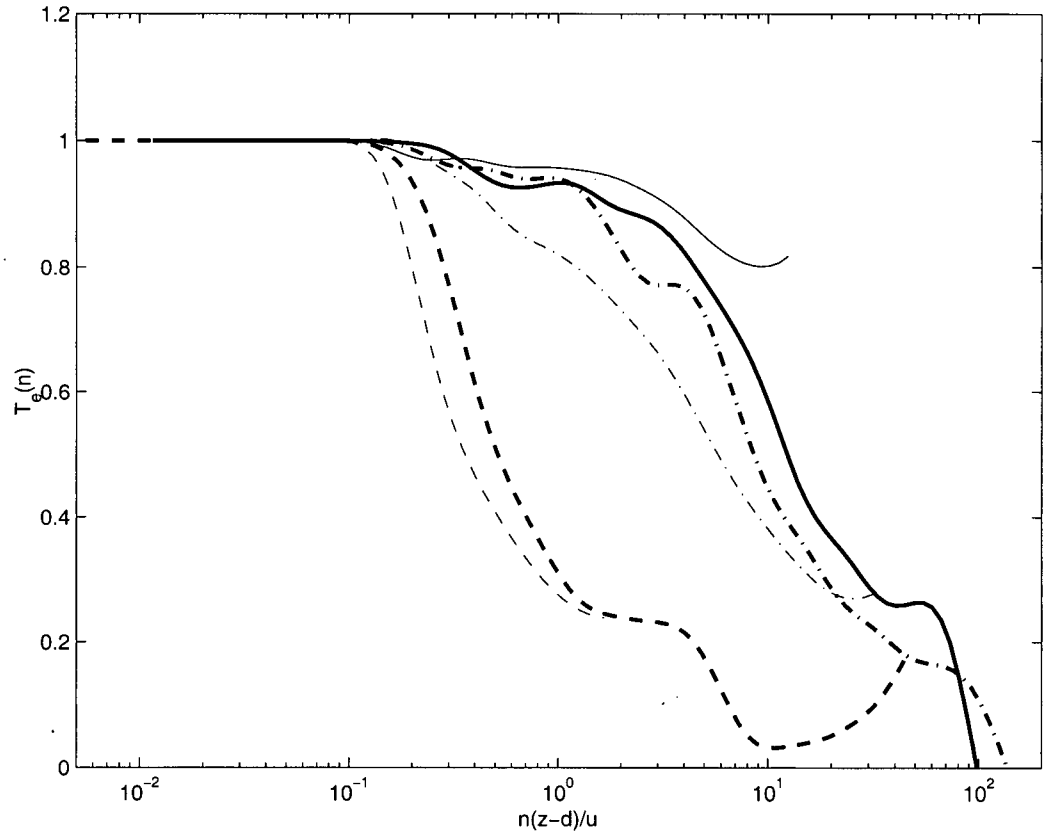


Fig. 4.6 Empirical transfer functions for latent heat flux loss due to signal attenuation determined during daytime conditions experiencing zero rainfall (solid lines), light rainfall (dash-dotted lines) and heavy rainfall (dashed lines)(Table 4.1). Thick lines designate $T_e(n) = \left( \frac{S_{w\chi_w}(n) / \overline{w'\chi'_w}}{S_{wT}(n) / \overline{w'T'}} \right)^{1/2}$, while thin lines designate $T_e(n) = \left( \frac{S_{\chi_w}(n) / \sigma^2_{\chi_w}}{S_T(n) / \sigma^2_T} \right)^{1/2}$. The latter do not extend beyond the frequency associated with increasing $\chi_w$ power spectral slope (Fig. 4.1). All $T_e(n)$ were smoothed using zero-phase forward and reverse digital filtering (The MathWorks, 1996).

#### 4.1.1.4 Delay Times

Calculated delay times deviating from the normal 20 to 23 samples at a 20 Hz sampling rate (equivalent to 1 s) were an indication that signal attenuation and high frequency loss of $\lambda E$ was occurring in high humidity conditions. Delay times were calculated online as the delay in $T$ required to maximize the cross correlation of $\chi_w$ and $T$ using the first 3 to 4 min of samples within each half hour. Delay times tended to deviate from normal values when covariances were very small, when pump problems resulted in decreased flow rates, when there were increases in the resistance in the lines (e.g. longer tube lengths, additional filters, dirty filters) and when RH increased. The latter case was likely a result of delayed measurements of instantaneous $\chi_w$ due to water vapour adsorption/desorption effects on the sampling tube walls (Laubach and Teichmann, 1996). Fig. 4.7 illustrates the apparent systematic underestimation of $\lambda E$ as delay times deviate from the normal value of 20 to 23 samples.

Since delay times were calculated using only a portion of the half hour, delay times for selected periods with proper sampling tube flow rates were recalculated using 25 min of the half hour. Under ideal conditions, delay times calculated over 25 min tended to approach normal values with less variability, as indicated by smaller standard deviations. During the afternoon of June 8, 1998 daytime weather conditions were dry and clear, with strong atmospheric turbulence and fluxes of large magnitudes (see Table 4.1). During this period, mean delay time ± 1 s.d. for $\chi_w$ and $\chi_c$ changed from 18.8 ± 41.2 and 30.4 ± 46.4 samples for 3 min to 24.3 ± 0.9 and 24.9 ± 7.3 samples for 25 min, respectively for 16 half hour measurements. However, delay times deviated further from normal, as indicated by the unreasonable means and larger standard deviations when measurements were recorded during conditions of high humidity despite good turbulence and large fluxes (see July 14, 1998 data in Table 4.1). Mean delay time ± 1 s.d. for $\chi_w$ and $\chi_c$ changed from 24.3 ± 55.4 samples and 4.1 ± 35.1 samples for 3 min to 55.2 ± 56.1 and 2.2 ± 48.8 samples for 25 min, respectively for 19 half hour measurements. Thus, 3 minute calculations gave a good indication of the actual delay time. As a result, delay times which deviated from normal values appeared to indicate possible signal attenuation problems when other influences were not present.

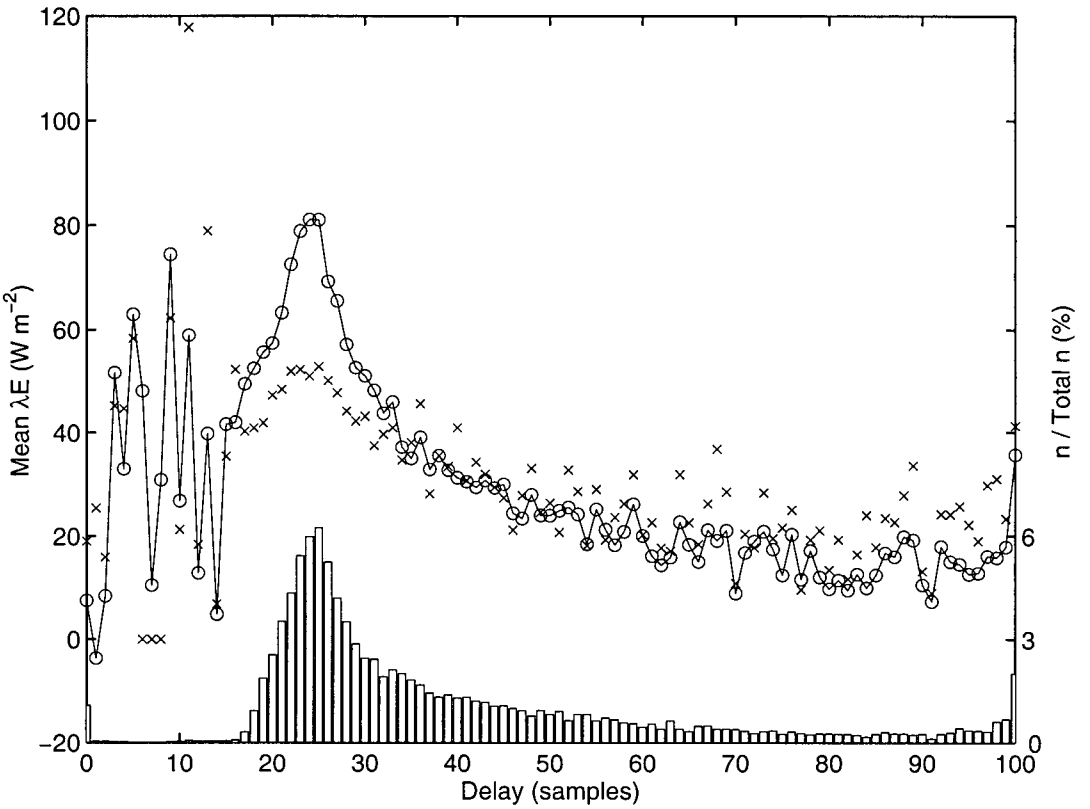


Fig. 4.7 The relationship between $\lambda E$ and delay times calculated as the time (# of samples) required to maximize the cross correlation between $\chi_w$ and $T$ when flow rates were > 8 L min$^{-1}$ and atmospheric turbulence was strong ($u_* > 0.2$ m s$^{-1}$). Mean $\lambda E$ for each delay time (O) is shown with the magnitude of 1 s.d. (×) and the proportion of measurements which occur in each delay time bin (vertical bars). Total n is 12251 half hours.

In general, this analysis indicated that significant underestimation of $\lambda E$ was likely while $H$ could be measured adequately under rainfall and high humidity conditions. An additional factor not fully addressed was the effect of contaminants such as dust and pollen within the sampling tube and filters. This situation has been suggested to result in significant underestimation of $\lambda E$ also likely due to adsorption/desorption of water vapour molecules (Judd, 1995; Smith and Campbell, 1999). With dirty tubing and filters, the effects of high humidity will only be increased and may account for the persistence of high frequency losses despite heating of the

sampling tube. As a result, the various means of correcting $\lambda E$ discussed above may be undertaken when deviations of measured delay times indicate a need.

### 4.1.2 Monin-Obukhov Similarity

Following Foken and Wichura (1996), the non-dimensional standard deviations of $w$ ($\phi_w = \sigma_w / u_*$) and $T$ ($\phi_T = \sigma_T / T_*$) were calculated and compared to values derived for this site using the Businger-Dyer formulations to investigate sonic anemometer performance during inclement weather. Monin-Obukhov similarity theory predicts values of $\phi_w$ and $\phi_T$ to become universal functions of $\zeta$ with fully developed turbulence structure within the surface layer when $-2 \leq \zeta \leq 1$, where the similarity functions are valid (Kaimal and Finnigan, 1994). The Businger-Dyer forms of $\phi_w$ and $\phi_T$ for the unstable range $-2 \leq \zeta \leq 0$ are,

$$\phi_w = a\left(1+3\left|(z-d)/L\right|\right)^b \tag{4.4}$$

$$\phi_T = a\left(1+9.5\left|(z-d)/L\right|\right)^b \tag{4.5}$$

where $u_*$ is the friction velocity, $T_*$ is the surface layer temperature scaling variable, and $a$ and $b$ are empirical coefficients commonly found to be 1.25 and 1/3, respectively, for $\phi_w$ and 2 and -1/3, respectively, for $\phi_T$ (Kaimal and Finnigan, 1994). For the stable range, $0 \leq \zeta \leq 1$, the forms of $\phi_w$ and $\phi_T$ are,

$$\phi_w = a\left(1+0.2(z-d)/L\right)^b \tag{4.6}$$

$$\phi_T = a\left(1+0.5(z-d)/L\right)^b \tag{4.7}$$

where $a$ and $b$ are empirical coefficients commonly found to be 1.25 and 1, respectively, for $\phi_w$ and 2 and -1, respectively, for $\phi_T$ (Kaimal and Finnigan, 1994). Foken and Wichura (1996), suggested that deviations from these functions by more than 20 to 30% indicate poor data quality. Measured values of $\phi_w$ and $\phi_T$ will be increased with additional mechanical turbulence caused by obstacles (heterogeneous terrain) or by the sonic itself or due to heterogeneity in the surface temperature and moisture conditions (Foken and Wichura, 1996).

Fig. 4.8 illustrates how $\sigma_w/u_*$ varied with stability and rainfall intensity. The coefficients $a$ and $b$ in Equation (4.4) were determined applying an optimization procedure to measurements

recorded during rain-free, unstable and stable ($-2 \leq \zeta \leq 1$) conditions during the period between October 15, 1997 and May 31, 1999. This resulted in $a = 1.25$ and $b = 0.22$ ($n = 15593$, $R^2 = 0.20$). The coefficients were also determined using means of $\sigma_w/u_*$ binned into 12 $\zeta$ intervals with a width of 0.25 where $a = 1.21$ and $b = 0.24$ ($n = 12$, $R^2 = 0.98$). No improvements in fit were found using Equation (4.6) for the stable range. Fitted $a$ in Equation (4.4) agreed very well with the accepted literature value of 1.25, while $b$ was lower than the commonly observed 0.33 (Kaimal and Finnigan, 1994). A lower $b$ value was also found for a mature aspen forest (Blanken et al., 1998), where it was suggested that this may indicate an increased momentum transport resulting from the rough canopy surface.

In the near-neutral range, $|\zeta| < 0.02$, where 16% of rainfall measurements are recorded, mean $\sigma_w/u_*$ was $1.19 \pm 0.01$, n = 604 for rain periods and $1.25 \pm 0.01$ for dry periods, n = 1096. When investigating the relationship using linear regression, the values became 1.094, $R^2 = 0.98$ for rain periods and 1.097, $R^2 = 0.96$ for dry periods. After increasing the stability range to $|\zeta| < 0.1$, which included 52% of all rain events, means were found to be $1.22 \pm 0.003$, n =1956 for rain periods and $1.29 \pm 0.004$ for dry periods, n = 3780. Either stability range resulted in values which agreed well with the expected value of 1.25 (Kaimal and Finnigan, 1994) for dry conditions and only slightly lower values for rainy conditions indicating satisfactory measurements from the sonic anemometer under rainfall conditions. Using this criterion, Gash et al. (1999) also concluded that a Gill Solent Model A101R2 sonic anemometer performed well in rainfall as mean $\sigma_w/u_*$ was 1.19 and 1.18 for dry and rainy periods.

Fig. 4.8 shows that mean values of $\phi_w$ deviate from those measured in dry conditions in the unstable range. This was partly attributable to the rarity of an unstable atmosphere being maintained during rainfall such that means were not weighted similarly. Only 3.3% of the measurements made during rainfall were recorded when $\zeta < -0.38$. Overall, 90.6% of dry condition measurements fell within 30% of the $\phi_w$ calculated using Equation (4.4) while 93.7% to 98.0% were within this range during the various rainfall intensity ranges shown in Fig. 4.8. These percentages fell to 82.0% and 87.8% to 96.5%, respectively when the range was reduced to 20% of the $\phi_w$ calculated using Equation (4.4). As a result, rainfall did not result in any discernible negative effects on velocity components measured using the sonic anemometer.

The relationship between $\phi_T$ and $\zeta$ is considerably more problematic as $\phi_T$ increases with stability conditions approaching neutrality (see Equations (4.5) and (4.7)). Using Equation (4.7) with $a = 2$ and $b = -1$, as suggested by Kaimal and Finnigan (1994) for $0 \leq \zeta \leq 1$, 58.9% of the measurements in dry conditions (n = 15593) fell within 30% of the expected value of $\phi_T$ and 28.1% for rainy conditions (n = 3173). Better results for the unstable range, $-2 \leq \zeta \leq 0$ and rainfall conditions were obtained with Equation (4.5) and $a = 2$ and $b = -1/3$. 46.1% of dry period values and 50.4% of rainy period values were within 30% of the expected $\phi_T$. However, this indicated that about half of the sonic anemometer $T$ measurements were of poor quality in both dry and rainy conditions. These results indicated the difficulty in applying Monin-Obukhov similarity theory as a means to check the quality of scalar values such as $T$ under all conditions whether rainy or dry.

To obtain an estimate of $a$ in Equations (4.5) and (4.7), $\sigma_T$ was regressed against $T_*$ when $|\zeta| < 0.1$ (not shown). For dry periods, $a$ was 1.39 ($R^2 = 0.27$, n = 3783) and 1.02 for rainy periods ($R^2 = 0.16$, n = 1956). Both estimates were lower than the commonly used value of 2 while $a$ for rainfall conditions was lower than dry conditions and associated with more data scatter.

In general, rainfall appeared to have a greater negative effect on sonic anemometer measurements of $T$ than on the velocity components. This was expected as velocity components measured by the sonic anemometer were derived by differencing the transit times of the acoustic signal along the path in opposite directions. Temperature was derived from the addition of these transit times, thereby increasing the error. However, bearing in mind the satisfactory spectral and cospectral results, there does not seem to be significant anemometer performance problems during rainfall conditions.

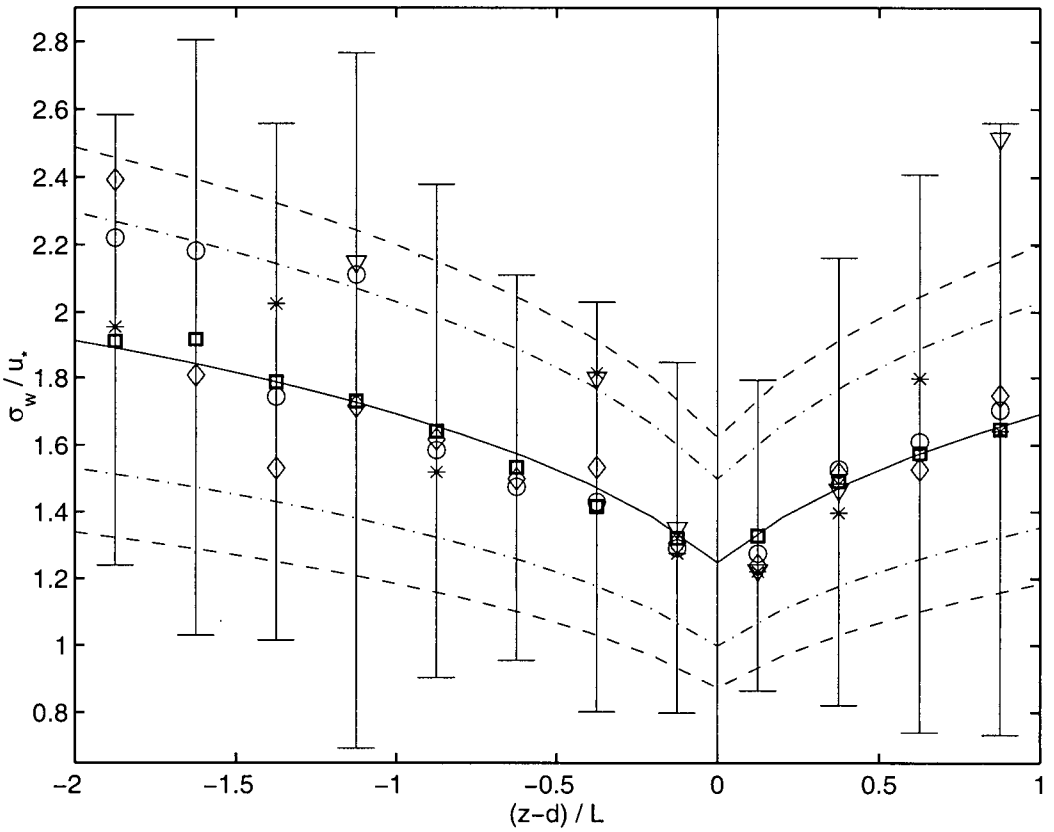


Fig. 4.8 Mean $\sigma_w/u_*$ ($\phi_w$) against stability, $\zeta$ = ($z$-$d$)/$L$. Symbols denote the following rates of precipitation, 0 mm/30 min (□), 0 - 0.6 mm/30 min (○), 0.6 - 1.6 mm/30 min (◊), 1.6 - 3.9 mm/30 min (✳) and > 3.9 mm/30 min (▽). Error bars indicate the 95% confidence interval for the mean of all measurements in each bin. The solid line indicates the dependence of $\sigma_w/u_*$ on stability as described using the Businger-Dyer relationships (Equation (4.4)) with $a$ = 1.25 and $b$ = 0.22 found for dry conditions. Dash-dotted lines and dashed lines indicate deviations by ± 20% and ± 30%, respectively.

## 4.2 FLUX FOOTPRINTS

To ensure that measured eddy fluxes originated from our 50-year-old Douglas-fir stand rather than from surrounding areas, flux source areas or footprints were determined (Table 4.2). In general, the distance to the peak flux source was no greater than 120 m upwind from the tower, while an area extending 950 to 1060 m from the tower was required to account for 80% of the flux source area. However these distances ranged from 385 m up to 3841 m depending on the degree of atmospheric turbulence. As indicated in Section 3.1, this site was particularly homogeneous with at least 400 m of fetch in all directions and about 700 to 800 m of fetch in the prevailing daytime NE wind direction (see Fig. 3.1). Beyond this was a very similar forest ranging in age from 24 to 57 years. These results implied that there was generally sufficient fetch to eliminate concerns over inhomogeneity and specifically, edge effects on the fluxes. However, the 5 to 10° slope and source areas greater than 2 km in the upslope direction did allow for advection caused by dynamical effects in the vicinity of the mountains of Vancouver Island (Bernhofer, 1992)

Table 4.2 Upwind footprint distances estimated to act as the peak flux source ($x_{max}$) and source area for 80% of the measured flux (Schuepp et al., 1990) for unstable ($-2 \leq \zeta < -0.02$), neutral ($-0.02 \leq \zeta \leq 0.02$) and stable ($0.02 \leq \zeta \leq 1$) conditions. Also listed are the $u/u_*$ ratios determined within these stability ranges using linear regression (unstable $R^2 = 0.85$, n = 7731, neutral $R^2 = 0.92$, n = 1702 and stable, $R^2 = 0.85$, n = 9339). Maximum and minimum flux source areas are also shown.

| | Unstable | | Neutral | | Stable | |
|---|---|---|---|---|---|---|
| | $x$ (m) | $u/u_*$ | $x$ (m) | $u/u_*$ | $x$ (m) | $u/u_*$ |
| Distance to peak flux source ($x_{max}$) | 107 | 4.1 | 117 | 4.5 | 118 | 4.5 |
| Distance to 80% of cumulative flux source area | 955 | 4.1 | 1051 | 4.5 | 1057 | 4.5 |
| Minimum distance to 80% of cumulative flux source area ($u/u_* > 0$) | 385 | 1.7 | 559 | 2.4 | 442 | 1.9 |
| Maximum distance to 80% of cumulative flux source area (for $u_* >$ 0.2 m $s^{-1}$) | 3841 | 16.5 | 2304 | 9.9 | 3333 | 14.3 |

## 4.3 ENERGY BUDGET CLOSURE

Energy budget closure is an important independent method used to ascertain the quality of the turbulent flux measurements (Moncrieff et al., 1996). The lack of closure achieved in many studies stems from a variety of proposed causes such as a failure to meet the theoretical requirements for eddy covariance, sensor errors, and meteorological problems (Foken and Wichura, 1996; Lee, 1998). As a result, the residual is often attributed to the sum of instrumental uncertainties, to the result of mismatched areas of representation (e.g. $R_n$ vs. eddy fluxes), and very often, to poorly measured storage terms (Fitzjarrald and Moore, 1994).

During the measurement period between October 15, 1997 and May 31, 1999, an average energy budget closure was calculated as the slope of the linear regression of half hourly turbulent flux measurements ($H + \lambda E$) on the available energy ($R_a$) forced through zero. Energy budget closure was 76.9% ($R^2 = 0.88$, n = 25891) over all half hour measurements (see Section 3.5.6 for flux screening process) and improved only slightly to 77.5% using only daytime values ($S\downarrow > 0$ W $m^{-2}$) ($R^2 = 0.87$, n = 13106) while it fell to 53.0% using only nighttime values ($R^2 = 0.10$, n = 14454). Daily energy closure was 78.9% ($R^2 = 0.85$, n = 587) or 89.3% when computed with an offset of -1.2 MJ $m^{-2}$ $day^{-1}$ ($R^2 = 0.89$, n = 587). Fractional energy closure using 24-h values also varied on a seasonal basis with improved closure occurring in the summer months (May to September) with median values ranging from 83% (May 1998) to 87% (August 1998), while very poor closure was possible in the winter months (October to April) from -49% (February 1999) to 77% (October 1997). Using all half hour measurements from May 1, 1998 to September 30, 1998, closure forced through zero was 82.2% ($R^2 = 0.92$, n = 7061) and 65.5% ($R^2 = 0.76$, n = 17376) for periods between October 15 and April 30 during 1997/98 and 1998/99.

All turbulent fluxes in this analysis were derived from $w$ and $T$ or $\chi_w$ means linearly detrended over the half hour. Using fluxes derived from block average means added approximately 2.5% to the energy closure estimates such that energy closure for all half hour measurements increased from 76.9% to 79.4%.

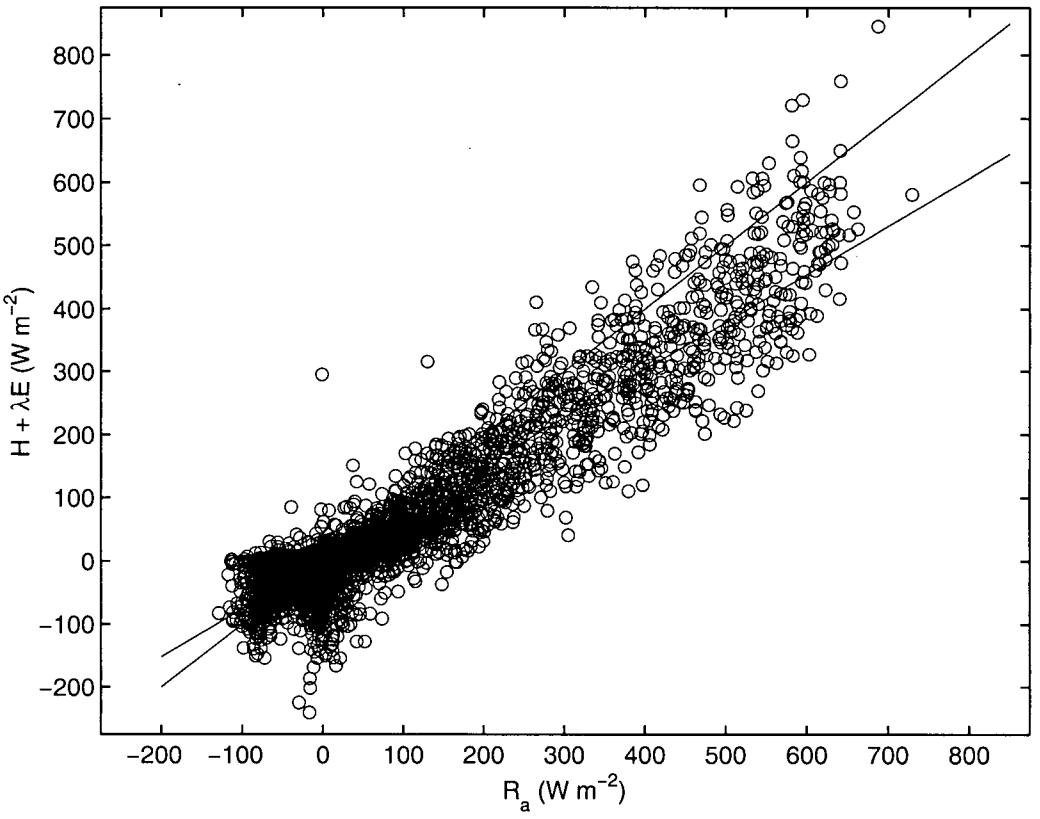


Fig. 4.9 Energy budget closure, the ratio of turbulent fluxes to available energy $(H + \lambda E)/R_a$, where $R_a = R_n - J - G$ for all half hour values subject to data screening (Section 3.5.6). Linear regression forced through zero results in a closure measure of 76.9% ($R^2 = 0.88$, n = 25891).

These overall fractional closure values were not significantly less than most values reported in the literature for eddy covariance measurements obtained above other forests. Using half hourly values and regression with an offset, Blanken et al. (1997) obtained closure of 87% for all values with 95% during the daytime and 53% during the night for a 22 m tall aspen forest. The same method resulted in closure of 83% for a shorter, more open canopied Douglas-fir forest, while total daytime values ranged from 67% to 96% during the summer measurement period (Lee and Black, 1993). Laubach et al. (1994) found daytime closure ranging from 70% to 93% with measurement height and month over a 31 m tall spruce forest. An open canopied ponderosa pine forest of 33-m height was found to have a 24-h closure of 70% over 426 days (Anthoni et al., 1999). Using daytime measurements only, 89% closure was found over a deciduous forest

(Barr et al., 1994), while 90% was found for a Ponderosa pine forest (Denmead and Bradley, 1985).

Known sources of error in the energy budget included the neglected photosynthesis term which would not likely have exceed 5 W $m^{-2}$ as found for a more productive aspen forest (Blanken et al., 1997). Despite the closed canopy, it could be assumed that soil heat flux, ($G$) experienced fairly large horizontal heterogeneity due to the patchy nature of the solar irradiance which penetrated the forest floor within the source location of the turbulent fluxes. Therefore, using only three soil heat flux plates may not have been adequate (Lee and Black, 1993). However, only about 3% of global solar radiation reached the forest floor such that $G$ tended to be very small with values rarely exceeding +40 W $m^{-2}$ or dropping below -13 W $m^{-2}$. In addition, differences between the sensors were minimal (mean differences ranged from 0.4 W $m^{-2}$ to 17 W $m^{-2}$). The assumption that $S_t$ may be represented using only two trees also may have been in error, as suggested in Section 3.5.4. The spatial characterization of $R_n$ using a single net radiometer would generally be considered acceptable within this very homogeneous, closed canopy (Anthoni et al., 1999). However, under calm atmospheric conditions, possible differences in albedo of the 50-year-old stand and surrounding younger stands may have influenced the matching of flux source areas with $R_n$ measured at the tower. Although the flux averaging time of 30 min was chosen to provide the most robust flux estimate (Lee and Black, 1993), turbulent fluxes may have been underestimated as low frequency contributions, with time scales exceeding 15 minutes, were not sampled adequately. Furthermore, the results of Section 4.1 suggested that $\lambda E$ may have been significantly underestimated during high humidity conditions. When the sampling pump flow was low, flow was not turbulent within the sampling tube and further signal attenuation would occur. However, using the correction procedure for signal attenuation outlined in Section 3.5.6 and selecting half hours with good pump flow, half hour closure only improved slightly to 79.9% ($R^2$ = 0.88, n = 24550). Ultimately, one of the main uncertainties in the estimation of available energy for fractional energy closure on time scales less than 24 h is quantifying the rate of energy storage.

### 4.3.1 Storage Terms

Accurately determining the storage terms in the energy budget may be a critical component for achieving closure and thus, confidence in the measurements.

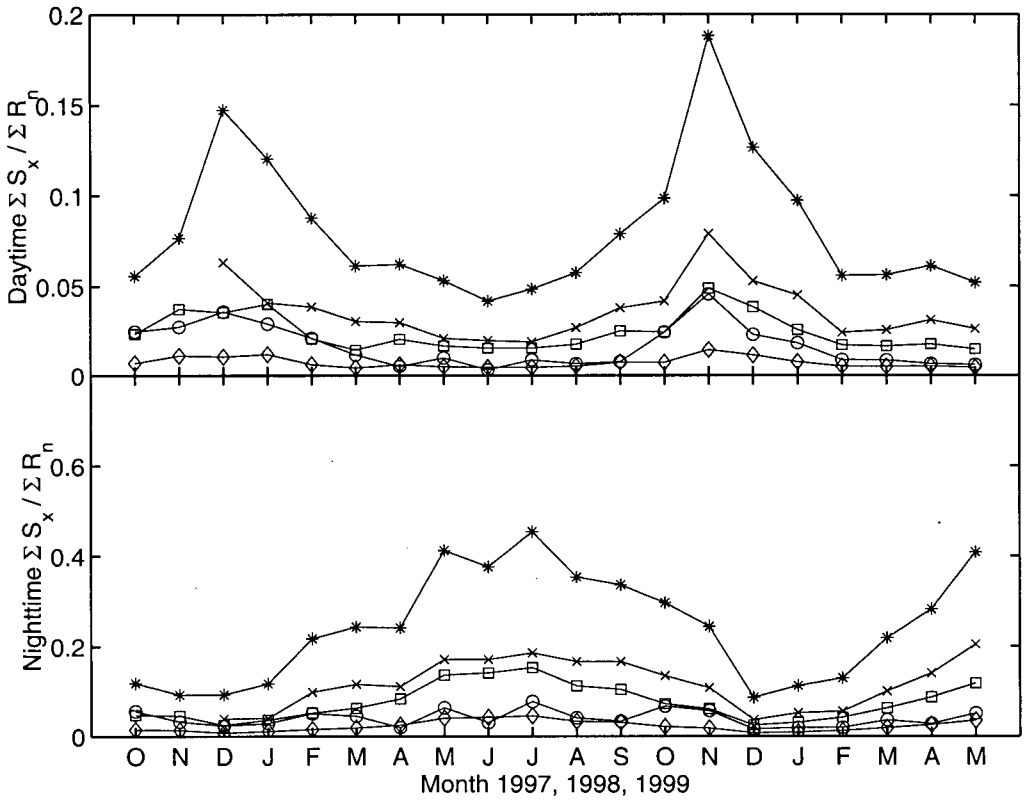


Fig. 4.10 The proportion of $R_n$ accounted for by the storage terms on a monthly basis during the daytime ($S\downarrow$ > 10 W m$^{-2}$) (top panel) and the nighttime ($S\downarrow$ = 0 W m$^{-2}$) (bottom panel). Values are calculated using the sum of the half hour measurements during each month. The storage terms illustrated are rates of total storage excluding photosynthesis, $J$ (✳), tree bole heat storage, $S_t$ (×), sensible heat storage in the air, $S_h$ (□), latent heat storage in the air, $S_l$ (○) and heat storage in the needles and branches, $S_{nb}$ (◊) .

Fig. 4.10 illustrates the importance of $J$ in the energy budget as a monthly ratio of $J$ to $R_n$ during both daytime and nighttime throughout the measurement period. Monthly mean $J \pm 1$ SE was found to be as high as 17.17 ± 1.24 W m$^{-2}$ during the daytime, as low as -23.83 ± 1.05 W m$^{-2}$ during the night with half hour values as high as +110 W m$^{-2}$ and as low as -200 W m$^{-2}$, while 93.7 % of the measurements fell within ± 50 W m$^{-2}$. In total, $J$ accounted for 6.21 % of daytime $R_n$ and 24.93 % of nighttime $R_n$ where daytime values were chosen when solar radiation was greater than 0 W m$^{-2}$. Total daytime $J$ was most important to closure during the winter months (November to February), while total nighttime $J$ was most important to closure during the

growing season months (approximately April to October). During the winter months, monthly mean daytime $R_n$ was 71.9 ± 3.7 W $m^{-2}$ while $J$ was still significant and positive (see Fig. 4.11). Conversely, during the growing season, daytime $R_n$ was much larger than $J$. However, $J$ was typically large and negative during summer nights (see Fig. 4.11) when monthly mean $R_n$ was about -50.6 ± 1.1 W $m^{-2}$. On an annual basis, as on a diurnal basis, cumulative $J$ was expected to go to zero. In 1998, the cumulative sum of $J$ was 0.18 MJ $m^{-2}$ (n = 17518) which amounted to 0.008% of the cumulative sum of $R_n$ in 1998 equal to 2205 MJ $m^{-2}$ (n = 17520). As this was a departure from zero, some remaining problems in the measurement and calculation of the $J$ term existed.

The total rate of energy storage in this densely planted forest made up a slightly larger fraction of $R_n$ than what has been found for other forests. Total storage accounted for only 2% to 8% of daytime $R_n$ during the growing season for a 22 m tall boreal aspen forest (Blanken et al., 1997) and 2.6 % in a mixed deciduous stand (Barr et al., 1994). During the summer at a shorter, less dense Douglas-fir stand, total daytime $J$ did not exceed 5% of $R_n$ (Lee and Black, 1993). More similar values have been obtained for a 31 m tall spruce forest where $J + G$ was as much as 60 to 90 $Wm^{-2}$ depending on the month (Laubach et al., 1994). The Thetford forest of 15.8 m tall Scots and Corsican pine at 800 stems $ha^{-1}$ was also similar with maximum $J$ around +70 W $m^{-2}$ and a minimum of -50 W $m^{-2}$.

The diurnal variations of $S_t$, $S_h$, $S_l$, and $S_{nb}$ which make up $J$ are shown in Fig. 4.11. The relative proportions of the individual storage terms making up $J$ did not show any discernible seasonal variations. The means of the monthly ratios are listed in Table 4.3 and show $S_t$ making up the largest proportion of $J$ at 45% with $S_h$ second at 31% , followed by $S_l$ at 19% and $S_{nb}$ with the least contribution at 9%.

Table 4.3 The mean ratios of the individual storage terms $S_t$, $S_h$, $S_l$, and $S_{nb}$ to $J$, the total storage term where $J = S_t + S_h + S_l + S_{nb}$. Ratios on the first line were calculated first as monthly ratios where the totals during the daytime and nighttime for each month were found and then averaged over the 18 months between December 1997 and May 1999. The second ratios were calculated from the totals during this period.

| Mean ± 1 SE<br>$\sum S_x / \sum J$ | $S_t/J$ | $S_h/J$ | $S_l/J$ | $S_{nb}/J$ |
|---|---|---|---|---|
| Daytime | 0.448 ± 0.011 | 0.311 ± 0.014 | 0.195 ± 0.021 | 0.093 ± 0.004 |
| | 0.443 | 0.310 | 0.157 | 0.093 |
| Nighttime | 0.449 ± 0.009 | 0.314 ± 0.014 | 0.191 ± 0.021 | 0.094 ± 0.004 |
| | 0.441 | 0.314 | 0.155 | 0.094 |

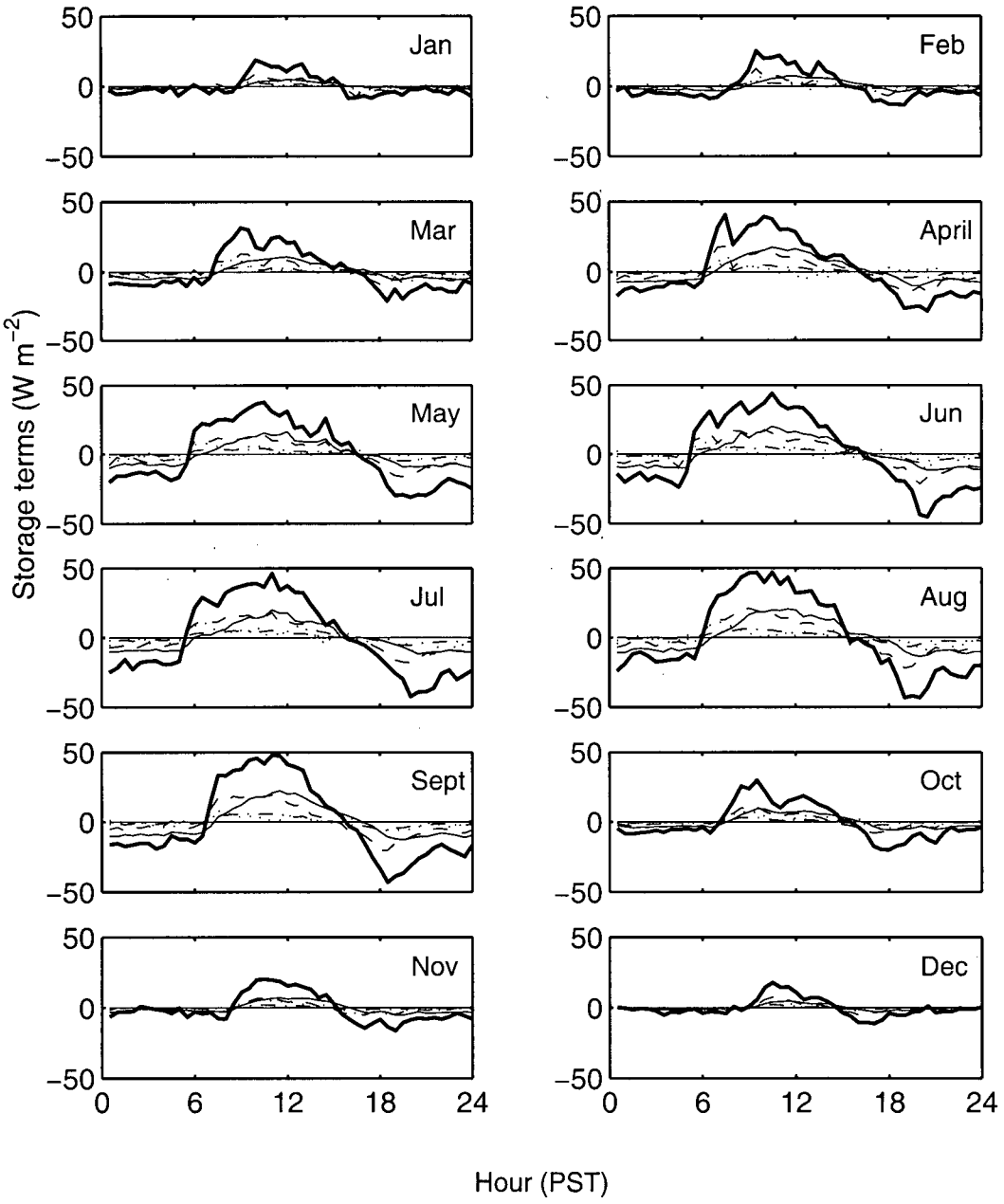


Fig. 4.11 Diurnal variations of storage terms calculated as a ensemble average of each half hour within each month of 1998. Shown are total storage, $J$ (thick solid line), tree bole heat storage (thin solid line), sensible heat storage in the air (dashed line), latent heat storage in the air (dotted line) and heat storage in the needles and branches (dash-dotted line).

Heat storage in the vegetation was clearly the most significant storage term and may be estimated a number of different ways. Stewart and Thom (1973) approximated the thermal behaviour of trees to a layer of water of a certain depth responding to the changes in air temperature. With $S_l$ and $S_h$ known, $S_t + S_{nb}$ was found as the difference from hourly data (taken during the evening) when the aerodynamic fluxes were negligible compared to $R_n$. This method depends upon the assumption that closure has been achieved and that the entire residual term can be attributed to storage and not to instrument errors. Another method to calculate $S_t$ involves modeling the heat flux density at the bole surface using a sinusoidal bole surface temperature (Herrington, 1969)(see Appendix D). This method has further been developed with the addition of a surface resistance and expressions for trees of variable radii (Moore and Fisch, 1986) (Meesters and Vugts, 1996). However, this method requires trees of large diameter to avoid overestimating $S_t$ (Appendix D). Alternatively, as done here, $S_t$ can be calculated directly using measured values of tree bole temperature within a number of tree bole annuli of similar thermal characteristics and then integrated along the entire bole length (Aston, 1985; Blanken et al., 1997). Empirical relationships may then be developed between $S_t$ and above-canopy air temperature (Aston, 1985; McCaughey and Saxton, 1988).

Maximum values of $S_t$ at this site were about ±45 W $m^{-2}$ with 90% of the values within ±30 W $m^{-2}$. Over the measurement period, $S_t$ accounted for 4.2% of $R_n$ ($R^2$ = 0.57, n = 26005) ranging from 1.9% to 7.7% with daytime $S_t$ summed over a month. These were only slightly smaller than the ±55 W $m^{-2}$ found by Stewart and Thom (1973) in a 15.8-m tall pine forest. Denmead and Bradley (1985) found that $S_t$ in the morning could amount to as much as 17% of the $R_n$ (~ 100 W $m^{-2}$) in a 16-m tall pine forest using Herrington's basic model. However, these may be inflated as the tree diameters were slightly too small and they did not account for bole taper. Aston (1985) found that in a 10-m high eucalyptus forest, heat storage was approximately 10% of $R_n$ during a clear sunny morning (~ 20 - 60 W $m^{-2}$). Our values were similar to those of a 35-m tall Amazon forest where $S_t$ accounted for 3% to 5% of daily $R_n$ and on overcast days $S_t$ could exceed 6% and occasionally 10% of $R_n$ (Moore and Fisch, 1986). $S_t$ from our forest tended to be larger than values obtained from a 20-m tall mixed deciduous and coniferous stand where the daytime mean ranged from -2.5% to 3.0% of $R_n$ (McCaughey and Saxton, 1988).

Discrepancies between forests of similar tree biomass and similarities between forests of unequal tree biomass are not surprising considering the variety of ways with which it may be

calculated. Appendix D illustrates Herrington's method applied to our forest and the resultant decrease in $S_t$ when tree taper was accounted for.

These calculations of $S_t$ for our Douglas-fir forest indicated that rates of heat storage within the stand biomass in addition to $S_h$, $S_l$ and $S_{nb}$ were a significant proportion of the energy balance particularly during winter months when energy budget closure tended to be the weakest. Despite the high degree of uncertainty in the estimation of $J$ for this forest, estimated values were already large compared to other forests such that the 23% closure discrepancy (equivalent to a maximum of 138 W $m^{-2}$ when $R_a$ was 600 $Wm^{-2}$ ) was not likely attributable to storage terms. As a result other factors such as those related to the theoretical requirements for eddy covariance or sensor errors may be responsible for the lack of fractional energy closure (Foken and Wichura, 1996).

### 4.3.2 Wind Direction and Turbulence

Energy budget closure appeared to be clearly related to wind direction (Fig. 4.12) with poor closure tending to coincide with winds from the SE and SW quadrants (about 126° to 290°). Wind directions were found to be strongly bimodal (Fig. 4.12, bottom panel) at this site due to the land-sea/upslope-downslope circulations during the summer, spring and fall months. During the winter months, the predominance of passing cyclonic disturbances from the west resulted in winds predominantly from the ESE and SSW. Poor closure was associated with nighttime katabatic or downslope winds principally from the SW quadrant and into the SE quadrant reflecting the predominant winter wind directions (Fig. 4.13). Anabatic winds associated with the daytime were generally from the NE to ESE directions (about 0° to 130°) where closure values tended to be the greatest. These directions were also related to friction velocity and stability as nighttime winds from the SW - SE quadrants were associated with lower wind speeds, stable conditions, and lower friction velocities (Fig. 4.13). It seemed likely that closure was more closely related to atmospheric turbulence rather than wind direction and fetch as the study site was composed of a very homogeneous, even aged stand extending with adequate fetch in most directions. However, winds which originated from beyond a plateau followed by a marsh area lying approximately 1.5 km WSW of the tower (Fig. 3.1) may have shown evidence of the possible effects of changing surface type.

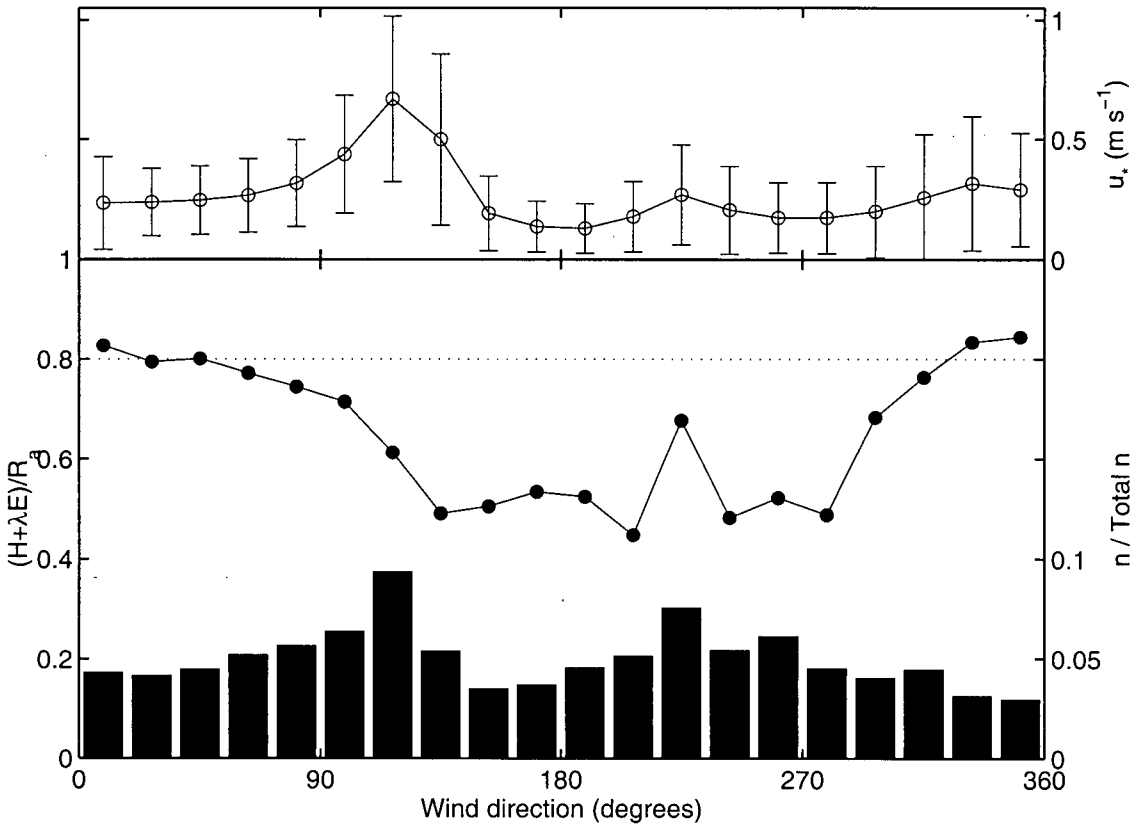


Fig. 4.12 Energy budget closure and mean friction velocity ($u_*$) versus wind direction for half hour measurements between October 15, 1997 and May 31, 1999. Energy budget closure is the slope of the linear regression of $H + \lambda E$ against $R_a$ forced through zero within each 18° wind direction sector. The dotted horizontal line indicates closure error of -20%. Vertical bars indicate the proportion of total half hour measurements which occur within each wind direction sector. The top panel shows mean $u_* \pm 1$ s.d. for each wind direction sector.

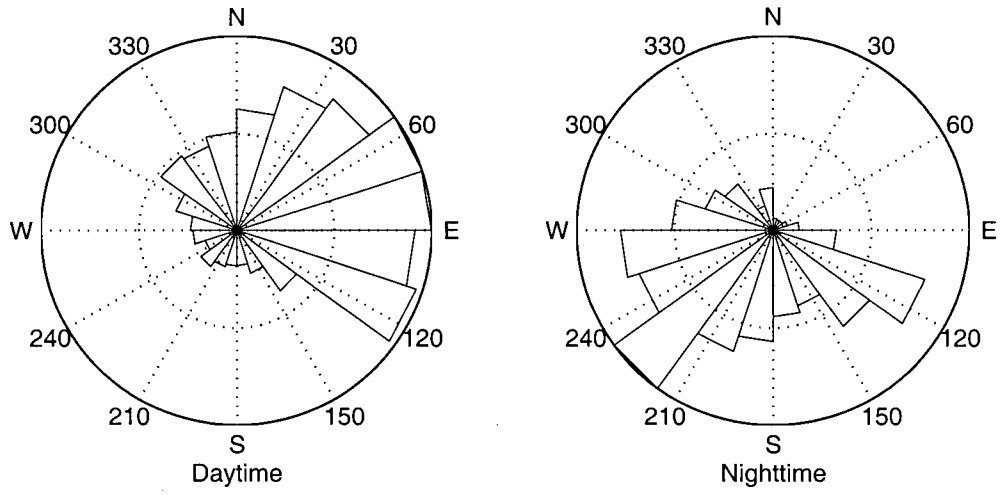


Fig. 4.13 Wind rose using the R. M. Young wind monitor measurements recorded during the daytime ($S\downarrow > 5$ W m$^{-2}$) and nighttime ($S\downarrow = 0$ W m$^{-2}$). Outer and middle radial circles indicate 10% and 5% of the total daytime and 12% and 6% of the total nighttime half hour observations, respectively.

Many studies using eddy covariance find a tendency for systematic underestimation of fluxes under calm conditions with neither mechanical nor convective turbulence, generally during the nights with low wind speeds (Anthoni et al., 1999; Blanken et al., 1997; Laubach et al., 1994; Lee, 1998; Yang, 1998). During calm periods, water evaporating from the soil surface and from the canopy may go into storage and subsequently be released with increasing turbulent conditions as a measurable flux above the canopy (and associated loss in storage). Otherwise, evaporated water may be carried away by drainage flows (Lee, 1998). In the absence of poor measurements due to instrumentation and processing problems such as tube attenuation (Moncrieff et al., 1996), the former situation is accounted for in measurable storage terms. However, the latter situation may result in horizontal flow convergence/divergence, and thus requires an unknown advective term which was not included in the energy budget. Flow

convergence/divergence requires that the air carried away is not replaced by similar air from upslope nor is recirculated back. Lee (1998) suggests this situation is characterized by a non-zero mean vertical velocity and may be included within a "mass-flow" term. Possible mechanisms include descending motions from stationary convective cells, synoptic scale subsidence or local circulations such as katabatic flow on undulating terrain (Lee, 1998). As this site was situated on terrain with a 5 to 10° slope, nighttime downslope winds may have been involved in flux divergence situations.

Evidence that good energy closure was closely related to well developed atmospheric turbulence associated with high $u_*$ and unstable conditions is shown in Fig. 4.14. Fractional energy closure improved with increasing $u_*$, attaining 80% closure when $u_*$ exceeded 0.35 m $s^{-1}$. This has also been found by a number of recent studies using the eddy covariance technique (Anthoni et al., 1999; Barr et al., 1994; Blanken et al., 1997). By selecting half hour measurements with recorded $u_*$ values > 0.35 m $s^{-1}$, closure of 82.1% was achieved ($R^2$ = 0.88, n = 8764). It would appear that either the mechanical or convective production of turbulent energy will increase the likelihood of measuring significant $\lambda E$ and $H$ at the measurement height above the canopy. In addition, the flux source area (footprint) is smaller under these conditions such that less scale mismatch with the $R_n$, $J$, and $G$ terms may occur.

During the night, $u$ and $u_*$ tend to be low such that weak atmospheric turbulence leads to systematic underestimation of turbulent fluxes (Blanken, 1997). This was epitomized by very poor energy budget closure during many nights throughout July and August 1998 when both $H$ and $\lambda E$ remained negligible while significant longwave radiation continued to be emitted from the canopy. This particular problem is not unusual and has been found by others using the eddy covariance technique (Blanken et al., 1997; Laubach et al., 1994).

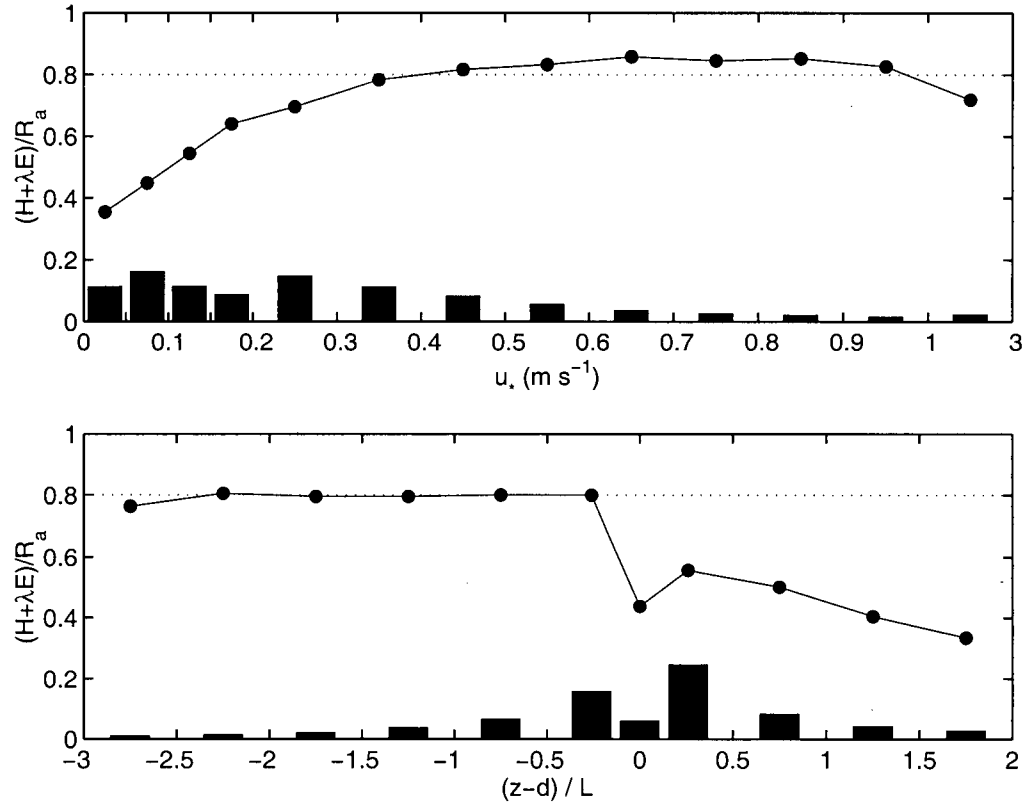


Fig. 4.14 Energy budget closure calculated as the slope of half hour ($H + \lambda E$) against $R_a$ forced through zero during similar $u_*$ periods (top panel) and stability ($\zeta = (z\text{-}d)/L$) periods (bottom panel). In the top panel, the last value is closure calculated when $u_* \geq 1$ m s$^{-1}$ with a maximum $u_* = 2.56$ m s$^{-1}$. The vertical bars indicate the proportion of total measurements at each $u_*$ and $\zeta$ range. The dotted horizontal line indicates a closure error of -20%.

## 4.4 SEASONAL PATTERNS & CONTROLS OF EVAPORATION

At the most basic level, evaporation rates from a forest depend on the availability of water, the availability of energy with which water may change state, the existence of a vapour concentration gradient, the existence of turbulent atmospheric conditions to transport the vapour away from the forest surface, and on the physiological control limiting water loss through the leaf stomata (Oke, 1987). This study investigated the relative importance of these various controls on evaporation rates throughout the measurement period on a seasonal and diurnal basis.

### 4.4.1 Weather Conditions (October 1997 - May 1999)

Fig. 4.15 shows daily mean weather and soil moisture variables monitored during the study period between October 15, 1997 and May 31, 1999. The general patterns of radiation, temperature and precipitation were characteristic of a northern temperate, maritime site experiencing mild, wet winters approximately through November to February and warm, dry summers extending from April to September, inclusively. Spring and fall transitions tended to occur during March and October, respectively. Mean 24-h temperatures rarely fell below freezing and could exceed values as high as 20°C. Mean daytime atmospheric saturation deficit closely followed the above canopy air temperature pattern with the highest values occurring in late July lagging behind peak incoming photosynthetic photon flux density ($Q$) around the summer solstice on June 21.

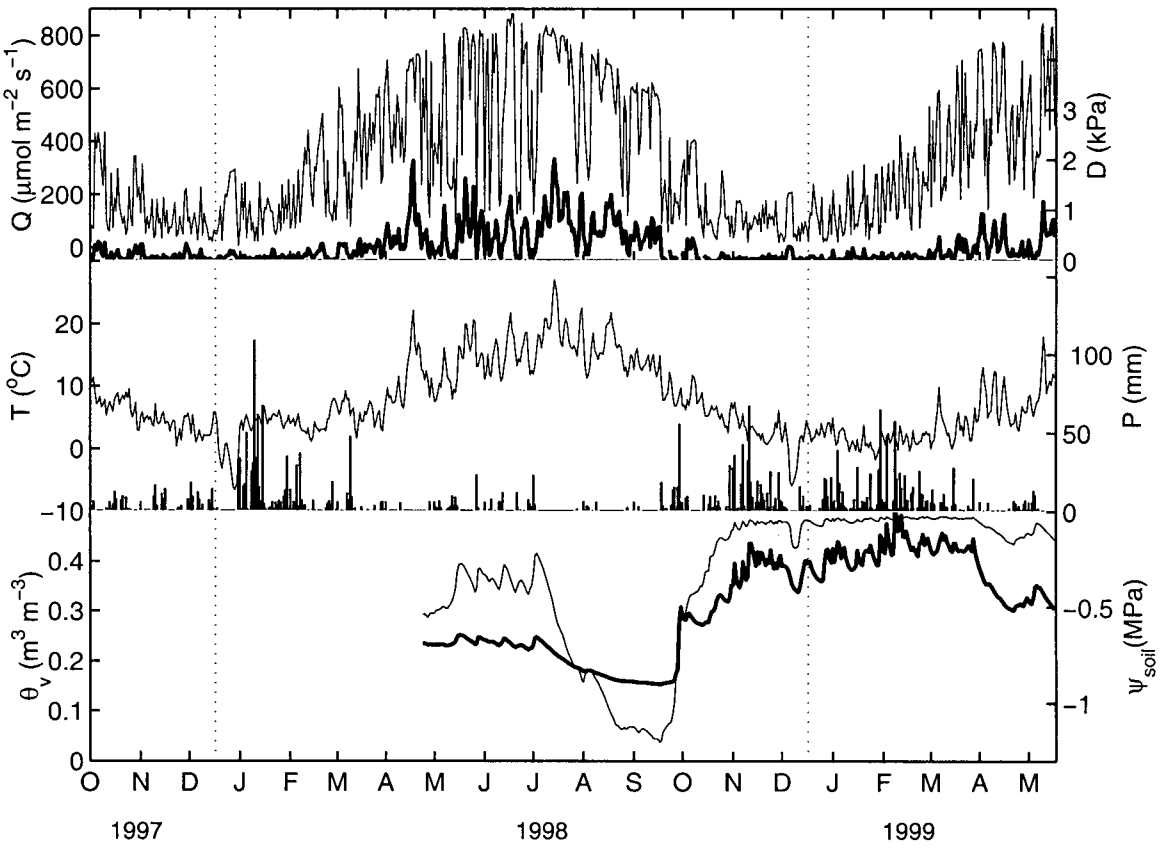


Fig. 4.15 24-h mean values of photosynthetic photon flux density ($Q$, thin line), daytime mean vapour pressure deficit ($D$, thick line), 24-h mean temperature ($T$, thin line), 24-h rainfall ($P$, bars), soil volumetric water content ($\theta_v$, thick line) and soil water potential ($\Psi_{soil}$, thin line). $\theta_v$ was calculated from half hour measurements using Water Content Reflectometers (Model CS615, Campbell Scientific Inc.) and 'corrected' up to average TDR values obtained bimonthly (see Section 3.3.1). $\Psi_{soil}$ was calculated using two water release curves for two soil layers applied to CS615 measurements only and integrated over 1 m depth of soil (Appendix B). As a result, $\theta_v$ and $\Psi_{soil}$ in this figure do not relate directly to the curve in Appendix B. Month tick marks are centered on the middle of the month (style is consistent throughout).

Weather conditions around the world were highly influenced by a significant El Niño event during 1997/98 and a rapid transition to strong La Niña conditions during 1998 (World Meteorological Organization, 1999). The equatorial Pacific sea surface temperatures associated with the 1997/98 El Niño reached near-record high temperatures (an anomaly of almost +3°C) at the beginning of 1998. Temperatures then fell rapidly in May and June, 1998 with average

central Pacific sea surface temperatures declining from values near 1°C above average to 1°C below average (World Meteorological Organization, 1999). Changes in global weather patterns result from interactions between the atmosphere and the ocean. On the Pacific coast of southern British Columbia, air temperatures in El Niño winters tend to be about 1°C to 1.5°C above normal, while total precipitation is fairly constant except with considerably less snow (Environment Canada, 1998). During La Niña winters, this area tends to experience colder winters by 1°C on average with near normal precipitation. However, snowfall may be as much as 90% above normal along the Pacific coast (Environment Canada, 1998).

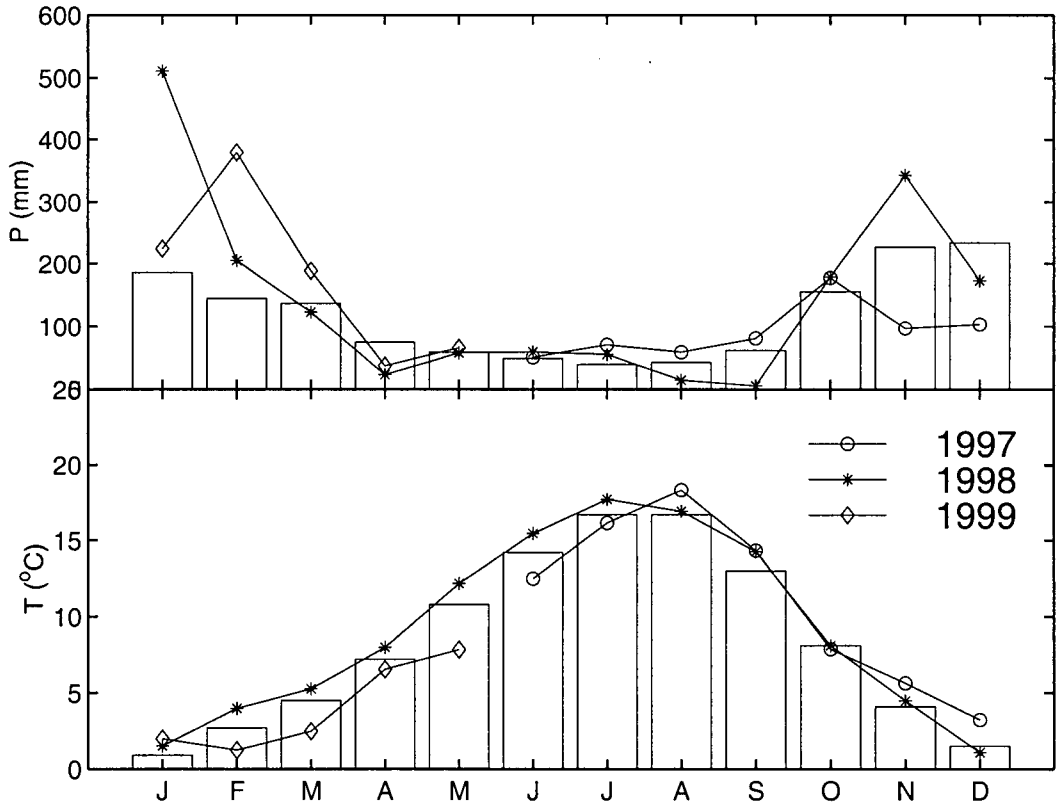


Fig. 4.16 Monthly values for total precipitation (top panel) and mean temperature (bottom panel) for 1997 (O), 1998 (✳), and 1999 (◊). Vertical bars indicate 30-year normals (1967-1997) from Campbell River Airport, Campbell River, BC.

Similar to the expected El Niño/La Niña climate, this site experienced a very mild, somewhat wetter than normal 1997/98 winter season followed by a warm, dry summer and a colder and

wetter than normal winter during 1998/99 (Fig. 4.16). Soil moisture clearly followed the rainfall pattern experiencing a steady dry-down during the summer of 1998 with the driest period in September 1998. The fall rains began in early October and brought the soil water content rapidly back up to saturation levels by November (Fig. 4.15). Snowfall during the winter of 1997/98 was minimal with sensors indicating a snow depth on the ground of at least 1 cm for only 4 days (2 days with 5 cm), while the 1998/99 winter experienced 88 days with at least 1 cm of snow (67 days with 5cm, 60 days with 10 cm, 53 days with 20 cm and 6 days with 50 cm of snow). The most striking feature of these seasonal weather patterns was the sharply contrasting rainfall patterns with high rainfall and a large number of rainfall days only in the winter. Winters at this site are dominated by passing low-pressure disturbances, while summers are characteristically warm and dry due to the strengthening subtropical high which moves northwards deflecting most Pacific cyclones north (Oke and Hay, 1994).

The proportion of time the canopy was wet or partly wet was established using a modeled canopy water balance with rainfall and evaporation as measured inputs and canopy parameters including the throughfall coefficient, $p$ and canopy saturation capacity, $S$ derived from throughfall measurements and validated using leaf wetness sensors (see Section 3.3.3; Appendix D) (Fig. 4.17). In total, the canopy was classified as being wet or partly wet for the equivalent of 251 days (12042 half hours) while it was dry for the equivalent of 312 days (14982 half hours) during the measurement period October 15, 1997 to May 31, 1999. Some half hours remained unclassified when $\lambda E$ was not calculated or measured. During the summer months (April to September, 1998), the canopy was wet less than 25% of the time. However, the canopy was wet between 30% to 45% of the time in April and May, 1999 marking the beginning of a cooler and somewhat wetter summer. The canopy was wet for almost 90% of November 1998, while normally, the canopy was wet from 50% to 75% of the time during the 1997/98 and 1998/99 winter months.

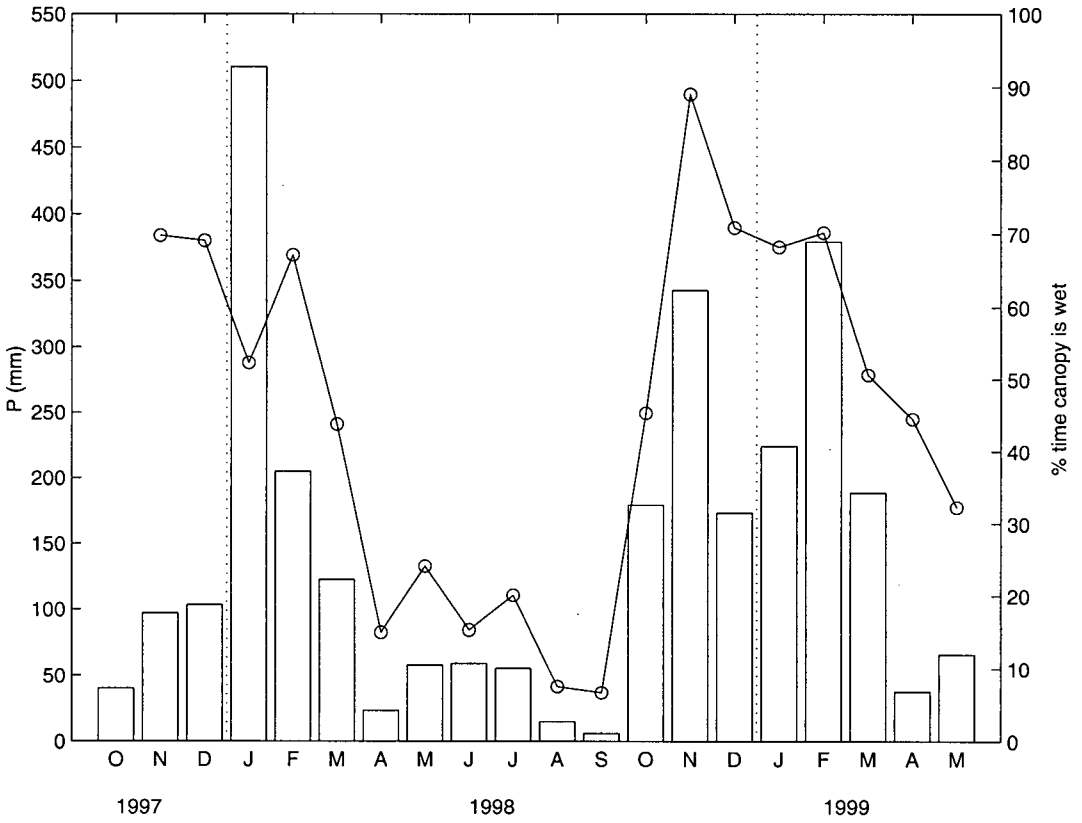


Fig. 4.17 Proportion of time during each month that the forest canopy was wet or partly wet (O). Vertical bars indicate the total amount of rainfall ($P$) received each month during the study. Wet canopy conditions were calculated using a canopy water balance model with $P$ measured directly and $E$ determined as the residual of the energy budget (see Section 3.3.3)

### 4.4.2 Energy Budget Components and Total Evaporation

Energy budget components for the entire measurement period are shown as daytime ($S\downarrow > 0$ W $m^{-2}$) and nighttime means for seven day periods in Fig. 4.18. Daytime $R_n$ remained positive throughout the year closely following the pattern of incoming radiation (i.e. $Q$ or $S\downarrow$) (Fig. 4.15). Nighttime values were consistently negative with slightly less negative values during the winter months. This was consistent with the typically overcast skies associated with the cyclonic disturbances which dominate the winter weather patterns at this site.

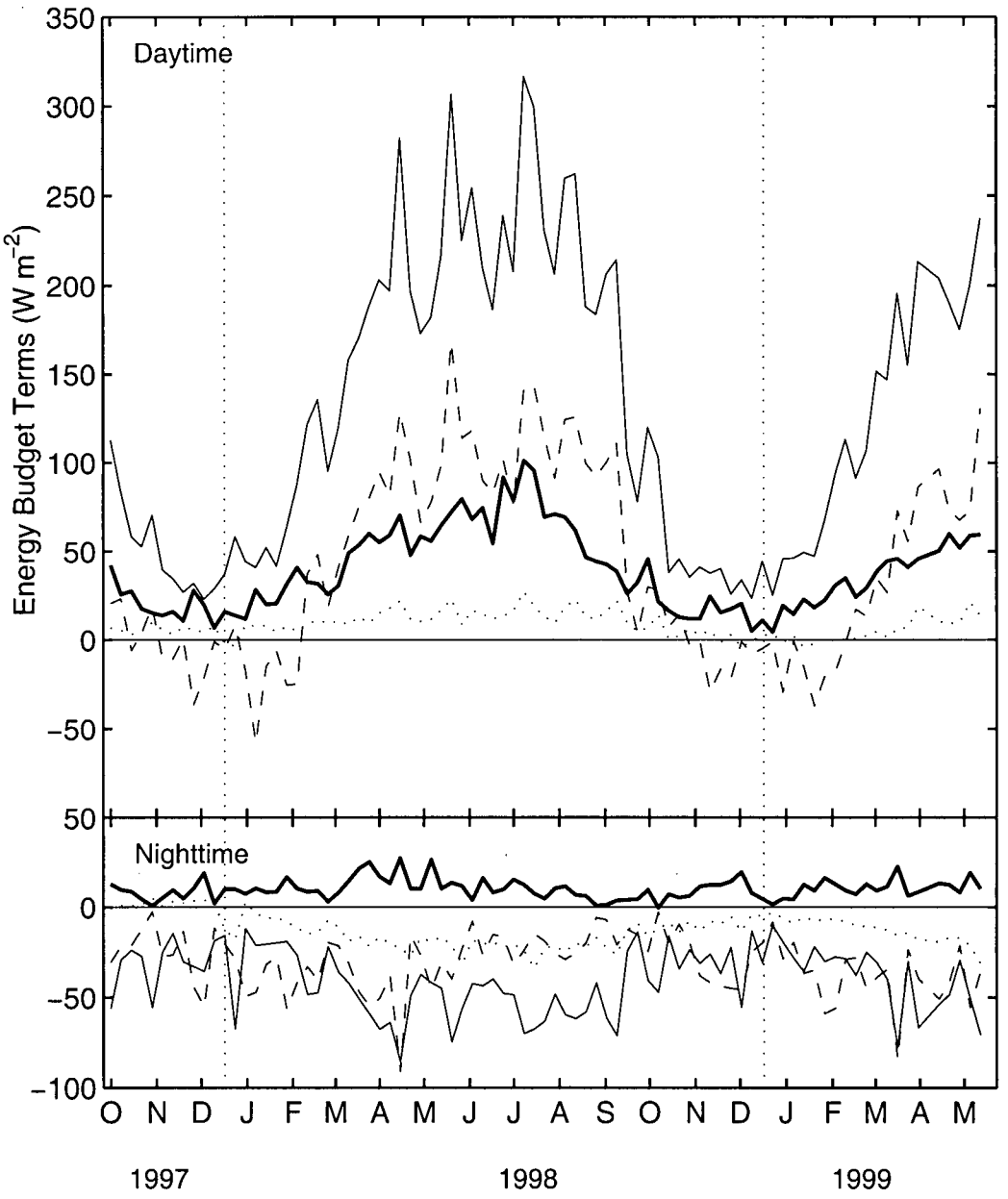


Fig. 4.18 Seven-day means of the energy budget components during the daytime when $S\downarrow > 0$ W m$^{-2}$ (top panel) and during the night (bottom panel). Illustrated are net radiation, $R_n$ (thin solid line), latent heat flux, $\lambda E$ (thick solid line), sensible heat flux, $H$ (dashed line) and soil heat flux with heat storage in the biomass and air column, $G + J$ (dotted line) between October 15, 1997 and May 31, 1999. No corrections were applied to $H$ or $\lambda E$ .

Soil heat flux, $G$, and heat storage, $J$, terms followed similar patterns with the expected slight temporal lag as a result of gradual warming and cooling of the soil. During the daytime, convective energy exchange from this forest underwent a rapid transition from a system dominated by positive $H$ during the summer (when mean $R_n$ was > 175 W $m^{-2}$) to an $\lambda E$ dominated one during the winter. In addition, the high rates of $\lambda E$ during the winter were supported by both radiative inputs (positive $R_n$) and downward $H$.

As discussed in Section 4.1, it was likely that $\lambda E$ was prone to underestimation during these typically very humid winter conditions between November and February. The resultant increase in mean daytime winter $\lambda E$, following the signal attenuation correction procedure in Section 3.5.6, was from 21 ± 24 W $m^{-2}$ without to 33 ± 38 W $m^{-2}$ with corrections (n = 2119) for 1997/98 and from 19 ± 24 W $m^{-2}$ without to 27 ± 25 W $m^{-2}$ with corrections (n = 1996) for 1998/99. Daytime $\lambda E$ corrected or uncorrected did not exceed $R_n$ when totaled over the winter periods. However, on a daily basis, mean daytime $\lambda E$ approached $R_n$ throughout the winter and occasionally exceeded it.

During the night, $\lambda E$ values indicated continued evaporation throughout the year supported by downward $H$ (Fig. 4.18). Mean $\lambda E$ during the night for both winter seasons was 13 ± 23 W $m^{-2}$, only slightly less than average daytime values during the winter months.

Overall, daytime mean $\lambda E$ patterns (Fig. 4.18) tended to follow daytime $D$ with peak values occurring in late July to early August 1998 (Fig. 4.15). The highest mean temperature values which caused the largest $D$ during the measurement period also coincided with peak $\lambda E$ values in late July. Beginning mid to late August 1998, daytime $\lambda E$ fell rapidly as soil water potentials dropped below -1 MPa despite $D$, $Q$, and $T$ remaining high. Daytime $\lambda E$ remained low throughout the rest of August and September when October rains brought about a sharp change in the mean direction of $H$ from positive to negative.

Cumulative totals of the energy budget components for 1998 were as follows with the number of missing half hours shown in brackets (most of these missing half hours were attributed to a week of missing eddy covariance data in April): $R_n$ = 2205 MJ $day^{-1}$ $m^{-2}$ (0), $H$ = 627 MJ $day^{-1}$ $m^{-2}$ (366), $\lambda E$ = 965 MJ $day^{-1}$ $m^{-2}$ (368), $G$ = -12 MJ $day^{-1}$ $m^{-2}$ (55), and $J$ = 0.18 MJ $day^{-1}$ $m^{-2}$ (2) where $\lambda E$ was uncorrected.

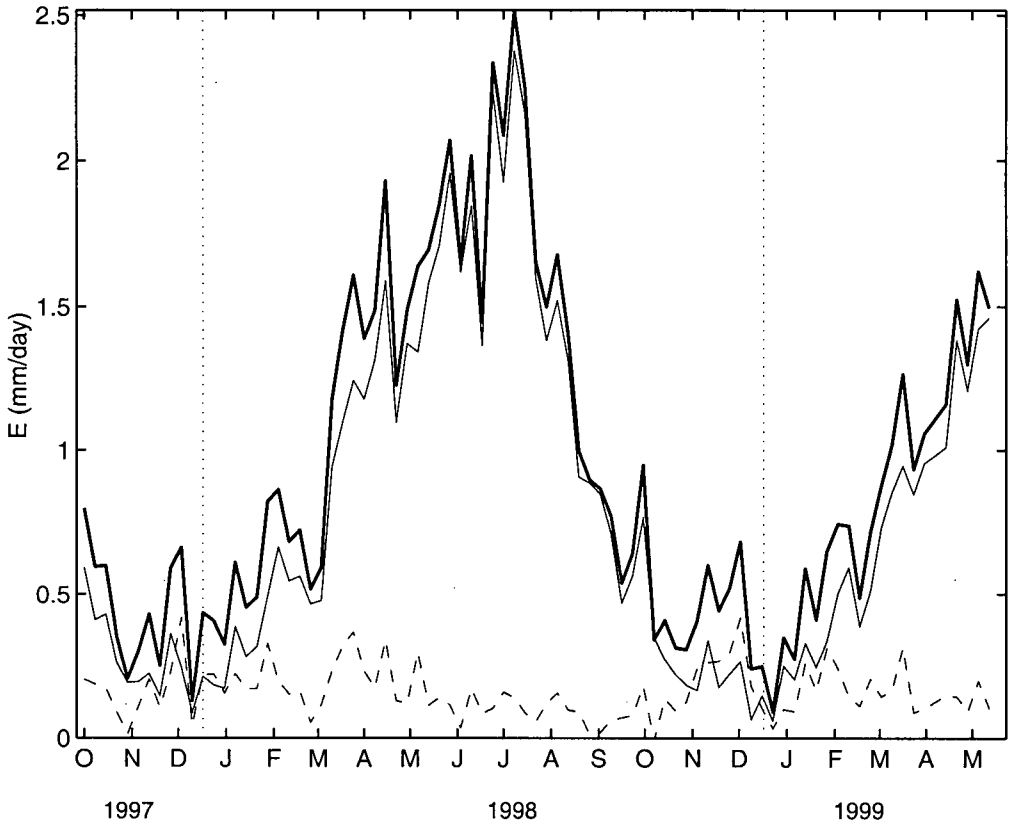


Fig. 4.19 Mean 24-h evaporation ($E$) (thick solid line), mean daytime evaporation when $S\downarrow > 0$ (thin solid line) and mean nighttime evaporation (dashed line) over 7-day periods between October 15 1997 and May 31, 1999. No corrections were applied to $\lambda E$.

Although significant evaporation occurred during the winter months, evaporation rates were considerably greater during the summer months (Fig. 4.19). Monthly total evaporation reached a maximum of 66 mm in July 1998, while total evaporation over the four winter months (November to February) was 56 mm in 1997/98 and 53 mm in 1998/99 with all values uncorrected. Maximum 24-h evaporation rates did not exceed 3.56 mm day$^{-1}$ (July 1998). Mean summer evaporation rates ranged from 0.9 to 2.1 mm day$^{-1}$. Winter maximum evaporation rates reached as high as 1.60 mm day$^{-1}$ (February 1999) but tended to average to 0.3 to 0.7 mm day$^{-1}$. The mean evaporation rate between April and September, 1998 was 1.57 mm day$^{-1}$ while it was only 0.47 mm day$^{-1}$, during both winter seasons between November and February.

Despite the cooler, wetter weather of 1998/99, there was little difference between the two winter season evaporation rates at 0.47 mm day$^{-1}$ during 1997/98 and 0.45 mm day$^{-1}$ during 1998/99. The spring months of April and May experienced greater evaporation rates of

1.54 mm $day^{-1}$ (94 mm) in 1998 and 1.34 mm $day^{-1}$ (70 mm) in 1999. Including spring and fall months, the proportion of rainfall evaporated was 8.6% for October 1997 to March 1998, inclusive, 6.5% for October 1998 to March 1999 and 137.7% for April 1998 to September 1998 (where missing $E$ values were filled according to Section 3.5.6).

Again, due to an increased likelihood of high frequency losses in $\lambda E$ during high humidity conditions, corrections for a 38% flux loss increased summer 1998 totals (April to September inclusive) from 297 mm to 316 mm (missing $E$ values filled for these totals). Winter totals during 1997/98 (November to February inclusive) increased from 56 mm to 76 mm while 1998/99 values increased from 52 mm to 65 mm, respectively. This changed the total proportion of rainfall evaporated for the summer of 1998 to 146.3% and for the winters of 1997/98 to 11.4% and for 1998/99 to 8.1%. Applying Bowen ratio corrections to daytime data further increased these proportions to 176.7% for the summer, 15.9% for the winter of 1997/98 and 12.8% for the winter of 1998/99. Bowen ratio corrections had a considerable impact but may be a questionable practice when the energy budget closure discrepancy may be due to advection/drainage terms which were not accounted for.

An additional 3 mm of water evaporated from the canopy during the El Niño winter (1997/98) despite an extra 250 mm of precipitation during the La Niña winter (1998/99). Mean $T$ and $D$ were only slightly different between the two winters. Between November 1998 and the end of February 1999, it was slightly cooler with mean $T$ equal to 2.2 ± 2.6°C, while it was 3.6 ± 3.0°C (± 1 s.d.) the previous year. As a result, there was slightly less atmospheric demand with daytime mean $D$ lower in 1998/99 at 0.05 ± 0.09 kPa than in 1997/98 when it was 0.09 ± 0.10 kPa (± 1 s.d.). Similar daytime $Q$ and $R_a$ and similar rates of downward $H$ were apparent for the two winters (Fig. 4.18). However, much more precipitation fell as snow in 1998/99 covering the ground for almost 3 months compared to only 4 days in 1997/98. This could have meant that there was less intercepted precipitation as the heavy snow fell to the ground. In addition, the snow was not directly available for evaporation except through sublimation. Finally, with snow melt, there would have been a greater proportion of total precipitation infiltrating into the soil in 1998/99.

Few studies of temperate forests have reported winter evaporation rates. A southern mixed deciduous forest in Tennessee had rates typically less than 0.8 mm $day^{-1}$ (Greco and Baldocchi, 1996), while evaporation rates for a boreal aspen forest were generally less than 0.5 mm $day^{-1}$ (Black et al., 1996). Thom and Oliver (1977) estimated that winter, wet canopy evaporation

rates could be as large as 2 to 3 mm day$^{-1}$. Evaporation rates from the Tennessee forest were similar to ours, despite the bare canopy, likely due to the similar rainfall rates and mild winter temperatures. In contrast, precipitation fell as snow during the winters at the aspen forest and temperatures remained well below freezing.

Peak values of daily evaporation for younger Douglas-fir forests 7 to 9 m tall with LAI ranging from 5 to 6.6 on Vancouver Island and near Haney, B.C. were considerably higher ranging from 4.2 to 4.8 mm day$^{-1}$ (McNaughton and Black, 1973; Price and Black, 1990; Tan et al., 1978). Applying the attenuation and Bowen ratio corrections as outlined in Section 3.5.6 increased the maximum evaporation rate to 4.2 mm day$^{-1}$. This may be a more realistic comparison as two of the previous studies were carried out using the BREB method assuming energy budget closure. Kelliher et al. (1993) summarized a total of 18 reports describing maximum evaporation rates from coniferous forests ranging from 2.4 mm day$^{-1}$ for *Pinus radiata* in Haupapa to 3.5 mm day$^{-1}$ for *Pinus radiata* at Mt. Gambier, Australia and as high as 4.8 mm day$^{-1}$ for the Douglas-fir in Haney, BC. Our uncorrected maximum of 3.6 mm day$^{-1}$ was exactly mid range. Recent reports of maximum evaporation rates for a 215-year-old *Pinus sylvestris* forest in Siberia with LAI = 1.5 were less than ours at 2.3 mm day$^{-1}$ (Kelliher et al., 1998) while a 50-year-old stand of *Picea abies* and *Pinus sylvestris* with an LAI = 4-5, were greater at 4 mm day$^{-1}$ (Grelle et al., 1997). A boreal Jack pine forest 13.5-m tall with an LAI = 1.9-2.2 had a maximum evaporation rate of 3.3 mm day$^{-1}$ with mean summer rates around 1.5 mm day$^{-1}$ (Baldocchi et al., 1997). Mean summer rates of 1.6 to 1.7 mm day$^{-1}$ in an open (LAI = 1.6) mixed age Ponderosa pine canopy in Oregon were very similar to ours with maximums of 4 mm day$^{-1}$ observed after rain (Anthoni et al., 1999).

Clearly, water loss to the atmosphere from this canopy was dominated by dry canopy, summer evaporation, primarily through the process of transpiration. However, this forest was relatively unique in the consistently large amounts of water loss throughout the winter on a 24-h basis and during the night, year-round. Downward $H$ provided the energy with which evaporation proceeded under these conditions during both summer and winter seasons (Fig. 4.18 and Fig. 4.19) and will be discussed further below.

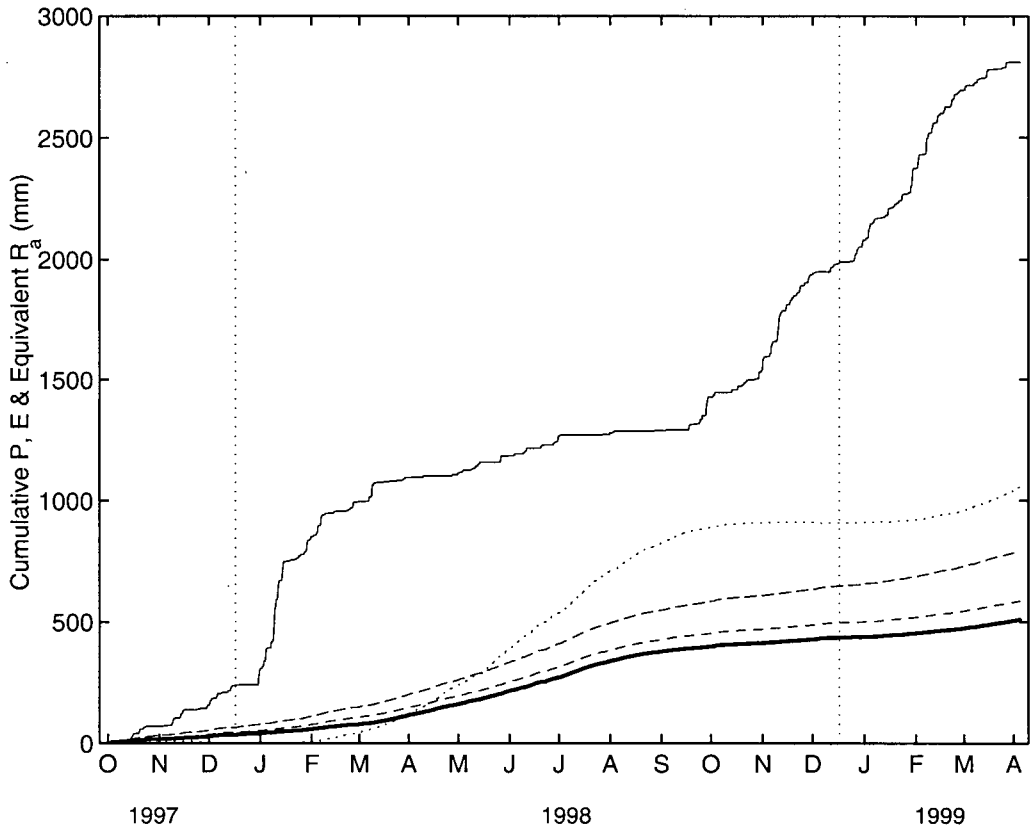


Fig. 4.20 Cumulative rainfall, $P$ (thin solid line), measured evaporation, $E$ (heavy solid line) and available energy, $R_a$ expressed in equivalent mm (dotted line). Also shown are corrections to $E$ for signal attenuation as indicated by calculated delay times (dash-dotted line) and an additional daytime Bowen ratio correction (dashed line). Missing half hour measurements of $E$ and $R_a$ were linearly interpolated. Corrected $\lambda E$ missing values were filled according to Section 3.5.6. Cumulative sums ended April 19 when a week of missing flux data occurred.

Cumulative sums for the 551 days of measurements ending April 19, 1999 resulted in 2812 mm of rainfall, 1057 mm of equivalent $R_a$ and 510 mm of total evaporated water (Fig. 4.20). With the applied corrections outlined in Section 3.5.6, evaporation increased to 586 mm with only the signal attenuation correction and 793 mm with both the signal attenuation correction and the Bowen ratio correction applied to daytime data. In total, evaporated water was measured to account for 18% of rainfall or 20% to 28% with measurement corrections.

On an annual basis for 1998, total rainfall amounted to 1751 mm, while total evaporation without corrections was 402 mm with 74% of the total occurring between April and September

1998, inclusively. Total evaporation for 1998 increased to 452 mm using only the signal attenuation correction and 584 mm using both corrections.

Evaporation from the wet canopy appeared to be significant throughout the year. Uncorrected evaporation measurements during rainfall amounted to 49 mm or 10% of the total measured evaporation for the study period. When the canopy was saturated but not necessarily during rainfall events, evaporation accounted for 8% of the total evaporation equivalent to 41 mm. When the canopy was partially wet, evaporation totaled 148 mm or 29% of the total evaporation. Evaporation from the dry canopy accounted for the largest proportion of the total evaporation at 63% with 321 mm.

### 4.4.3 Energy Partitioning and Controls

#### 4.4.3.1 Bowen ratios and the Evaporative fraction, $\lambda E/R_a$

During the summer months, convective energy exchange was dominated by $H$. As a result, daily daytime β calculated as $\sum^{n} H \Big/ \sum^{n} \lambda E$, where $n$ is the total number of half hours for each day when $S\downarrow > 0$ W m$^{-2}$, generally ranged between 1.3 and 3.5 reaching a maximum value of 4.1 in September (Fig. 4.21). On a monthly basis from May through September 1998, median β ranged from 1.3 to 2.7. Similar results have been obtained using the eddy covariance method for younger Douglas-fir forests on Vancouver Island with β values varying from 1.9 to 2.7 during a dry period in July (Lee and Black, 1993). Ratios of total daytime $\lambda E$ to total daytime $R_a$, calculated on a daily basis, were small during the summer months generally ranging from 0.18 to 0.40 with minimum daily values as low as 0.15. The median values determined for each summer month ranged from 0.23 to 0.36. As daytime energy budget closure was ~80% during the summer months, daily $\lambda E/R_a$ ranged from 0.25 to 0.48 with monthly medians ranging from 0.31 to 0.47 following the application of the attenuation and Bowen ratio corrections of Section 3.5.6.

Summer β values for days when the canopy was wet for at least one half hour were consistently smaller than the average (+ symbols in Fig. 4.21). This indicated that evaporation responded immediately to canopy wetting likely through the rapid evaporation of intercepted water. On a slightly longer time scale, β varied with ramp-like patterns through the growing season, shown by the running mean in Fig. 4.21. One example of this occurred between May 15

and May 31, 1998. These patterns were correlated with storm events (not shown), where a gradual increase in β was observed as the soil dried out following a storm. Following a storm event, β decreased as much of the available energy was used to evaporate the intercepted rainfall. Once the canopy dried, evaporation was dominated by transpiration limited increasingly by physiological control as the soil dried. Bowen ratios tended to increase in value by less than 1 during these ramp-like periods, while β was found to increase in increments as large as 4 in a

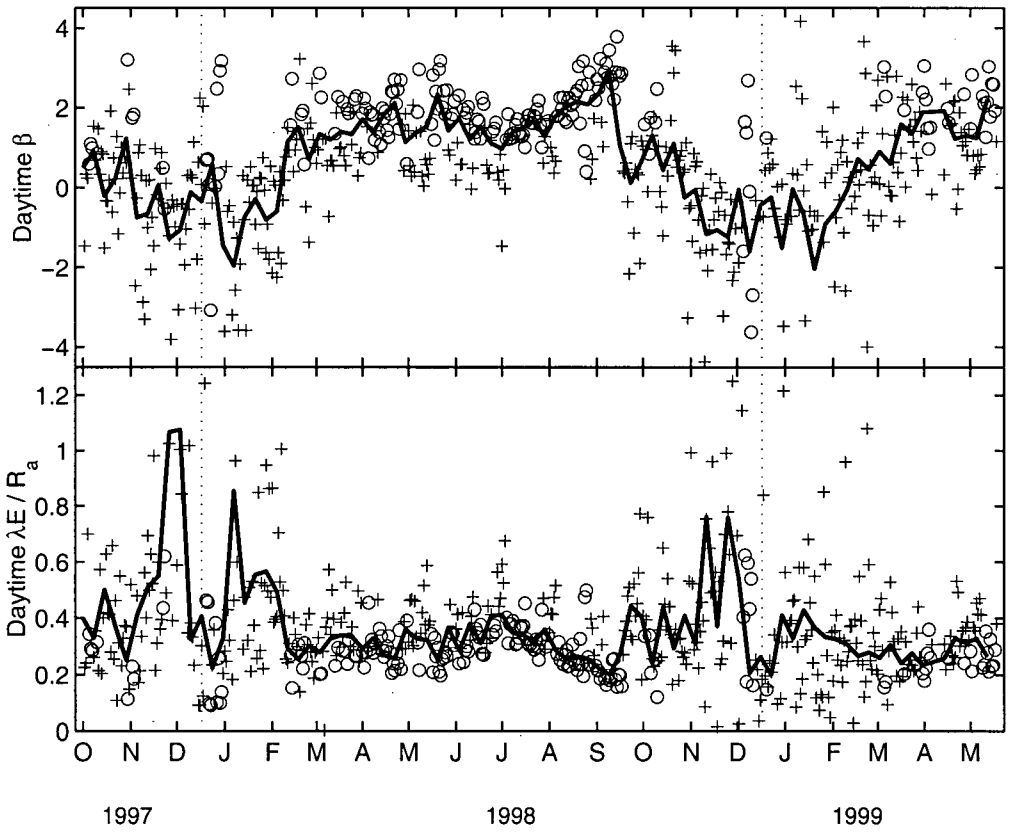


Fig. 4.21 Bowen ratios (top panel) and $\lambda E / R_a$ (bottom panel) calculated from daytime totals (+ for wet days, O for dry days) and as a 7-day running mean (solid line). No corrections were applied to $\lambda E$ or $H$.

young 3-m tall boreal jack pine forest (McCaughey et al., 1997).

Daily $\lambda E / R_a$ was observed to steadily decrease from about 0.4 to 0.15, while β increased from about 1 to 3.5 between July 1998 and September 1998 indicating an increase in $H$ at the expense of $\lambda E$ (Fig. 4.21). Soil water potential clearly influenced the partitioning of available

energy. During this period, only 76 mm of rain fell with less than 6 mm of rainfall occurring in September 1998 (Fig. 4.15). Volumetric water content steadily decreased between July and late September from 25% to 15% with soil water potentials decreasing from -0.01 MPa to -1.21 MPa (Fig. 4.15). Pre-dawn twig water potentials recorded in mid-August were on average -0.88 ± 0.14 MPa (± 1 s.d.). Air temperature, $Q$ and $D$ were also observed to decrease throughout this period, however they were not likely low enough to be limiting. Tan and Black (1976) found $\lambda E/R_n$ from a Douglas-fir forest to fall from about 0.6 to 0.3 with a decrease in soil water potential from 0 to -1.05 MPa.

During the two winter seasons, a greater proportion of the available energy was partitioned into $\lambda E$ with monthly median $\lambda E / R_a$ varying from 0.27 to 0.53 and median β varying from -0.63 to 0.53 determined from daily values within each month between November and February, inclusively. Maximum daytime $\lambda E/R_a$ reached values as high as 3.57. With both signal attenuation and Bowen ratio corrections, monthly median $\lambda E / R_a$ was found to vary from 0.67 to 1.20 while β varied from -0.13 to 0.21. Individual days observed to deviate from these trends were days where the canopy was determined to be completely dry. In these relatively rare instances, β could be found to increase to summer-like values from 2 to 3, while the corresponding $\lambda E/R_a$ values decreased to as low as 0.1 to 0.2.

### 4.4.3.2 Priestly-Taylor α and McNaughton and Jarvis Ω values

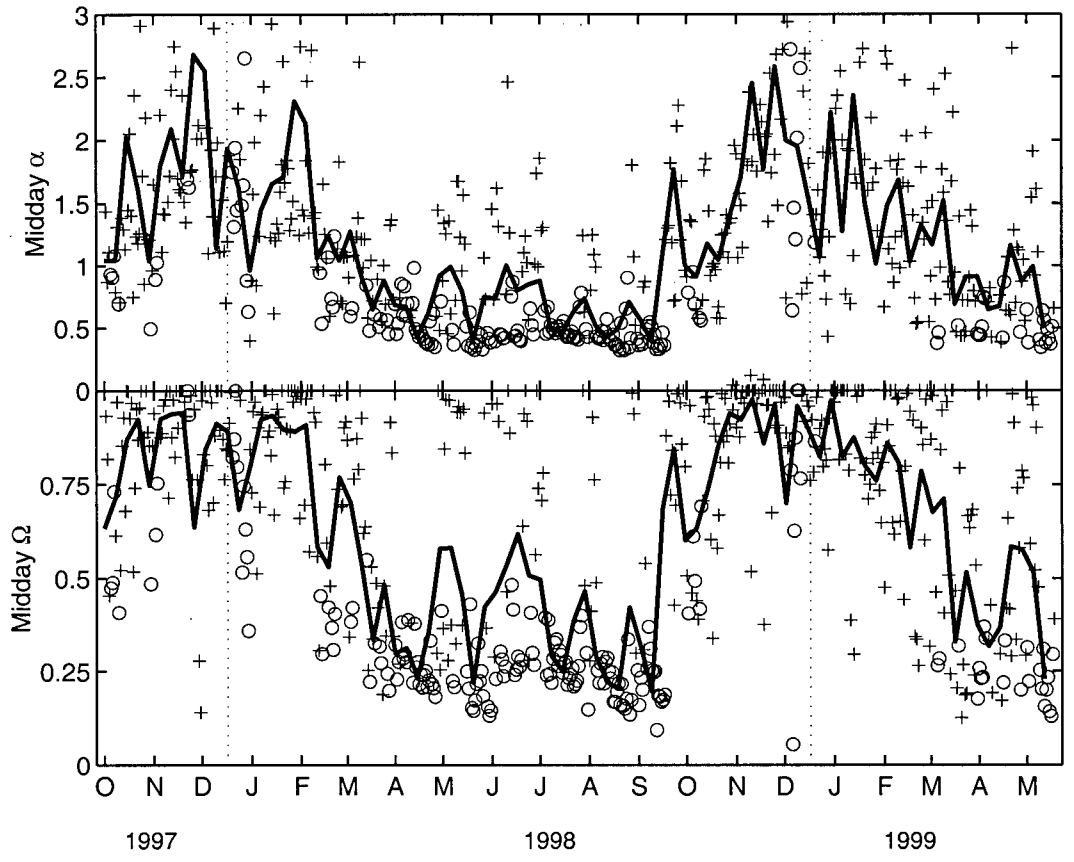


Fig. 4.22 Priestley-Taylor α values throughout the measurement period (top panel) as means for each midday period between 1100 h and 1430 h PST (+ for wet days, O for dry days) and as 7-day running means of midday periods (solid line). The bottom panel shows the atmospheric decoupling coefficient, Ω in the same manner for midday periods. $\lambda E$ used to compute both values was corrected using the maximum attenuation and Bowen ratio correction (Section 3.5.6). This led to a mean increase of 42% and 35% in Ω and α during the summer periods, respectively, while the increase was 101% and 69%, respectively, during the winters.

Throughout the summer, when the canopy was primarily dry, the midday values of the Priestley-Taylor α and the McNaughton and Jarvis Ω values indicated the importance of surface controls on evaporation rates. Fig. 4.22 shows both parameters calculated for midday periods with $\lambda E$ corrected using both attenuation and Bowen ratio corrections as outlined in Section 3.5.6. Values of α were calculated as $\sum^{n} \lambda E \Big/ \sum^{n} \lambda E_{eq}$ where $n$ is the six half hours for each day between 11:00 h and 14:30 h PST. Between April and September, α was consistently low

ranging from 0.30 to 0.70 or 0.20 to 0.55 without corrections. Median values for these months ranged from 0.43 to 0.61 or 0.30 to 0.49 without corrections (Fig. 4.22). Most midday $\alpha$ values deviating from this range were during days when the canopy was wet for at least one half hour. Consistent with high $\beta$ and low $\lambda E/R_a$ values observed throughout the summer, these low $\alpha$ values indicated a water-limited system with $R_a$ partitioned largely into $H$ rather than $\lambda E$ (Priestley and Taylor, 1972). These low $\alpha$ values were also consistently lower than the 1.26 attributed to $\alpha$ for a wide range of extensive surfaces not experiencing significant moisture stress (McNaughton and Spriggs, 1989). However, this forest was not very likely experiencing drought stress until late July as soil water potentials were well above -0.5 MPa (Fig. 4.15). Between late July and late September, $\alpha$ values appeared to decline somewhat (Fig. 4.22) as soil water potential declined to -1.2 MPa (Fig. 4.15). However, mean midday values were not considerably lower than in previous summer months (June: 0.70 ± 0.54, July: 0.73 ± 0.41, August: 0.56 ± 0.27, September: 0.53 ± 0.33).

Values of $\alpha$ less than 1.26 for daytime, dry canopy conditions, regardless of drought stress, have also been found for a spruce forest in Plynlimon, Wales and for Scots pine in the Thetford forest in Norfolk, England (Shuttleworth and Calder, 1979). The $\alpha$ values for these forests ranged from 0.50 to 0.81, determined from total $\lambda E$ measured throughout the entire year. Using the same method at our site for both daytime and nighttime, $\alpha$ was equal to 0.80 with corrections and 0.60 without. McNaughton and Jarvis (1983) also found $\lambda E$ to decline below $\lambda E_{eq}$ corresponding to an $\alpha$ of approximately 0.27 when $\lambda E > 50$ W m$^{-2}$ in a Sitka spruce stand 11.5 m tall with an LAI = 9 in northeast Scotland (determined from Fig. 1. in McNaughton and Jarvis, 1983). Values of $\alpha$ (some values inferred from reported values of $\lambda E/R_n$) for a variety of relatively unstressed, dry canopy boreal coniferous stands were near 0.5 (Baldocchi et al., 1997), 0.24 to 0.36 (Lindroth, 1985) and about 0.28 (Pattey et al., 1997). Conversely, McNaughton and Black (1973) found $\alpha$ approaching 1.05 for dry canopy conditions in a 7.8 m tall Douglas-fir forest well supplied with water in Haney, B.C., while a similar sized, unstressed Douglas-fir stand in Courtney tended to show values of 0.5 (Tan et al., 1978). Differences have been suggested to be related to greater atmospheric demand within continental climates vs. maritime climates (Jarvis et al., 1976); however, these reported values for coniferous forests were not consistent with this hypothesis.

Physiological control, quantified by $g_c$, must have played a significant role in the reduction of evaporation rates well below equilibrium rates when the canopy was dry and transpiration was the dominant evaporation process. The decoupling coefficient ($\Omega$), described by Equation (2.4), was introduced by McNaughton and Jarvis (1983) to describe the degree of interaction between the canopy and the atmosphere. Forests are expected to have values around 0.1 to 0.2 as the aerodynamically rough surface of these canopies causes $g_a \gg g_c$ such that transpiration rates are dependent on canopy conductance and the saturation deficit. Grasslands and low agricultural crops are expected to have $\Omega$ values around 0.8 to 0.9 such that transpiration rates are weakly related to the saturation deficit of the air and closely follow $R_a$. Fig. 4.22 shows the seasonal variation of midday $\Omega$ values (averaged for the six half hours between 11:00 h and 14:30 h PST) computed using $\lambda E$ corrected with both attenuation and Bowen ratio corrections. In order to ensure that $\Omega$ ranged from 0 to 1, $g_c$ values less than zero were set to zero for use in Equation (2.4). Negative $g_c$ derived from a manipulation of the Penman-Monteith equation (Equation (2.7)) were often found for wet conditions. Although the apparent surface conductance for saturated canopy conditions should have been zero, any errors in the micrometeorological measurements or in the determination of $g_a$ resulted in non-zero values of $g_c$ (Stewart, 1977). Throughout the summer months, the median $\Omega$ determined from individual midday values over each month ranged from 0.21 to 0.33 (0.15 to 0.28 without corrections) indicating an aerodynamically rough canopy well coupled to the saturation deficit of the air.

During the two winter seasons extending from November to February, inclusively, the canopy was wet for a total of 70% of the time. Monthly median values of $\alpha$ ranged from 1.25 to 1.66 (0.45 to 0.66 without corrections). Monthly mean values of $\Omega$ ranged from 0.83 to 0.91 (0.45 to 0.63 without corrections), while median $\Omega$ values with corrections were consistently 1.0 for all eight winter months while uncorrected medians varied from 0.40 to 0.61. In general, $\lambda E$ from the wet canopy tended to approach rates predicted by a Priestley-Taylor $\alpha$ of 1.26. As a result, the forest surface conductance was no longer limiting and $\lambda E$ appeared to be primarily limited by radiative energy inputs and less coupled to the saturation deficit of the air. However, there were 292 days when mean midday $\alpha$ computed with corrections was greater than 1.0, 30% of which were over 2. Without corrections, 59 days were recorded with mean midday $\alpha$ greater than 1.0, 24% of which were over 2. The largest midday mean $\alpha$ recorded was 8.26 with no corrections on January 26, 1998 and 6.47 on December 20, 1997 with corrections. Shuttleworth

and Calder (1979) found $\alpha$ values in excess of 9 for 3 years of total evaporation measured during wet daytime conditions at the Plynlimon forest, while the Thetford forest $\alpha$ of 1.50 was more similar to our site. During the growing season, maximum $\alpha$ was about 3 with or 1.5 without corrections, when the canopy was at least partially wet. In general, our uncorrected, wet canopy $\alpha$ values for the growing season were similar to those found for a wet boreal jack pine stand where $\alpha$ was about 0.75 (Baldocchi et al., 1997). Using total $\lambda E$ over wet conditions during both winter and summer seasons, overall $\alpha$ was 2.29 with corrections and 1.25 without.

Values of $\alpha$ exceeding 1 and 1.26 over forests illustrate the possibility for relatively high $\lambda E$ despite low incident radiation. This is possible as turbulent transport above an aerodynamically rough canopy allows water to evaporate as a function of atmospheric demand and be carried away from the canopy despite stable atmospheric conditions (McNaughton and Jarvis, 1983). Key to this process is the source of energy required for the evaporation of water and the maintenance of a non-zero $D$ in the atmosphere above the canopy.

To further emphasize the differences in $\lambda E$ between a dry summer month and a wet, winter month, evaporation statistics were tabulated for July 1998 and December 1998 (Table 4.4). Daily rainfall was 3 times greater in December than in July, while the mean daytime evaporation rate in December was only a fifth of that in July. After applying attenuation and Bowen ratio corrections to $\lambda E$, median daytime $\beta$ approached unity in July. $\lambda E/R_a$ approached unity in December. Finally, $\alpha$ values computed with the corrections were high in December with a mean of 1.46 or median of 1.23, very close to often cited $\alpha$ of 1.26 for a variety of surface types well supplied with water (McNaughton and Spriggs, 1989). July mean $\alpha$ was much lower with a median of 0.53 indicative of a water-limited surface.

Table 4.4 Rainfall ($P$), evaporation rates ($E$), evaporative fraction ($\lambda E/R_a$) and $\alpha$ and $\Omega$ for July 1998 and December 1998 to illustrate differences between winter and summer seasons. Also shown are the values for evaporation with the maximum corrections including 38% flux loss correction with subsequent daytime Bowen ratio correction. Median values are shown in brackets

| | July 1998 | | | December 1998 | | |
|---|---|---|---|---|---|---|
| | mean ± s.d. | Range | corrected mean ± s.d. | mean ± s.d. | Range | corrected mean ± s.d. |
| $P$ 24 hr (mm day$^{-1}$) | 1.84±4.79 | 0 : 22.84 | | 5.64±7.16 | 0 : 25.38 | |
| $E$ 24 hr (mm day$^{-1}$) | 2.13±0.82 | 0.46 : 3.56 | 2.66±0.81 | 0.45±0.37 | -0.02 : 1.56 | 0.72±0.56 |
| $E$ daytime (mm h$^{-1}$) | 0.12±0.10 | -0.08 : 0.51 | 0.12±0.12 | 0.02±0.03 | -0.03 : 0.20 | 0.03±0.06 |
| $\lambda E/R_a$ daytime | 0.38±0.09 (0.36) | 0.27 : 0.65 | 0.54±0.20 (0.46) | 0.27±0.56 (0.27) | -2.23 : 1.15 | 0.88±0.73 (1.03) |
| $\beta$ daytime | 1.12±0.74 (1.34) | -1.42 : 2.26 | 0.91±0.56 (1.02) | 0.51±10.13 (-0.46) | -21.63 : 46.04 | 0.23±5.51 (-0.13) |
| $\alpha$ midday (30 min values) | 0.53±0.23 (0.49) | 0.04 : 1.45 | 0.73±0.41 (0.55) | 0.74±1.20 (0.46) | -6.47 : 8.41 | 2.03±2.09 (1.66) |
| $\Omega$ midday (30 min values) | 0.35±0.20 (0.28) | 0.02 : 1.00 | 0.46±0.28 (0.33) | 0.55±0.35 (0.49) | 0: 1.00 | 0.86±0.28 (1.00) |

#### 4.4.3.3 Nighttime Evaporation

The energy required to support evaporation was observed as downward $H$ throughout the winter months and during nighttime periods year-round (Fig. 4.18). Nighttime evaporation provided further evidence that evaporation may be supported by non-radiative energy sources as suggested by Pearce and Rowe (1980). Fig. 4.23 illustrates the proportion of total 24-h evaporation occurring during the daytime. Nighttime evaporation was likely due to the evaporation of soil water and of intercepted water from the canopy when wet, as transpiration from Douglas-fir was assumed to be negligible at night. As expected, nighttime evaporation was important to total evaporation generally throughout the wet, winter months. Between November and February, inclusive during both winter seasons, nighttime evaporation contributed to 44% (42% with signal attenuation corrections) of total evaporation and up to 100% of the total evaporation on a daily basis. The contribution of nighttime evaporation to total evaporation,

during the summer months, was only 10% (no change with corrections) and generally ranged from 0% to 20% on a daily basis. During the summer, the canopy was wet less often, less soil moisture was available for evaporation, and daytime rates of evaporation were generally higher than winter rates by a factor of about 3 (2 with corrections).

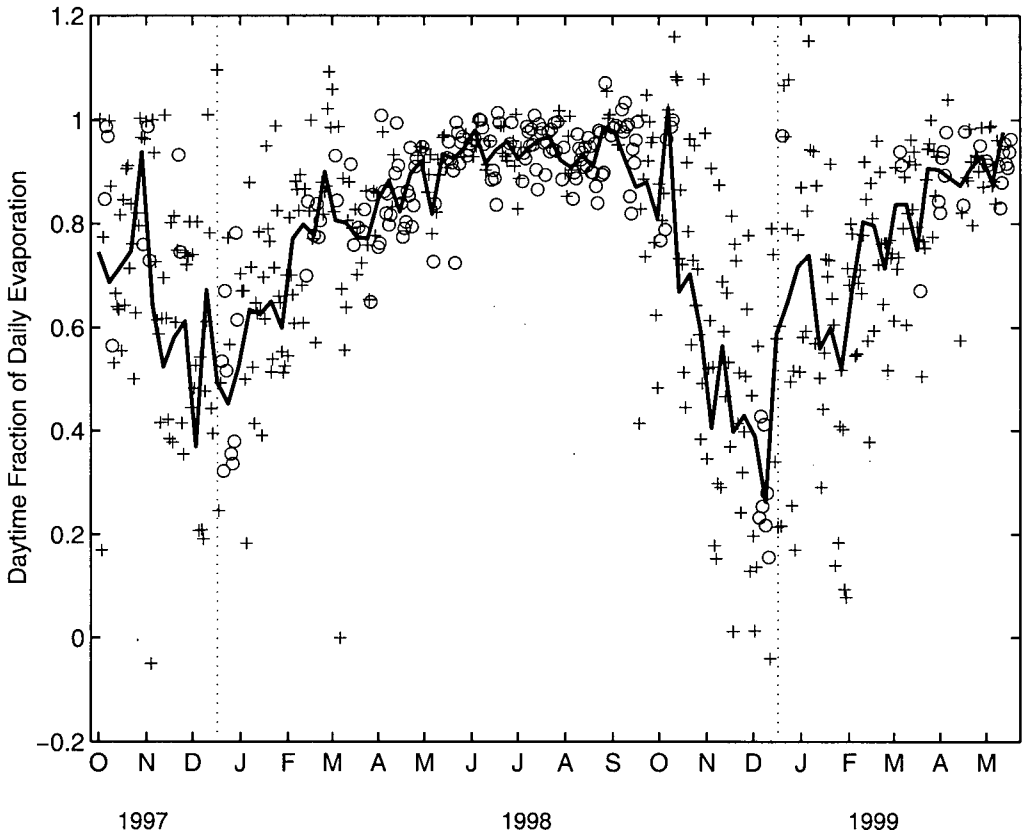


Fig. 4.23 Proportion of total 24-h evaporation occurring during the daytime (+ for wet days, O for dry days) and as a 7-day mean (solid line) throughout the measurement period October 15, 1997 to May 31, 1999. No corrections were applied to $\lambda E$.

## 4.5 DIURNAL PATTERNS OF EVAPORATION

### 4.5.1 Monthly Ensemble Averages

The diurnal patterns of the energy budget components and $\lambda E$ throughout the year supported the general trends observed for the seasonal variations described above. In particular, the seasonal variations in energy partitioning were clearly apparent in plots of the ensemble average of the energy budget components calculated for half hour intervals for selected months (Fig. 4.24). Plots of the wet winter months of January, November and February illustrated the very short days, low total $R_a$ and almost constantly negative $H$ resulting in high $\lambda E/R_a$ and low or negative $\beta$ values. Latent heat fluxes were low throughout the day but were evidently positive and significant for all three winter months shown. In fact, rates of nighttime and daytime $\lambda E$ began to approach the same values.

April 1998 was representative of a spring month where the canopy was dry most of the time while available soil water was high. Daytime convective fluxes were dominated by $H$ throughout most of the day while $\lambda E$ exceeded $H$ in the late afternoon. This phase shift was due to the high degree of coupling between the canopy and the atmosphere such that $\lambda E$ remained in phase with $D$ rather than $R_a$. This is a typical pattern for $\lambda E$ from Douglas-fir during the growing season (McNaughton and Black, 1973) and other coniferous forests (Lindroth, 1985; Pattey et al., 1997). Nighttime $\lambda E$ was relatively high during the spring due to intermittent wet canopy conditions and ample soil water. These positive nighttime $\lambda E$ were supported by heat extracted from the air as indicated by negative $H$.

During July, the patterns begun in April continued with larger $\lambda E$ and greater $R_n$ throughout the daytime. Nighttime $\lambda E$ tended to be slightly lower and $H$ was less negative. By the end of the summer in September, when $\Psi_{soil}$ was the most negative, a greater proportion of $R_a$ was partitioned into $H$ with late afternoon $\lambda E$ no longer exceeding $H$. Nighttime $\lambda E$ was virtually nil during this month and correspondingly, $H$ was only slightly negative.

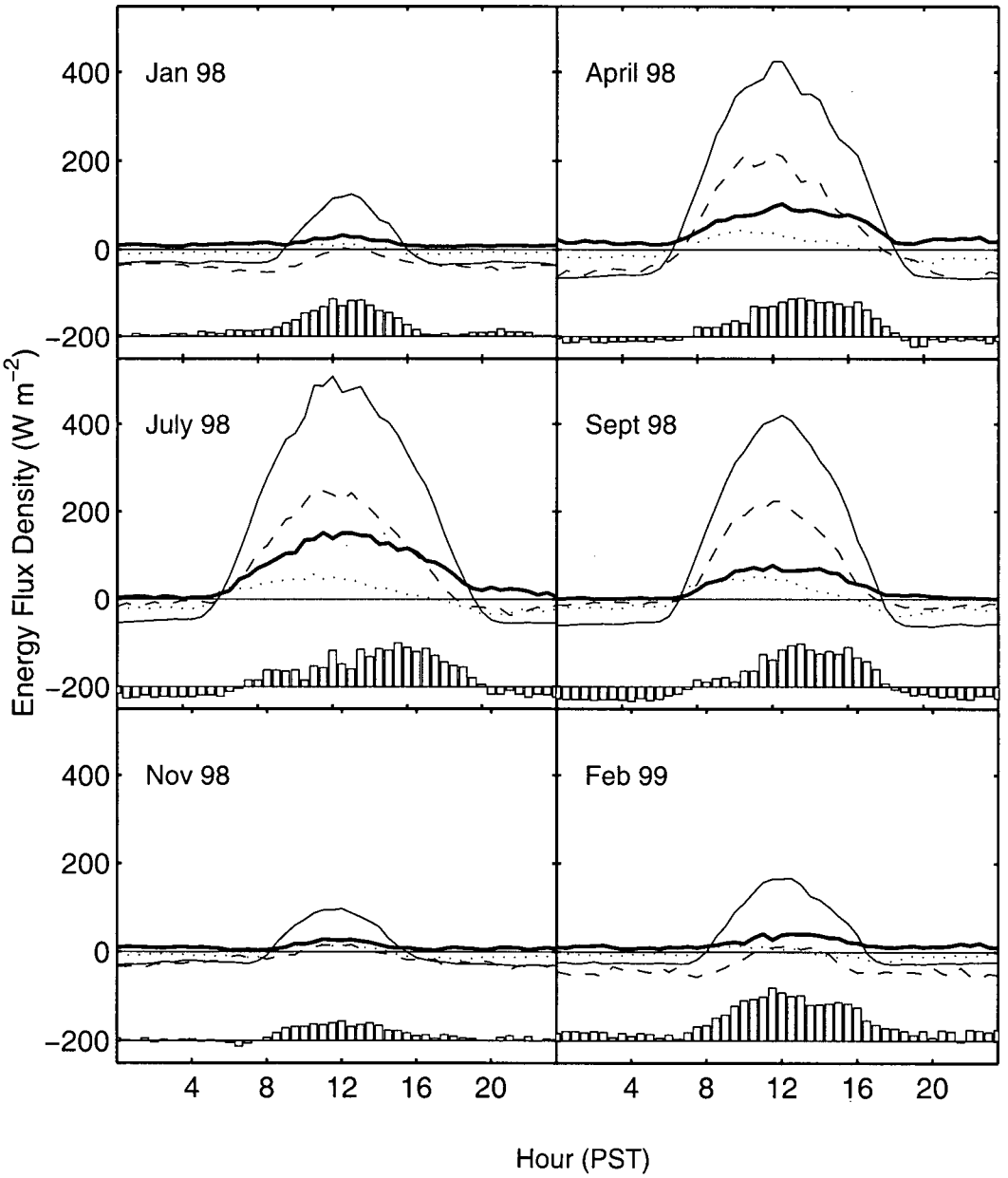


Fig. 4.24 Selected ensemble monthly averages of the half hourly, diurnal energy budget terms: $R_n$ (solid line), $H$ (dashed line), $\lambda E$ (thick solid line), $G + J$ (dotted line). Vertical bars illustrate the residual of energy budget closure, $R_n$ - $H$ - $\lambda E$ - $G$ - $J$ .

### 4.5.2 Evaporation from a Dry Canopy

#### 4.5.2.1 Daytime

By isolating particular 24-h periods within the seasonal trends discussed above, the various limitations and driving forces for evaporation from this forest canopy can be observed in greater detail. Again, seasonal variations in $\lambda E$ and controls on $\lambda E$ from this forest are integrally linked to the wetness of the canopy.

Beginning with dry canopy evaporation, Fig. 4.25 and Fig. 4.26 illustrate the diurnal patterns of $R_a$, $H$, $\lambda E$ and $\lambda E_{eq}$ for the start and end of the summer season, represented by May 29 and September 14, 1998. No corrections were applied to $\lambda E$. Also shown is the daytime canopy conductance ($g_c$) calculated with Equation (2.7), the total rainfall for each half hour, friction velocity ($u_*$) and saturation deficit ($D$). Half hours when the canopy was saturated or partially wet (see Section 3.3.3) are indicated along with periods when energy budget closure is adequate at $\pm$ 20% of unity. All times are reported in Pacific Standard Time.

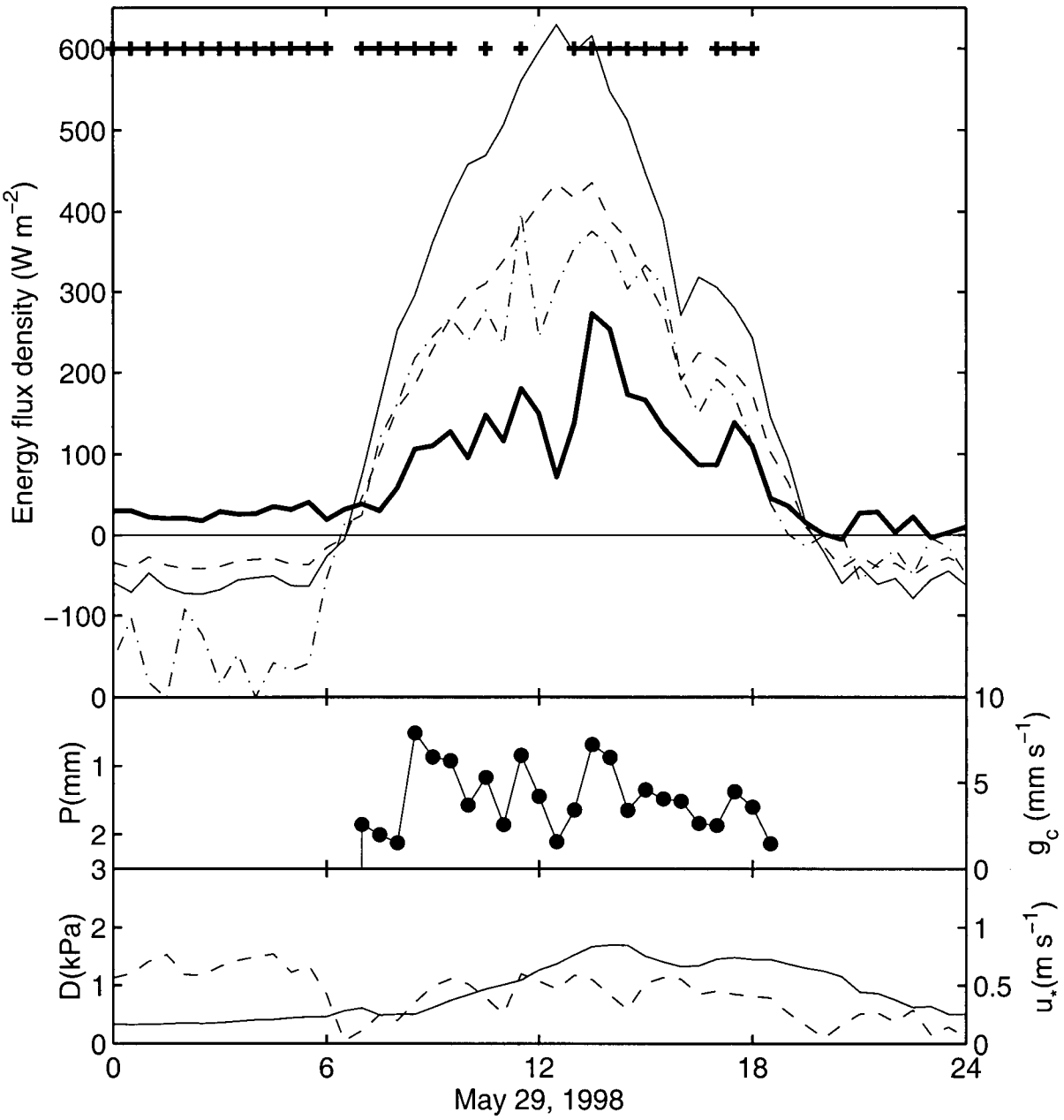


Fig. 4.25 Diurnal courses of energy budget components ($R_a$, thin solid line; $H$, dash-dotted line; $\lambda E$, thick solid line) and $\lambda E_{eq}$ (dashed line) for a dry canopy May 29, 1998. Daytime canopy conductance ($g_c$, ●) is illustrated in the center panel with precipitation (vertical bars). Vapour pressure deficit ($D$, solid line) and friction velocity ($u_*$, dashed line) are shown in the bottom panel.

Periods with good energy budget closure , ± 20% of unity (+) and with a saturated or partially wet canopy (○) are also indicated.

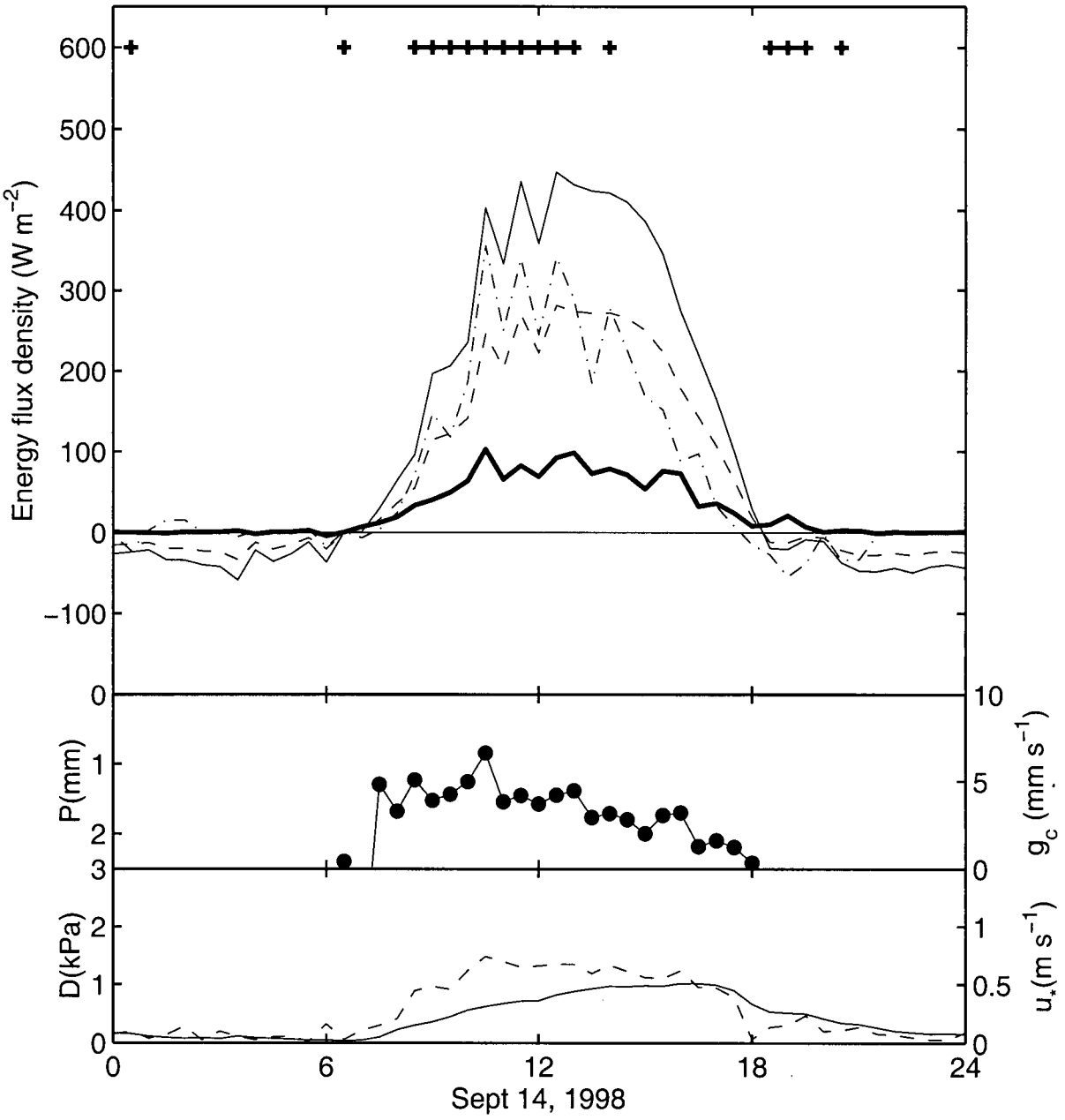


Fig. 4.26 Same as Fig. 4.25 for a dry canopy September 14, 1998.

The canopy was completely dry throughout both days. The most recent rainfall was within 17 hours prior to May 29 while it had been 78 hours for September 14. During the daytimes, $\lambda E$ was significantly lower than both $H$ and $\lambda E_{eq}$. For May 29 and September 14, $\beta$ was 1.7 and 2.8, $\lambda E/R_a$ was 0.33 and 0.21, and $\alpha$ was 0.48 and 0.34, respectively. Canopy conductance was quite low for both days with a maximum value of only 8 mm $s^{-1}$ and 6 mm $s^{-1}$, respectively. On both days, $g_c$ was observed to decline throughout the day (Fig. 4.25 and Fig. 4.26). This control was important in limiting $\lambda E$ well below $\lambda E_{eq}$ values. Since $g_a$ was high during this period at 50 to 80 mm $s^{-1}$ ($r_a$ = 10 to 20 s $m^{-1}$) under adequate wind speeds and $u_*$, $\lambda E$ did not follow the variations in $R_a$ but was largely influenced by $D$ as described by Equation (2.5). Latent heat flux tended to peak in the late afternoon and exceeded $H$ to a greater degree on May 29 than on September 14. This was likely a result of the larger decrease in $g_c$ throughout the afternoon for September 14 as $u_*$ and $D$ were similarly large for the two daytimes. Soil water was quite limiting by the end of the summer with $\theta_v$ = 0.16 ($\theta_v$ = 0.10 with CS615 measurements only) and $\Psi_{soil}$ = -1.12 MPa on September 14 while it was higher on May 29 with $\theta_v$ = 0.25 ($\theta_v$ = 0.15 with CS615 measurements only) and $\Psi_{soil}$ = -0.28 MPa. The trees were likely experiencing drought stress in September despite the recent rainfall events so that canopy control was able to suppress the tendency for higher $\lambda E$ in the afternoon driven by high $D$. Certainly this was reflected in the lower $\alpha$ and $\lambda E/R_a$ values for September 14. Latent heat fluxes and $H$ were also observed to be in phase with $R_n$ above the Thetford spruce forest under dry soil moisture conditions (Stewart and Thom, 1973). Canopy conductance for the Thetford forest also tended to be somewhat low with noon hour values around 7 mm $s^{-1}$ (Stewart and Thom, 1973).

The half hour variations of May 29 appeared to be artifacts of closure problems likely in the eddy flux measurements. Specifically, coincident peaks and dips of the two fluxes were contrary to maintaining the energy balance when $R_a$ was relatively constant.

#### 4.5.2.2 Nighttime

Nighttime $\lambda E$ and $H$ patterns were very different for the two days. May 29 experienced relatively large rates of evaporation (~ 40 W $m^{-2}$) and downward $H$ as large as 200 W $m^{-2}$ ($H$ = -200 $Wm^{-2}$) between 0 h and 06:00 h. The next evening, between 20:00 h and 24:00 h, closure was poor with $\lambda E$ and $H$ of smaller magnitudes. Friction velocity was greater in the early

morning at about 0.5 m $s^{-1}$, while it declined to about 0.1 to 0.2 m $s^{-1}$ in the late evening. However, $D$ was greater during the late evening declining from 1.3 to 0.5 kPa and 0.8 kPa on average. On September 14, $\lambda E$ was negligible throughout the night and early morning with $H$ only slightly negative due to radiative cooling of the canopy with slightly negative $R_a$. Both $u_*$ and $D$ were small throughout with a mean of 0.08 m $s^{-1}$ and 0.18 kPa.

Nighttime evaporation was largely due to evaporation of intercepted water and soil water evaporation as transpiration from the trees was assumed to be negligible. The canopy was found to be dry on both days, however a week of intermittent rainfall amounting to 32 mm ended only 17 hours before the May 29 case study. As a result, moisture may have remained on needles deep within the canopy. The ground foliage may have remained moist and soil water was certainly plentiful early in the summer with $\theta_v$ at 0.25. Therefore, water was available for evaporation, a large $D$ provided the atmospheric demand and $u_*$ was large indicating sufficient turbulent mixing for the transport of water vapour from the canopy and soil surface. Thus, in the absence of radiative energy, energy was extracted directly from the air to support evaporation. Few of these conditions existed during the night of September 14 as little water was available for evaporation and both atmospheric demand and turbulence were low.

Soil water evaporation was found to account for 4% to 7% of total evaporation for a period in August at this site. In general, evaporation of water from the forest floor ranges from 3% to 21% of total forest evaporation (Black and Kelliher, 1989). Values ranged from 7% to 13% for a similar Douglas-fir site in the Netherlands (Schapp et al., 1997), while values from a 13.5 m boreal jack pine stand ranged from 10% to 40% of total evaporation (5 to 25 W $m^{-2}$) (Baldocchi et al., 1997). As nighttime evaporation on May 29 accounted for 7% (0.17 mm) of the 24-h evaporation (2.33 mm), it was likely that evaporation from the canopy floor was large enough to account for nighttime evaporation rates at this site.

Nighttime evaporation, supported by downward $H$ is relatively rare for dry canopy conditions at various forests such as a boreal aspen forest (Black et al., 1996), a spruce forest in Germany (Laubach et al., 1994), and a mixed spruce forest in Sweden (Grelle et al., 1997), often despite adequate soil moisture for soil water evaporation. However, due to the extreme roughness of this canopy and the water available within the soil and on understory vegetation, positive $\lambda E$ was able to occur when the evaporative demand and turbulent conditions existed days after rainfall events.

### 4.5.3 Evaporation from a Drying Canopy

Fig. 4.27 illustrates the dynamic interaction of controls over evaporation from a drying canopy. Prior to October 17, 1998, there had been 8.4 mm of rainfall during the previous day following a 3-day dry spell. October 17 began with a rainfall amounting to 9.9 mm, exceeding the canopy saturation capacity. During the rainfall between 0 and 04:00 h, the atmosphere was unusually turbulent with a relatively high $u_*$ ranging from 0.2 m $s^{-1}$ to 1 m $s^{-1}$. However, with almost zero $D$, no radiative inputs (Fig. 4.27) and no temperature gradient through the canopy to drive evaporation, little water evaporated from the saturated canopy during this time. Just before and during sunrise, large negative $H$ was observed as $\lambda E$ exceeded both $R_a$ and $\lambda E_{eq}$. Between 06:00 h and 09:00 h, $\lambda E$ exceeded even potential evaporation rates as described by Equation (2.6). The rapid increase in $\lambda E$, despite a negligible $D$ at 6:00 h, was accompanied by a shift from upslope to downslope winds whose influence will be discussed below. By 08:30 h, the rain stopped, $R_a$ began to increase indicative of a clearing sky, while evaporation continued to exceed $\lambda E_{eq}$. However, downward $H$ was minimized as energy for evaporation began to be supplied by radiative inputs. By 12:00 h, high $D$ approaching 1 kPa and high $R_a$ contributed to extremely high $\lambda E$, exceeding 350 W $m^{-2}$ from the wet canopy. The canopy became dry shortly after 12:00 h. However, as $\lambda E$ continued at the equilibrium rate indicative of unlimiting $g_c$, there was likely a source of free-standing water deep within the canopy, on the ground vegetation and/or from the rain-wetted soil surface. Overall, daytime $\alpha$ was 1.29, $\lambda E/R_a$ was 0.73, and $\beta$ was -0.04.

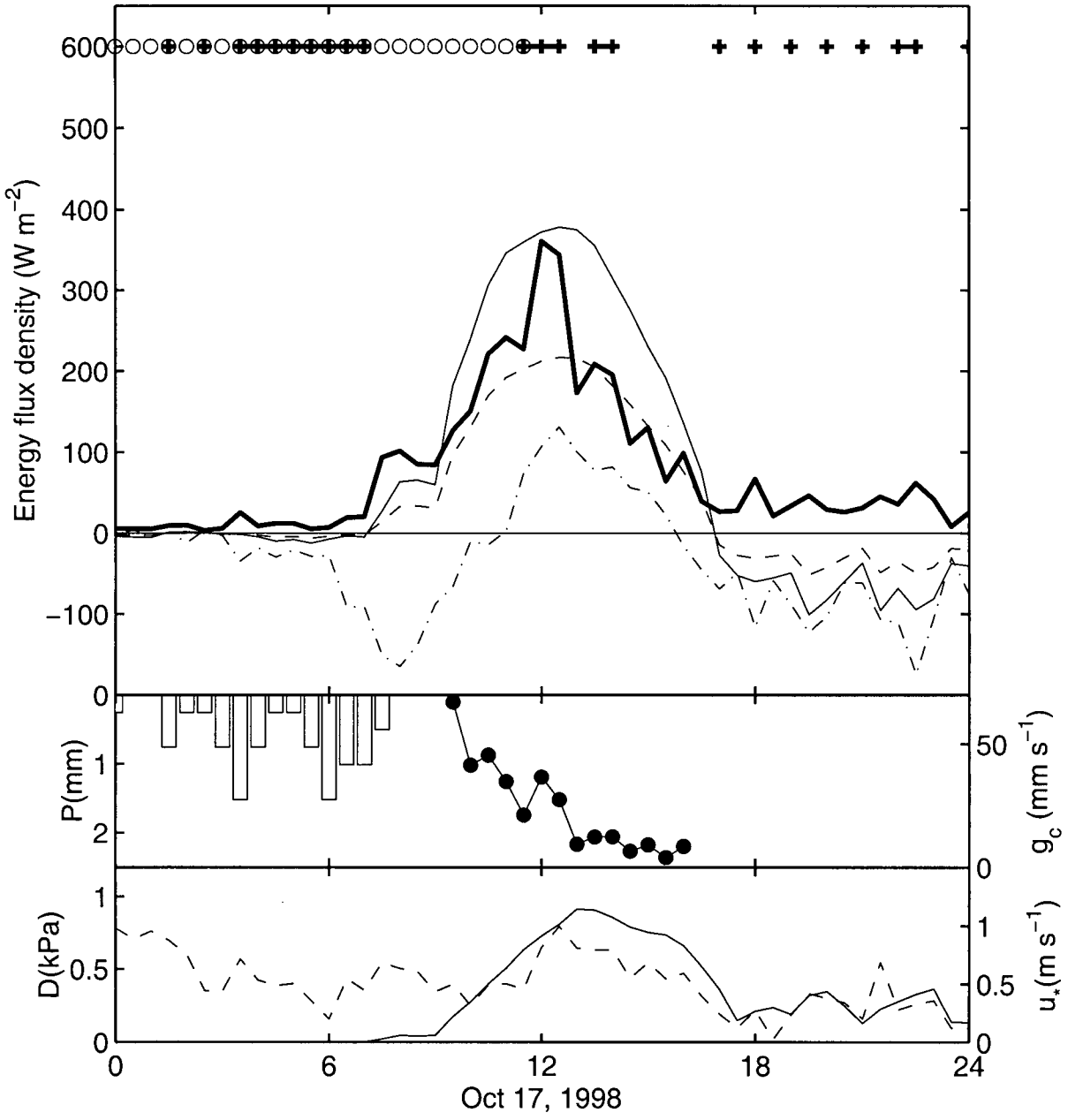


Fig. 4.27 Same as Fig. 4.25 for a rain saturated canopy drying over October 17, 1998. Note that the $g_c$ axis ranges from 0 to 70 mm s$^{-1}$.

High rates of evaporation continued throughout the night ranging from 30 to 66 W $m^{-2}$ between 18:00 h and 24:00 h. Energy was supplied by large negative $H$ making $\beta$ large and negative at -2.7. Conditions during this period differed from the early morning in that rain was not falling, $u_*$ was slightly lower ranging from 0.12 to 0.69 m $s^{-1}$, and $D$ was considerably larger at about 0.25 kPa. As a result, the atmospheric demand appeared to be critical for significant evaporation to occur. Grelle et al. (1997) also found that for nighttime evaporation to occur during rainfall events, $D$ must be greater than zero regardless of a high $u_*$. Conversely, during the daytime, when a temperature gradient may be established with radiative input, non-zero $D$ would not be strictly required although $D$ was almost always non-zero during the daytime.

These results were in agreement with those found by Mizutani et al. (1997) over an evergreen broad-leaved forest where evaporation of intercepted rainfall estimated by the eddy correlation/energy balance method was largely dependent on wind speed and $D$. They observed downward $H$ as large as 200 W $m^{-2}$ ($H$ = -200 W $m^{-2}$) supporting $\lambda E$ up to 400 W $m^{-2}$ with additional energy inputs from $R_n$ when wind speed was at least 2 m $s^{-1}$ and $D$ was about 0.1 kPa. However, these observations occurred during rainfall whereas our measurements of evaporation were not large until rainfall ceased and $D$ increased. Klaassen et al. (1998) also found evaporation rates from a forest canopy to fall to lower values during rainfall (0.08 mm $h^{-1}$ on average) and to increase rapidly at the end of an event. This was contrary to Calder and Wright (1986) who found that evaporation of intercepted rainfall was higher during the event than afterwards using gamma ray attenuation measurements to directly monitor canopy water storage. Throughout the measurement period at this site, $\lambda E$ tended to be greater from the wet canopy when rainfall had ceased. Mean $\lambda E \pm 1$ s.d. was 35.1 ± 40.5 W $m^{-2}$ (40.2 ± 41.9 W $m^{-2}$), n = 3667 after rainfall compared with 25.9 ± 27.3 W $m^{-2}$ (49.7 ± 57.5 W $m^{-2}$), n = 2143 during rainfall (with values corrected for signal attenuation in brackets). However, standard deviations overlap such that the difference is not significant. Separating $\lambda E$ for different rainfall intensities did not indicate any significant differences either.

### 4.5.4 Evaporation from a Wet Canopy

Evaporation of intercepted water dominated the winter season evaporative fluxes. Fig. 4.28 and Fig. 4.29 illustrate two days when the canopy was saturated, one where rainfall occurred during the night of November 19, 1998 and one where rainfall occurred during the daytime of December 15, 1997. On November 19, nighttime evaporation was supported by large downward $H$ resulting in $\beta$ of about -3.6 despite almost negligible $D$ (0.005 kPa on average). However, $u_*$ was very high with half hours exceeding 1 m $s^{-1}$ from 0 h to 06:00 h and 18:00 h to 24:00 h. Rainfall also occurred during these hours with rates as high as 5 mm $h^{-1}$. Under very turbulent conditions, high $\lambda E$ was possible on this day with values approaching 70 W $m^{-2}$ despite very small non-zero $D$. Similar patterns were observed throughout the 24-h period on December 15 (Fig. 4.29). Evaporation rates from the saturated canopy were relatively constant from about 10:00 h to 24:00 h with $\lambda E$ as high as 65 W $m^{-2}$ despite rainfall during the daytime. Downward $H$ supported this evaporation as $R_a$ only increased above zero for a total of 6 hours and never exceeded 54 W $m^{-2}$. $\beta$ was about -3.0 for the entire period, daytime $\alpha$ was 4.84 and $\lambda E/R_a$ was 2.09 despite poor energy budget closure. Again, $D$ was quite low, less than 0.03 kPa when positive $\lambda E$ was significant after 06:00 h. Friction velocities were very high after 06:00 h averaging 1.0 m $s^{-1}$.

During the daytime of November 19, energy budget closure was poor. Taking the eddy measurements as recorded, $\lambda E$ was very low as $R_a$ increased and $H$ became almost negligible. This coincided with $u_*$ decreasing to a mean of 0.25 m $s^{-1}$ and $D$ increasing to a maximum of 0.057 kPa. Canopy conductance values were even recorded to be in the range of 0 to 22 mm $s^{-1}$ despite the saturated canopy. However, since the mean delay time $\pm$ 1 s.d. was 46.6 $\pm$ 32.9 samples during this period, it was likely that $\lambda E$ was underestimated with low $u_*$ conditions and flux losses due to signal attenuation such that $g_c$ was also underestimated (see Section 4.3.2). These observations also indicated that $D$ must be only slightly greater than zero and atmospheric conditions must be turbulent for significant evaporation to occur from a wet canopy.

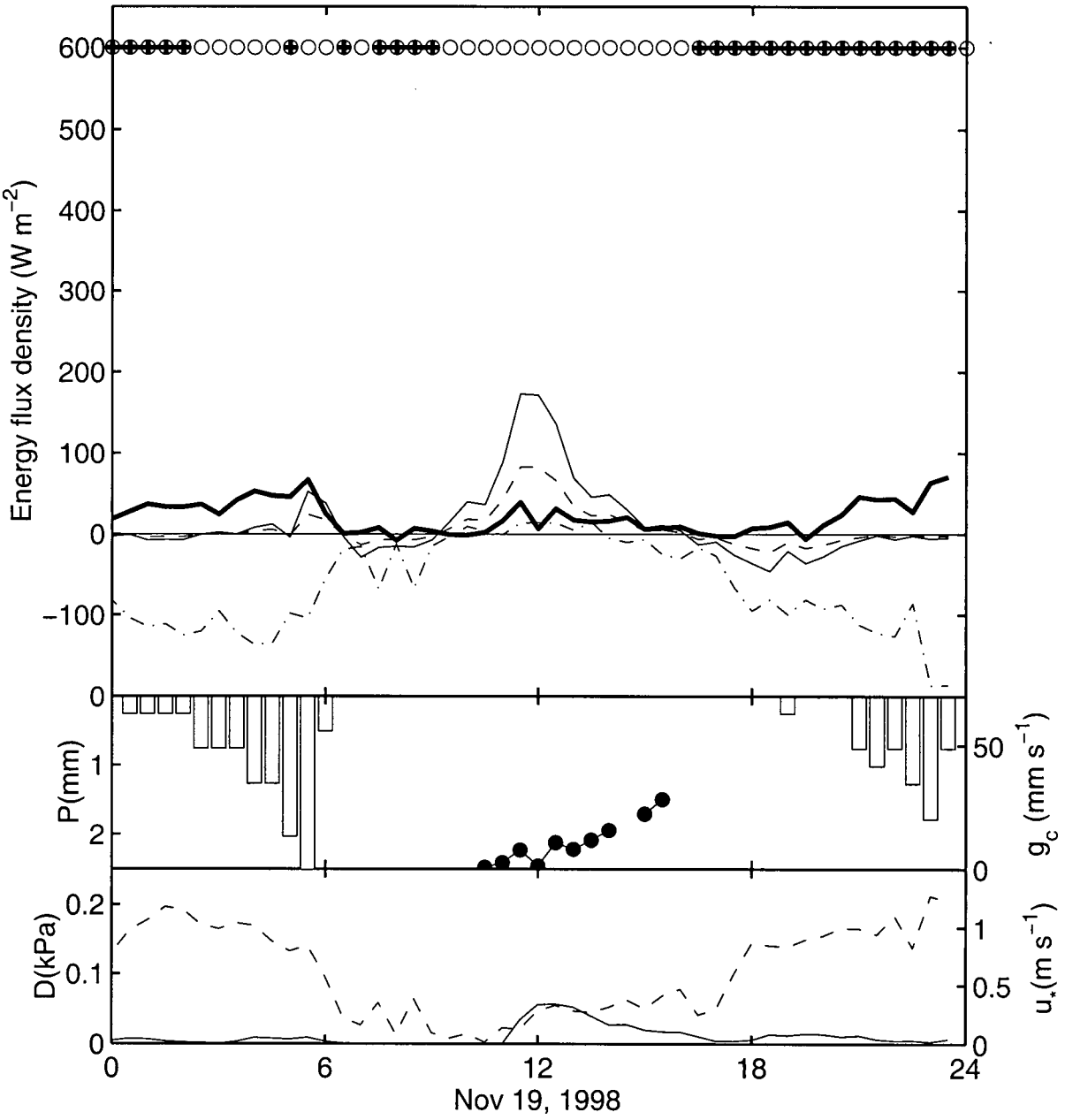


Fig. 4.28 Same as Fig. 4.25 for a wet canopy November 19, 1998. Note the $D$ axis in the bottom panel has been reduced to a maximum of 0.25 kPa and the $g_c$ axis ranges from 0 to 70 mm s$^{-1}$ .

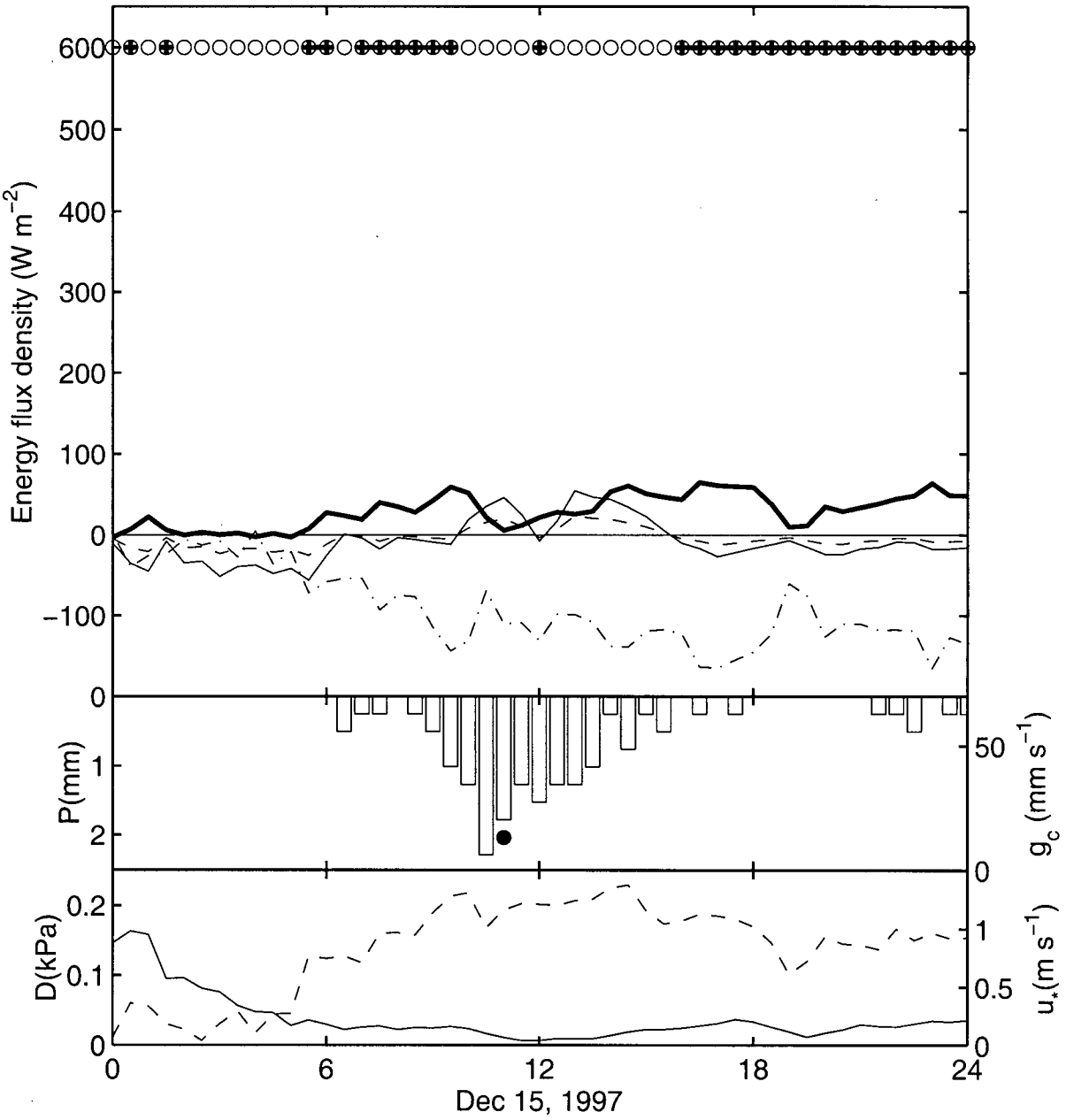


Fig. 4.29 Same as Fig. 4.25 for a wet canopy December 15, 1997. Note the $D$ axis in the bottom panel has been reduced to a maximum of 0.25 kPa and the $g_c$ axis ranges from 0 to 70 mm s$^{-1}$ .

### 4.5.5 Equilibrium Evaporation Rates and Measured $\lambda E$

Results from these five case studies are summarized in Fig. 4.30. Rates of evaporation from the dry canopy were considerably less than equilibrium rates during the daytime as shown for May 29 and September 14 data. Canopy conductance clearly limited $\lambda E$ on these two days. Canopy conductance was more limiting on September 14 than on May 29 as soil moisture was less. Evaporation of intercepted water from the wet or partially wet canopy could approach equilibrium rates and exceed them considerably during both daytime and nighttime conditions. Very large daytime $\lambda E$ was observed on October 17 under somewhat unusually high $R_a$ and $D$ for wet canopy conditions. The winter dates of November 19 and December 15 also illustrated

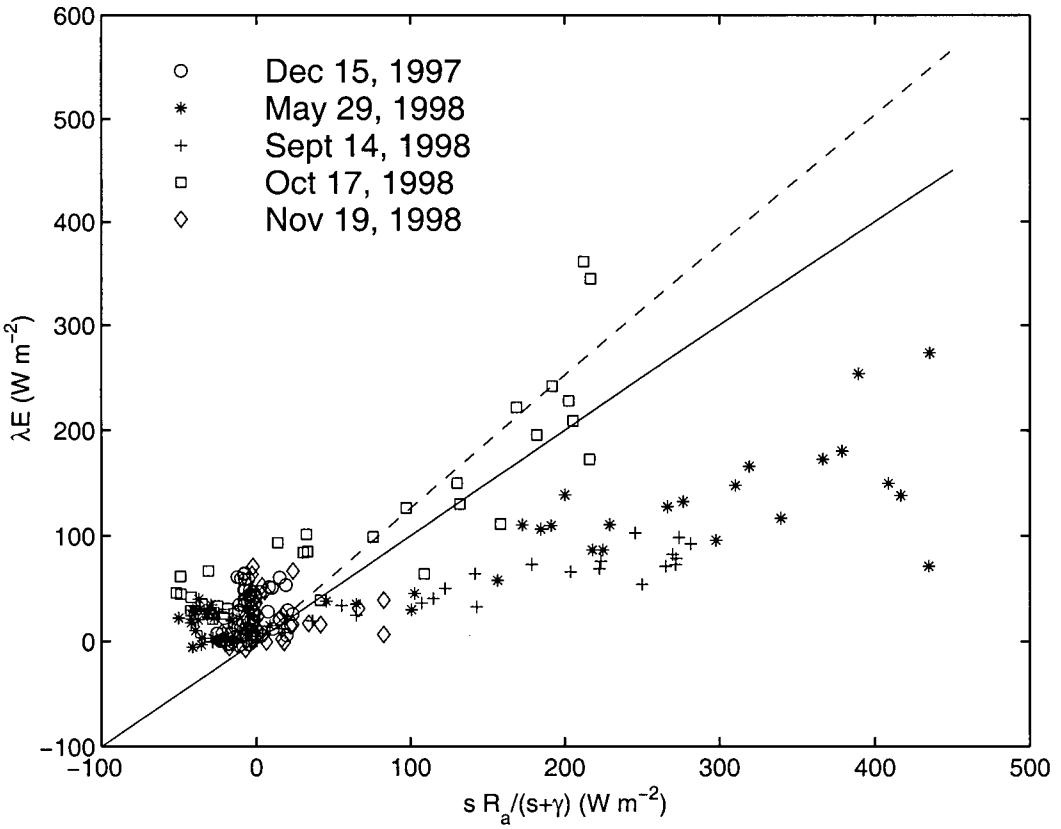


Fig. 4.30 Measured half hourly $\lambda E$ against equilibrium latent heat flux ($\lambda E_{eq} = R_a s/(s+\gamma)$) during the five case studies illustrated in Fig. 4.25 through Fig. 4.29. The solid line indicates the 1:1 line while the dashed line indicates a slope of 1.26 associated with many well-watered surfaces (McNaughton and Spriggs, 1989).

$\lambda E$ greater than $\lambda E_{eq}$ with small but consistently positive $\lambda E$ throughout daytime and nighttime periods more typical of wet canopy conditions with low $R_a$ and $D$.

### 4.5.6 Mechanisms to Support High Rates of Evaporation of Intercepted Water

The occurrence of high daytime $\lambda E$ exceeding $\lambda E_{eq}$ or $R_a$ and high nighttime $\lambda E$ in the absence of radiative energy supports the hypothesis that a wet forest canopy may act as a sink for sensible heat extracted from the air observed as a downward flux of sensible heat from the atmosphere (Rutter, 1967). Evaporation of intercepted water, supported by negative $H$, occurred regularly throughout the winter and after isolated rainfall events throughout the summer at this site (see Fig. 4.18). This has also been illustrated numerous times on shorter time scales by other studies measuring $\lambda E$ and $H$ above forests using indirect techniques such as the Bowen ratio/energy balance method (Stewart, 1977), the eddy covariance/energy balance method (Mizutani et al., 1997) and interception techniques (Pearce and Rowe, 1980; Shuttleworth and Calder, 1979).

These high rates of evaporation were possible from this wet forest canopy due to the high aerodynamic roughness of the surface. Equation (2.5) describes the micrometeorolgical variables driving evaporation and the limitation exerted by physiological control through $g_c$. Therefore, as $g_c$ approaches infinity for a wet surface, $\lambda E$ approaches $\lambda E_{eq}$ while significantly large $g_a$ will increase the additional importance of the convective term (the last term) in Equation (2.6). In order for $\lambda E$ to exceed $\lambda E_{eq}$, $D$ must be maintained above zero over the evaporating surface as evaporated water humidifies the air above the canopy and into the mixed layer of the planetary boundary layer (McNaughton and Jarvis, 1983). One possible mechanism is by advection of dry air from local sources (edge effects) (Oke, 1987) or large-scale sources where both situations require a horizontal gradient in $D$ (Singh and Szeicz, 1979; Stewart, 1977; Thom and Oliver, 1977). Non-advective sources include heat supplied directly from the air above the canopy and/or from the forest biomass (McNaughton and Jarvis, 1983; Moore, 1976).

As this forest is quite extensive, edge effects are unlikely (see the site Map in Fig. 3.1). Support for large-scale advection as described by Shuttleworth and Calder (1979) appeals to the common weather patterns associated with rainfall in the uplands of the UK. Here cold-front activity associated with rainfall tends to be followed by large drier air masses which would not likely become humidified passing over forests on the order of 10 km. However, weather patterns

over coastal southern British Columbia during the winter are characterized by cyclonic disturbances which pass through at a rate of approximately one per week (Oke and Hay, 1994). As a result, general cyclonic uplift associated with low pressure systems results in widespread stratiform cloud and chances of rainfall extending over the order of tens to thousands of square kilometers (Oke and Hay, 1994). This type of weather would likely discount the possibility of large, sustainable $\lambda E$ supported by advection of dry air from moving air masses (Shuttleworth and Calder, 1979). In addition, advection from neighboring areas in situations of isolated showers (Singh and Szeicz, 1979) or from neighboring lowland areas when orographic uplift results in rainfall over hilly or mountainous terrain (McNaughton and Jarvis, 1983) would be unlikely. However, the influence of possible synoptic scale (>$10^3$ km) advection of unsaturated air originating outside of the influence of the cyclonic disturbances passing over Vancouver Island during the winter cannot be completely discounted.

An unsaturated atmosphere could also be maintained by non-advective mechanisms. Vertical mixing of the air column beneath the cloud base could be a possible supply of heat as descending air warms adiabatically (McNaughton and Jarvis, 1983). Another mechanism could involve adiabatically warming air as it descends a slope, losing sensible heat and gaining latent heat on the way down (McNaughton and Jarvis, 1983). As this Douglas-fir site is on a 5 to 10° slope with regular katabatic and anabatic wind flows, this may explain the significant nighttime fluxes observed throughout the early summer season. McNaughton and Jarvis (1983) illustrated how 1 $m^3$ of air descending a slope with $u$ = 1 m $s^{-1}$ could maintain a constant $D$ if sensible heat was replaced by latent heat at approximately 8 W $m^{-2}$ (with $\gamma/s$ = 0.5 at 20 °C). Depending on the depth of the descending air mass, this could account for considerable $\lambda E$. Support for this hypothesis was found during the October 17 case study. On this day, $\lambda E$ was rather insignificant until 06:00 h despite a relatively constant $u$ of 3 m $s^{-1}$. However, the wind direction abruptly switched from about 120° (ESE, upslope winds) to about 240° to 320° (W, downslope winds) where it remained for the rest of the day accompanied by high $\lambda E$.

However, during the winter, upslope-downslope patterns were not evident as the land-sea and valley-mountain temperature gradients were minimized. Winds tended to come from the ESE and SSW, at about 120° and 220°, reflecting the general movement of low pressure systems from the west accompanied by counter-clockwise windflow heading towards the low pressure center. As a result, downslope winds were not associated with higher $\lambda E$ for November 19 or December 17 where higher $\lambda E$ was associated with winds coming from about 120°. Significant

$\lambda E$ on these particular days was associated with very small non-zero $D$ and stronger wind speeds of about 4 to 5 m $s^{-1}$.

## 4.6 CANOPY CONDUCTANCE

Seasonal and diurnal patterns of $\lambda E$ from the forest canopy throughout the dry, summer season gave clear evidence for the role of physiological control in limiting rates of $\lambda E$ below potential or equilibrium rates. Evaporation from the dry canopy is primarily through the process of transpiration. Transpiration rates from aerodynamically rough forests depend mainly upon $D$ and $g_c$ (Equation (2.5)). Canopy conductance essentially treats the canopy as a "big leaf" and represents the aggregate role of individual stomata controlling water loss from the Douglas-fir needles. Therefore, the low $\alpha$ or $\lambda E/R_a$ values and high $\beta$ values observed throughout the summer months indicated that transpiration rates from the Douglas-fir canopy were limited by stomatal control.

The variation in $g_s$ and $g_c$ from Douglas-fir canopies has mainly been attributed to effects of $D$ and $\Psi_{soil}$ (Tan and Black, 1976). Irradiance has been shown to be an important additional factor for various coniferous species (e.g. Kelliher et al., 1993). A recent proposal by Monteith (1995b) has suggested that a mechanistic response to $E$ rather than $D$, based on the work by Mott and Parkhurst (1991), could be scaled up to predict the behaviour of $g_c$. These relationships and their underlying mechanisms are explored in the following section in order to further describe the controls over evaporation from this stand.

### 4.6.1 Variations in $g_c$ through the Summer

Fig. 4.31 illustrates the variations in daily mean $g_c$ between May 1 and September 1, 1998 along with associated environmental variables: photosynthetic photon flux density ($Q$), $D$, $T$, and $\Psi_{soil}$. Values associated with dry, daytime conditions only are shown. Daily mean $g_c$ was calculated by weighting the half hourly $g_c$ with $D$ as follows (Tan and Black, 1976),

$$\text{Mean } g_c = \sum_{i=1}^{n} D_i g_{c_i} \Big/ \sum_{i=1}^{n} D_i \qquad (4.8)$$

where $D_i$ and $g_{ci}$ are the values of $D$ and $g_c$ for the $i$th half hour of the $n$ daylight ($S\downarrow > 0$ W m$^{-2}$) half hours of each day.

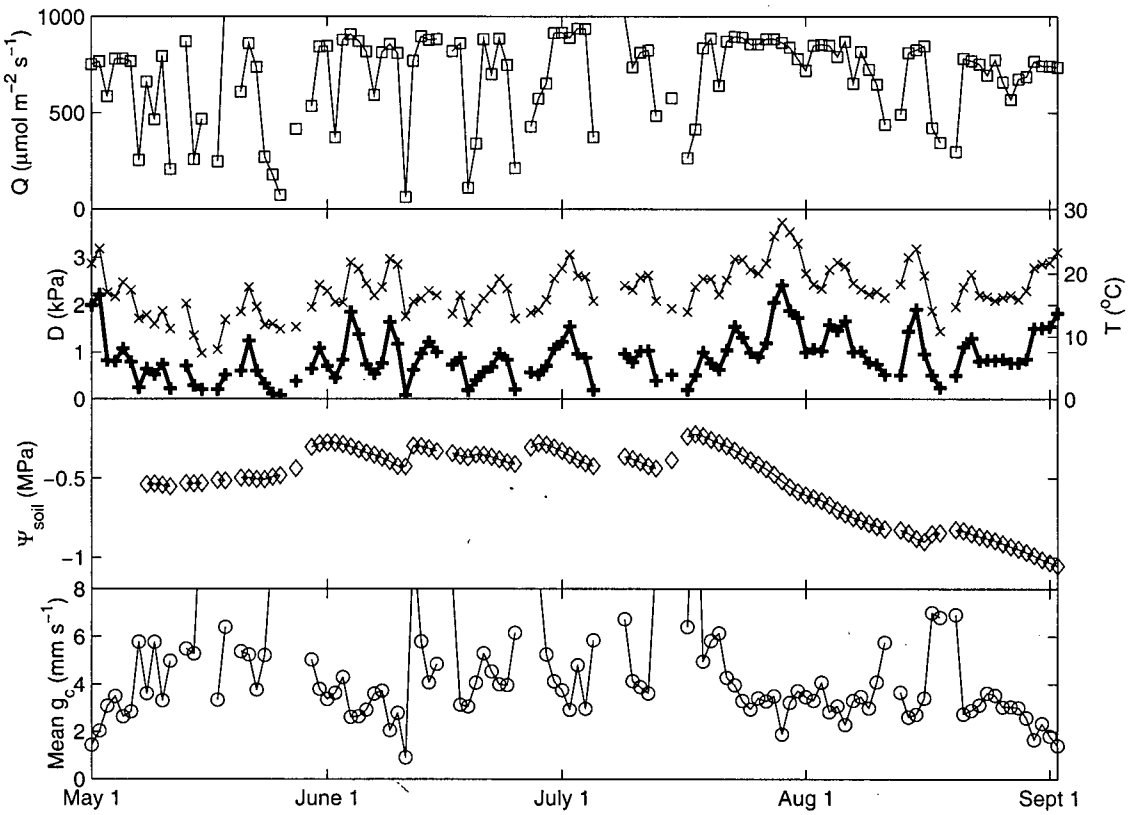


Fig. 4.31 Daily mean photosynthetic photon flux density, $Q$ (□), air temperature $T$ (×), saturation deficit, $D$ (+), soil water potential, $\Psi_{soil}$ (◊), and mean weighted canopy conductance, $g_c$ (○) for daytime, dry canopy conditions between May 1, 1998 and September 1, 1998.

Throughout this period, mean daily $g_c$ ranged from 1 mm s$^{-1}$ to 6 mm s$^{-1}$ with peak values of 20 mm s$^{-1}$ occurring with low $Q$, $T$, and $D$ characteristic of overcast conditions around rainfall events. In general, there appeared to be a decreasing trend in $g_c$ as the summer progressed. The most noticeable correlation between $g_c$ and these environmental variables was with $\Psi_{soil}$. In particular, dry down periods between rainfall events (indicated as missing data in Fig. 4.31) such as during the 13 days beginning May 29, were characterized by decreasing $\Psi_{soil}$ and decreasing mean $g_c$.

### 4.6.2 Canopy Conductance Functional Forms

To describe how $g_c$ varies with $Q$, $D$, and $\Psi_{soil}$, functional forms were fitted to $g_c$ for the period between May 1, 1998 and September 1, 1998. Rather than using the boundary-line approach on large amounts of data, $g_c$ was binned according to the independent variable in question (Jarvis, 1976). Empirical relationships using common functions described in the literature (e.g. Jarvis, 1976; Lhomme, 1998) were found using mean $g_c$ in order to simply describe how $g_c$ varied with these environmental factors rather than attempt to model $g_c$ behaviour. Results are shown in Table 4.5.

The influence of $Q$ was expressed as a rectangular hyperbolic function originally used with global solar radiation of the form (Stewart, 1988),

$$g_c = \frac{bQ}{a+Q} \tag{4.9}$$

where $a$ and $b$ are empirical coefficients. As $Q$ increased, $g_c$ increased until a saturating point was reached and further increases in $Q$ had little effect on $g_c$ (Fig. 4.32). Despite the very large scatter for unbinned data (as indicated by the large standard deviation about the means in Fig. 4.32), this non-linear relationship determined using an optimization algorithm fit the binned data well with an $R^2 = 0.77$. The resultant saturating $Q$ was equal to about 470 μmol $m^2$ $s^{-1}$ when $g_c$ attained 90% of the fitted maximum (i.e. $b$) of 2.4 mm $s^{-1}$. Tan et al. (1977) found Douglas-fir stomatal closure to generally begin at lower $Q$ levels around 300 μmol $m^{-2}$ $s^{-1}$. *Pinus radiata* stomata were also found to respond very rapidly with $g_c$ reaching 90% of the maximum value at only 10% full sunlight (Kelliher et al., 1993). The underlying mechanism regarding the relationship between $g_c$ and $Q$ as well as $T$ and $CO_2$ concentration (latter two not shown) are based on carbon assimilation processes through photosynthesis and the exchange of $CO_2$ through the stomata. Thus, at light levels limiting to photosynthesis, $g_c$ was expected to be low.

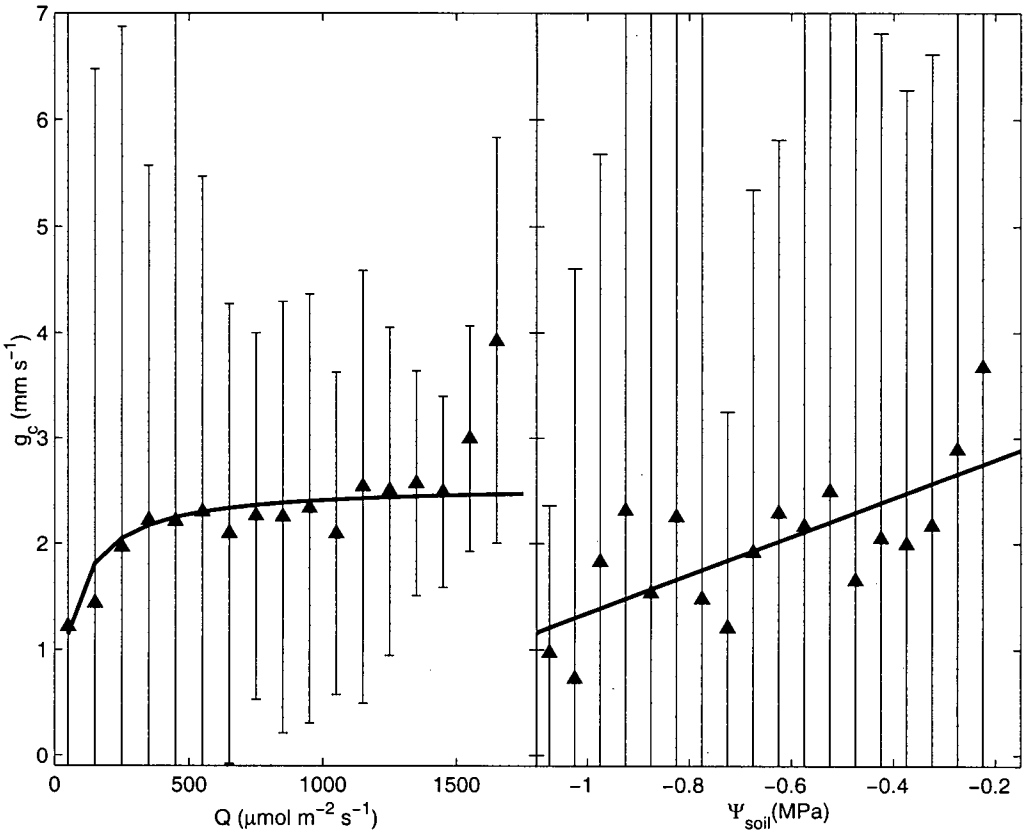


Fig. 4.32 The left panel shows the general relationship between mean canopy conductance ($g_c$) ± 1 s.d. and photosynthetic photon flux density ($Q$) with $g_c$ binned at 100 μmol m$^{-2}$ s$^{-1}$ intervals (▲). The non-linear relationship $g_c = \frac{bQ}{a+Q}$ was fitted with an optimization algorithm. The right panel shows the general relationship between mean $g_c$ ± 1 s.d. and $\Psi_{soil}$ with $g_c$ binned at 0.05 MPa intervals. The relationship $g_c = a + b\Psi_{soil}$ was fitted with least squares linear regression. Results are shown in Table 4.5.

Soil water potential was related to $g_c$ using a simple linear relationship based on a hyperbolic relationship used for canopy resistance (e.g. Lhomme, 1998),

$$g_c = a + b\Psi_{soil} \qquad (4.10)$$

where $a$ and $b$ are empirical coefficients, unrelated to those of Equation (4.9). As soil water became more limiting, $g_c$ tended to decrease with a large degree of scatter for unbinned data within the $\Psi_{soil}$ range, -0.2 to -1.3 MPa, observed throughout the summer. The decrease was more systematic for binned data with an $R^2$ = 0.49 (Fig. 4.32). When $\Psi_{soil}$ was 0, the fitted maximum $g_c$ (i.e. $a$) was found to be 3.16 mm s$^{-1}$, while $\Psi_{soil}$ at which complete stomatal closure

would occur was equal to -1.74 MPa. Again, as the other variables influencing mean $g_c$ were not accounted for, this maximum $g_c$ and limiting $\Psi_{soil}$ were strictly descriptive rather than predictive. Of particular note was the tendency for $g_c$ to decrease significantly at a potential of about -0.2 to -0.25 MPa (Fig. 4.32). This was the same critical $\Psi_{soil}$ found for a younger Douglas-fir stand located within 20 km of this study site on Vancouver Island with a similar gravelly sandy loam soil (Tan and Black, 1976).

Canopy conductance was observed to decrease with increasing $D$ computed using RH and $T$ measured within the canopy at 27 m. As $g_a$ was high above this forest, $D$ at the leaf surface was likely well approximated by $D$ of the air. A decreasing hyperbolic function,

$$g_c = \frac{a}{1+bD} \tag{4.11}$$

was fit using linear regression (for the reciprocal of both $g_c$ and the $D$ term) while attempting to maintain $Q$ and $\Psi_{soil}$ constant through stratification assuming that temperature effects were accounted for in $D$, while $CO_2$ concentration and time were assumed to have small effects (Fig. 4.33).

In general, Equation (4.11) described the relationship between $g_c$ and $D$ adequately with the relationship maintained as $Q$ decreased through all three ranges and for the two least negative $\Psi_{soil}$ ranges (Table 4.5). Three ranges of $Q$ were used varying from low, possibly limiting light levels (200 to 400 μmol $m^{-2}$ $s^{-1}$), saturating levels (400 to 800 μmol $m^{-2}$ $s^{-1}$), and high levels (800 to 1800 μmol $m^{-2}$ $s^{-1}$). At high $D$, $g_c$ was observed to increase with increasing $Q$, while at low $D$, $g_c$ tended to decrease somewhat with increasing $Q$ levels. Maximum $g_c$ was 20.4 mm $s^{-1}$ or 5.1 mm $s^{-1}$, on a LAI basis, with the lowest $Q$ range, indicating that this range was not likely limiting $g_c$. A similar result was found for aspen $g_c$ with a maximum $g_c$ of 21 mm $s^{-1}$ or 9.1 mm $s^{-1}$, on a LAI basis, obtained with a mid-range $Q$ between 800 and 1400 μmol $m^{-2}$ $s^{-1}$ (Blanken, 1997). Maximum $g_c$ for younger Douglas-fir stands have been found ranging from 16 mm $s^{-1}$ (LAI = 5) (Price and Black, 1990) to 17 mm $s^{-1}$ (McNaughton and Black, 1973). Maximum $g_c$ at high light levels was only 4.39 mm $s^{-1}$ for this stand, while maximum $g_c$ was 8.77 mm $s^{-1}$ at mid light levels. When a lower light range was set to vary from 25 to 200 μmol $m^{-2}$ $s^{-1}$ (not shown), maximum $g_c$ was 3.08 mm $s^{-1}$ associated with a large degree of scatter and low $R^2$ = 0.10. It appeared that light did not limit $g_c$ until $Q$ decreased well below 200 μmol $m^2$ $s^{-1}$.

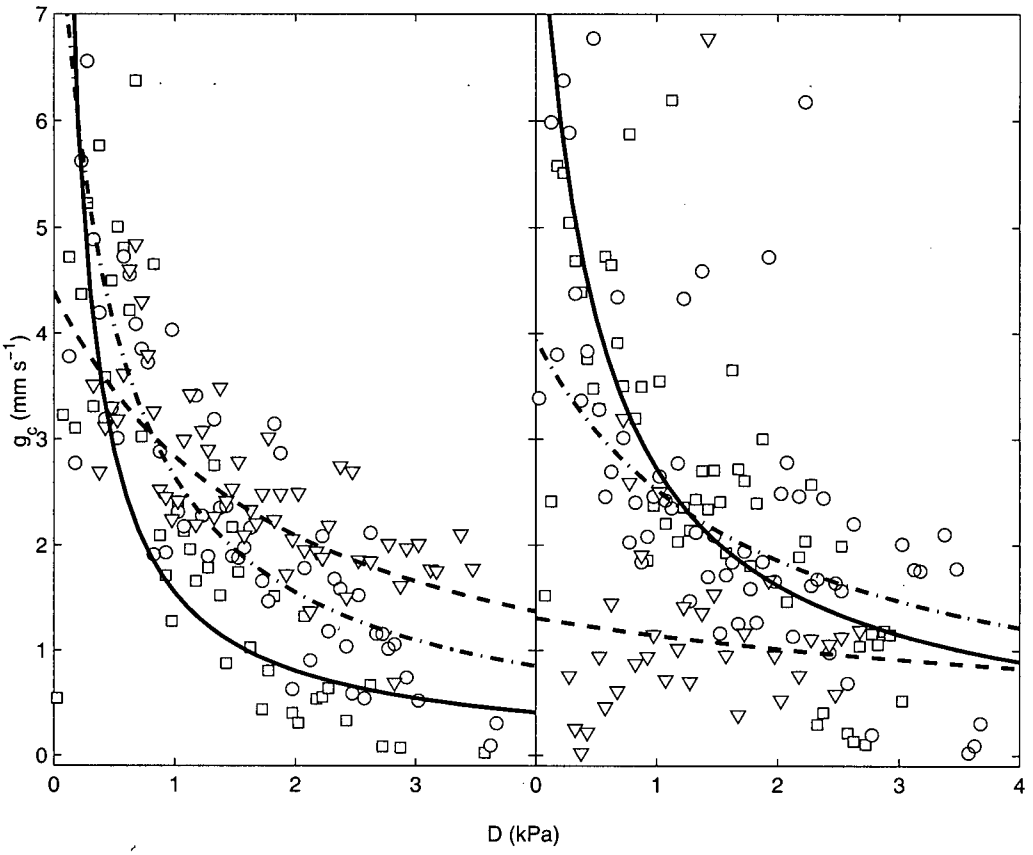


Fig. 4.33 Relationship between atmospheric saturation deficit at canopy height ($D$) and mean canopy conductance ($g_c$) binned at 0.05 kPa intervals stratified by photosynthetic photon flux density ($Q$); 200 - 400 μmol m$^{-2}$ s$^{-1}$ (□, solid line), 400 - 800 μmol m$^{-2}$ s$^{-1}$ (○, dash-dotted line), and > 800 μmol m$^{-2}$ s$^{-1}$ (▽, dashed line)(left panel). Relationships are in the form, $g_c = \frac{a}{1+bD}$ with coefficients $a$ and $b$ fitted with least squares linear regression for the reciprocal of $g_c$ and the $D$ term. The right panel shows the same relationships with $g_c$ stratified by soil water potential; 0 to -0.5 MPa (□, solid line), -0.5 to -1 MPa (○, dash-dotted line), and < -1 MPa (▽, dashed line). Results are shown in Table 4.5.

Canopy conductance was stratified by $\Psi_{soil}$ in three ranges from adequate soil moisture (0 to -0.5 MPa), slightly limiting (-0.5 to -1 MPa) and strongly limiting soil moisture (-1 to -1.3 MPa). As expected, maximum $g_c$ decreased as $\Psi_{soil}$ became more negative. At the most limiting $\Psi_{soil}$ range, the relationship between $g_c$ and $D$ was not maintained ($R^2 = 0.03$). Canopy conductance remained low despite decreasing $D$. This suggested the trees were under significant drought stress within this range such that measured $\lambda E$ from the canopy was greatly limited by $g_c$. Again, there was considerable scatter as the effects of other variables were unaccounted for.

Table 4.5 Relationships between canopy conductance ($g_c$) and photosynthetic photon flux density ($Q$), $g_c$ and soil water potential ($\Psi_{soil}$), $g_c$ and saturation deficit ($D$) stratified by $Q$ and by $\Psi_{soil}$. The first relationship was found using a numerical optimization procedure, the second relationship was determined using least squares linear regression. The last two relationships were fit using linear regression of the reciprocal of Equation (4.11) as $1/g_c = 1/a + (b/a)D$. Values of $g_c$ were limited to those above a certain value as listed in column three.

| Relationships | Bin intervals & Stratifying variable | Limit $g_c >$ (mm $s^{-1}$) | $a$ | $b$ | $R^2$ |
|---|---|---|---|---|---|
| $g_c$ and $Q$: $g_c = \frac{bQ}{a+Q}$ | $Q$: 100 µmol $m^{-2}$ $s^{-1}$ | 0 | 51.34 | 2.38 | 0.77 |
| $g_c$ and $\Psi_{soil}$: $g_c = a + b\Psi_{soil}$ | $\Psi_{soil}$: 0.05 MPa | 0 | 3.16 | 1.82 | 0.49 |
| $g_c$ and $D$: $g_c = \frac{a}{1+bD}$ | $D$: 0.05 kPa<br>$Q$: 200 to 400 µmol $m^{-2}$ $s^{-1}$ | 0.4 | 20.43 | 12.21 | 0.42 |
| | $D$: 0.05 kPa<br>$Q$: 400 to 800 µmol $m^{-2}$ $s^{-1}$ | 0.66 | 8.77 | 2.33 | 0.66 |
| | $D$: 0.05 kPa<br>$Q$: 800 to 1800 µmol $m^{-2}$ $s^{-1}$ | 0 | 4.39 | 0.55 | 0.36 |
| $g_c$ and $D$: $g_c = \frac{a}{1+bD}$ | $D$: 0.05 kPa<br>$\Psi_{soil}$: 0 to -0.5 MPa | 0.5 | 8.62 | 2.17 | 0.51 |
| | $D$: 0.05 kPa<br>$\Psi_{soil}$: -0.5 to -1 MPa | 0.5 | 3.93 | 0.56 | 0.30 |
| | $D$: 0.05 kPa<br>$\Psi_{soil}$: -1 to -1.3 MPa | 0.5 | 1.31 | 0.14 | 0.03 |

Originally attributed to Lohammar et al. (1980), the relationship between $g_c$ and $D$ in the form of Equation (4.11) has been applied successfully for other tree species such as *Eucalyptus grandis* (Leuning, 1995) and for *Macademia integrifolia* leaves (Lloyd, 1991). Others have used decreasing exponential functions (Blanken et al., 1997) and decreasing linear functions (Jarvis, 1976). The decreasing hyperbolic form describes a negative feedback response to increasing $D$. This formulation results in a saturation-type curve for rates of evaporation ($E$) plotted against $D$ (see Fig. 4.35). The associated mechanism is based on stomatal control through the water

relations of the leaf. For example, an increase in $D$ results in an increase in $E$ lowering the leaf water potential and decreasing stomatal aperture, thereby lowering $E$ to result in an asymptotic maximum rate for $E$. The linear form describes a feedforward response to $D$ characterized by the suppression of $E$ in dry air despite improving total leaf water potential (Schulze et al., 1972). Some of the suggested mechanisms for the feedforward response include peristomatal transpiration, patchy stomatal closure and hormonal influences (Cowan, 1994; Farquhar, 1978; Franks et al., 1997; Mott et al., 1993). The negative feedback response is by far the more common response reported in the literature for either herbaceous or woody species (Franks et al., 1997; Monteith, 1995b) and appeared to adequately describe the results from this Douglas-fir stand (Fig. 3.1 and Fig. 3.2). The decreasing linear relationship, $g_c = a - bD$, stratified by $Q$ and by $\Psi_{soil}$ slightly improved the fit between $g_c$ and $D$ for only the high $Q$ range as indicated by a slightly larger $R^2$ of 0.53. However, Tan et al. (1978) found results supporting the feedforward response pattern in a Douglas-fir stand when $D$ exceeded 1.0 to 1.5 kPa regardless of soil moisture stress. In that study, $\lambda E$ may have been underestimated at high $D$ and large $\beta$ values due to the difficulty in accurately measuring very small vapour pressure gradients observed above the canopy under these types of conditions (Black, pers. comm. 1999).

### 4.6.3 Monteith's Formulation of $g_c$

Despite the strong correlation found between $g_c$ and $D$ for forests and grasslands alike (e.g. Kelliher et al., 1993), a direct plant mechanism or structure for sensing $D$ has never been identified (Mott and Parkhurst, 1991; Sheriff, 1984). In fact, Mott and Parkhurst (1991) provided experimental evidence to show that stomatal aperture and $g_s$ responded to $E$ rather than $D$ in *Vicia faba* leaves. The $g_c$ response to $D$ expressed as a decreasing hyperbolic function (Equation (4.11)) supports a direct relationship between $E$ and $g_c$ when $D$ can be assumed to be equivalent to $E/g_c$ (Dewar, 1995; Leuning, 1995; Monteith, 1995b) which is a good approximation for aerodynamically rough forests. Originally stated for stomatal conductance, the linear decreasing relationship between $g_c$ and $E$ may be expressed as (Monteith, 1995b),

$$g_c = E / D = a(1 - bE) \qquad (4.12)$$

where $a$ and $b$ are empirical coefficients. Here, $a = g_m$, where $g_m$ is an extrapolated maximum conductance and $b = 1/E_m$, where $E_m$ is an extrapolated maximum evaporation rate. Equation

(4.12) may be restated as Equation (2.9), now formulated for $g_c$ as $\frac{g_c}{g_m} = 1 - \frac{E}{E_m}$. This relationship is known as Monteith's formulation of stomatal conductance (Monteith, 1995b). To avoid regressing dependent variables (i.e. *E/D* against *E*), Equation (4.12) was reformulated as (Monteith, 1995b),

$$1/E = 1/aD + b \qquad (4.13).$$

Equation (4.11) expressed as $g_c = \frac{a}{1+abD}$ can be obtained using $g_c = a(1-bE)$ of Equation (4.12) and $E = Dg_c$. Note that the coefficients *a* and *b* are consistent for this version of Equation (4.11) and Equations (4.12) and (4.13).

Scaling these relationships up to the canopy level has been undertaken theoretically by Lhomme (1998) and experimentally by Pataki et al. (1998), for example. Despite the implication of a linear decrease in $g_c$ with increasing *E* by the good fit of Equation (4.11) (see Fig. 4.33) and the tendency for 1/*E* to increase with 1/*D* (not shown), plots of $g_c$ against *E* did not clearly support this (not shown). In fact, there was a clear tendency for $g_c$ to be positively linearly related to *E* indicative of a feedforward response where $g_c$ decreases with decreasing *E*. This has also been found by other field researchers (Meinzer et al., 1997; Pataki et al., 1998) but does not immediately discount the hypothesis that $g_c$ responds to *E*. These results may simply be associated with field measurements where several unaccounted environmental variables covary with *D* such as *Q*, *T*, and time associated with circadian rhythms. As stated earlier, these may be important to plant stomatal responses and in the case of light and temperature, do have a mechanistic physiological basis for controlling $g_c$ through carbon assimilation processes. In contrast, Monteith's (1995b) analysis of 52 data sets was limited to measurements collected through gas exchange experiments in laboratory settings where most variables other than *D* could be held constant.

On a diurnal basis, $g_c$ could be seen to decrease with increasing $\lambda E$ for only a few hours prior to maximum $\lambda E$ on selected days. Similarly, measurements of $\lambda E$ and $g_c$ from tree saplings using sap flow and closed top gas-exchange chambers had to be restricted to the hours between 10:00 h and 14:00 h as hysteresis in 1/*E* vs 1/*D* plots was observed with declining *D* (Pataki et al., 1998). Two dry summer days, June 20 and 21, 1998 were selected to illustrate these findings. Canopy conductance for our stand was observed to generally peak quickly in the morning, commonly before 10:00 h, decrease rapidly until about 12:00 h and then decrease slowly throughout the rest of the day (Fig. 4.34). Latent heat flux tended to peak later after

12:00 h (Fig. 4.34). This diurnal $g_c$ pattern is quite common for stands of Douglas-fir and other coniferous species (Lindroth, 1985; McNaughton and Black, 1973; Price and Black, 1990; Tan et al., 1977).

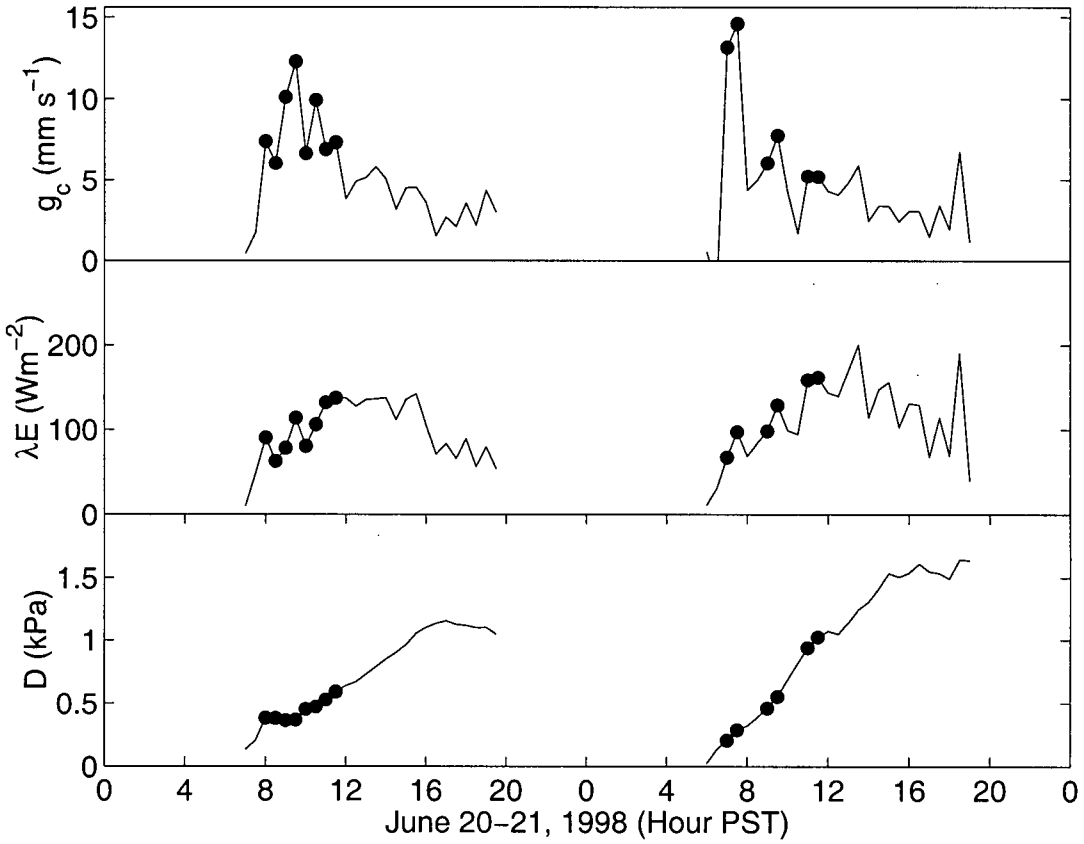


Fig. 4.34 Canopy conductance ($g_c$), latent heat flux ($\lambda E$) corresponding to stand transpiration rates and vapour pressure deficit ($D$) on a half hourly basis for June 20 and 21, 1998. Circles indicate the time intervals when $\lambda E$ was observed to increase with decreasing $g_c$.

Monteith's (1995b) analysis was then applied to these selected half hour values. The results are shown in Fig. 4.35 and Table 4.6. Using a boundary-line approach, the relationships were fitted to the values associated with maximum $g_c$ within each $D$ interval (width = 0.1 kPa). The decreasing hyperbolic relationship of Equation (4.11) was found to describe the relationship between $g_c$ and $D$ (fit using the reciprocal of both $g_c$ and the $D$ term, $R^2$ = 0.98, n = 6). In addition, an increasing hyperbolic relationship between $D$ and $E$ was found to describe these measurements fairly well, while a linear relationship between $g_c$ and $E$ using Equation (4.12) was

good for the boundary values of $g_c$ but less clear for the rest (Table 4.6, Fig. 4.35). These relationships describe both a negative feedback response pattern for $g_c$ and support the hypothesis that $g_c$ responds directly to $E$ rather than $D$ (Monteith, 1995b).

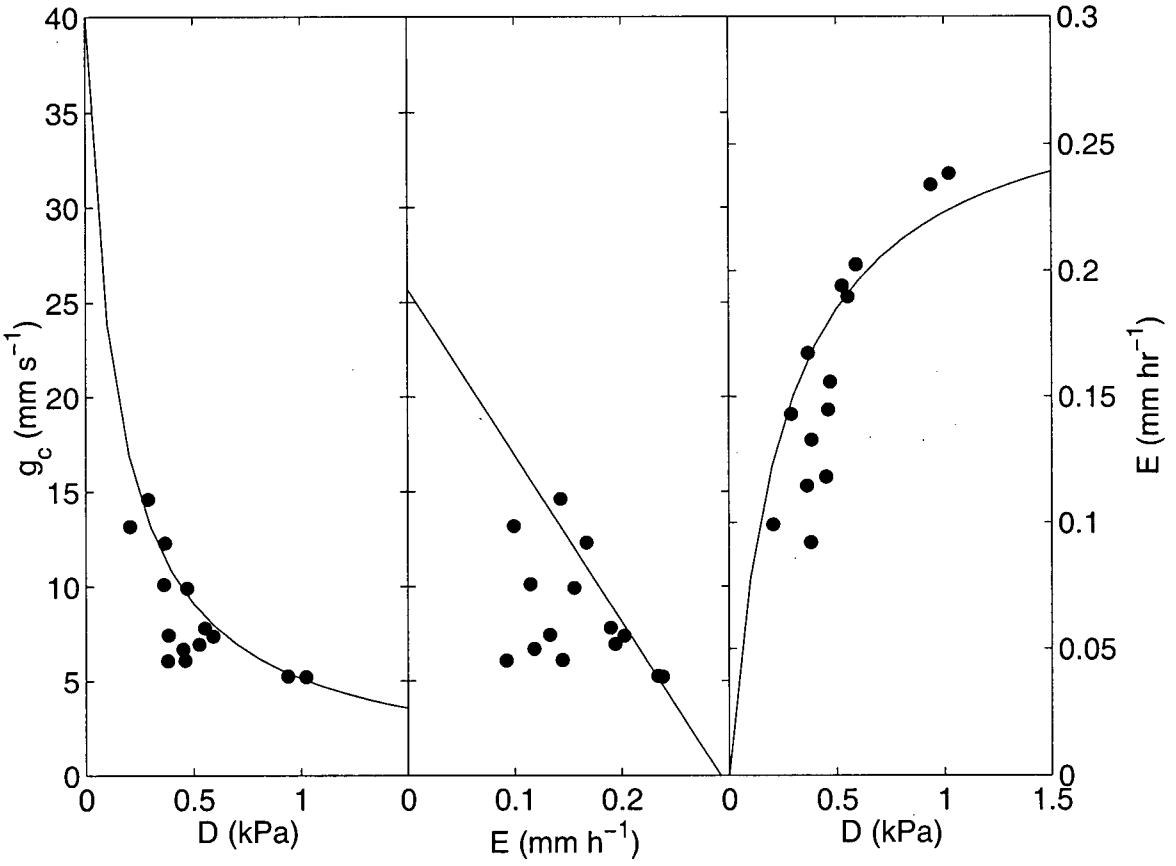


Fig. 4.35 Relationships between $g_c$ and $D$ (left), $g_c$ and $E$ (center) and $E$ and $D$ (right) for selected half hour measurements (Fig. 4.34) on June 20 and 21, 1998. Relationships were fit for the following functions: $1/g_c = 1/a + bD$ (the reciprocal of $g_c = a/(1+abD)$), $g_c = a(1-bE)$ and $1/E = 1/aD + b$ (the reciprocal of $E = aD/(1+abD)$). A 'boundary-line' approach was used with linear regressions performed on the 6 values of $E$ corresponding to the maximum $g_c$ for each $D$ interval of 0.1 kPa. Results are shown in Table 4.6.

The parameter, $g_m$ for Monteith's (1995b) formulation of $g_c$ (Equation (2.9)) derived from the plots of $1/E$ against $1/D$ was 39.60 mm s$^{-1}$ for the June 20 and 21, 1998 data while $E_m$ was 0.28 mm h$^{-1}$. The maximum $g_c$ was extremely high for a Douglas-fir stand while $E_m$ was low (Kelliher et al., 1993). Maximum conductance for conifers during the growing season are typically 23.5 ± 7.5 mm s$^{-1}$ (Kelliher et al., 1995). Placing these results in context, June 20 and 21, 1998 were clear, warm sunny days with maximum $Q$ of 1484 and 1493 μmol m$^{-2}$ s$^{-1}$,

maximum temperatures of 21.5 and 24.2 °C, and average $D$ of 0.46 and 0.79 kPa peaking at 1.1 and 1.6 kPa in the late afternoon. This period wasn't associated with very much soil moisture stress with $\theta_v$ about 24% and $\Psi_{soil}$ around -0.37 MPa. However, as mentioned above, $g_c$ appeared to decrease significantly at a water potential of around -0.25 MPa such that the trees may have been water limited and experiencing some degree of drought stress.

There was a large degree of scatter and an imprecise decreasing linear relationship between $g_c$ and $E$ (center panel in Fig. 4.35) while the hyperbolic function relating $g_c$ to $D$ appeared more successful (left panel in Fig. 4.35). As these two relationships are simple manipulations of one another using the approximation $g_c = E/D$, this approximation appears to be somewhat imperfect for canopy-based measurements. This would make reformulating the hyperbolic function based on $D$ to a linear one based on $E$ prone to errors. More importantly, the large scatter associated with Monteith's relationship emphasized the importance of the influence of other associated environmental variables, most likely covariables of $D$ such as $T$ and $Q$ including the effects of time through rhythmic plant behaviour, in determining canopy $E$ (Meinzer et al., 1997).

Table 4.6 Relationships between canopy conductance ($g_c$) and saturation deficit ($D$) for June 20 and 21, 1998. Data is shown in Fig. 4.35. The parameters $g_m$ and $E_m$ for Monteith's (1995b) formulation of $g_c$, $\frac{g_c}{g_m} = 1 - \frac{E}{E_m}$ ,Equation (2.9) are shown derived from the relationships. Only the last set of $g_m$ and $E_m$ are statistically valid (Monteith, 1995b). Also note that the first relationship was fit with a linear regression on the reciprocal of independent and dependent variables (i.e. $1/g_c = 1/a + bD$)

| Relationships | a | b | $R^2$ | n | $g_m$ (mm $s^{-1}$) | $E_m$ (mm $h^{-1}$) |
|---|---|---|---|---|---|---|
| $g_c = \frac{a}{1+abD}$ | 40.31 mm $s^{-1}$ | 0.17 s $mm^{-1}$/kPa | 0.98 | 6 | 40.31 | 0.39 |
| $g_c = a(1-bE)$ | 25.70 mm $s^{-1}$ | 3.42 $mm^{-1}$ h | 0.86 | 6 | 25.70 | 0.29 |
| $1/E = 1/aD + b$ | 1.085 mm $h^{-1}$/kPa | 3.57 $mm^{-1}$ h | 0.85 | 6 | 39.60 | 0.28 |

The parameters $g_m$ and $E_m$ have been interpreted in the literature as functions of irradiance through the net photosynthesis rate (Leuning, 1995) and as functions of the hydraulic properties of the leaf, specifically of epidermal and guard cells (Dewar, 1995; Lhomme, 1998). These

interpretations of $g_m$ and $E_m$ were supported by the relationships found here between $g_c$ and $Q$ and $\Psi_{soil}$; however, the limited number of observations with a linear decreasing relationship between $g_c$ and $E$ limited analysis of $g_m$ and $E_m$. Again, this hysteresis in our field measurements indicated the difficulty in scaling Monteith's formulation of $g_c$ to canopy level processes in the natural environment.

# 5. CONCLUSIONS

This study is the first of its kind to report year-round, direct measurements of $\lambda E$ and $H$ from a temperate seasonal rainforest ecosystem. One of the principle challenges of this research campaign was to ensure measurement quality despite long periods of inclement weather.

Spectral analysis indicated that in general, the Gill Model 1012R2A sonic anemometer-thermometer can measure the velocity components $u$, $v$, and $w$ in the rain, up to intensities of 4.6 mm $h^{-1}$. The measurement of $T$ was slightly more prone to sporadic spikes and the influence of white noise errors; however, these were shown to have minimal effects on the cospectra of $wT$ and the resulting $H$. Measurements of $\chi_w$ were strongly influenced by high humidity conditions (>70% RH) likely due to water vapour adsorption/desorption effects on the sampling tube and/or filter walls exacerbated by contaminants. This was particularly a concern in the unheated filter and portion of the sampling tube lying between the incoming heated sampling tube and the heated IRGA. Signal attenuation resulted in high frequency losses of $\lambda E$ ranging from 6% to 38%. These losses were significantly minimized with the installation of clean tubing and filters and improved heating. Selecting fluxes associated with good delay times due only to the time required for the air stream to travel the length of the sampling tube was a simple method to identify $\lambda E$ measurements likely to be underestimated due to signal attenuation. Calculations of the high frequency loss in $w\chi_w$ cospectra compared with unaffected $wT$ cospectra were used to apply a maximum possible increase of 62% to $\lambda E$, while empirical transfer functions based on the ratio of $T$ and $\chi_w$ power spectra or $wT$ and $w\chi_w$ cospectra resulted in smaller maximum corrections of 18% and 11%, respectively.

Energy budget closure analysis resulted in a 23% discrepancy between measured turbulent exchange and available energy for half hour measurements. This was despite including an energy storage term of a relatively large magnitude. Correcting $\lambda E$ for signal attenuation losses improved closure only slightly to 80%. 24-h energy budget closure was best during the dry summer months with improved half hour closure occurring during the daytime accompanied by upslope winds from the NE. These conditions tended to coincide with high $u_*$ suggesting that in low $u_*$ conditions, flux transport not included in the eddy covariance measurements may have

occurred (Lee, 1998). In general however, there was a strong correlation between $H + \lambda E$ and $R_a$. With corrections for $\lambda E$ losses during humid conditions, the eddy covariance measurements were clearly capable of characterizing the seasonal variations of energy exchange above this forest on a long-term basis (Goulden et al., 1997).

Seasonal trends in energy exchange over this Douglas-fir stand were strongly influenced by abrupt changes in weather and specifically, in rainfall. In this aerodynamically rough forest, surface conductance was critical in determining how energy absorbed by the stand was partitioned between the convective fluxes. The forest surface conductance was strongly dependent on canopy wetness. Few studies extending over a year were available for comparison; however, over a boreal aspen forest and a southern mixed deciduous forest, leaf emergence and senescence synchronized with $Q$ and $T$ had the greatest impact on energy exchange, also through effects on surface conductance (Black et al., 1996; Blanken et al., 1997; Greco and Baldocchi, 1996).

At this site, convective exchange was dominated by $H$ throughout the summer as has been observed for many other coniferous sites where low surface conductance limits transpiration rates to a greater and lesser extent as soil moisture decreases and increases (Baldocchi et al., 1997; Kelliher et al., 1998). Daytime $\beta$ ranged from about 1.3 to 3.5 without corrections and from 0.9 to 2.5 with the application of the attenuation and Bowen ratio corrections. Daytime $\lambda E/R_a$ varied from 0.18 to 0.40 without corrections and from 0.25 to 0.48 with corrections. Sharp transitions between summer and winter conditions coincided with the end of the spring rains in March 1998 and the beginning of the fall rains in early October 1998. Sensible heat was consistently negative throughout the winter as heat was removed from the air to support evaporation of intercepted water from the wet canopy. Daytime $\beta$ ranged from -0.5 to +0.5 with maximum $\lambda E /R_a$ exceeding unity. This was possibly due to the maritime winter climate of this site characterized by frequent cyclonic disturbances passing over Vancouver Island bringing mild temperatures and rain. During the winter of 1998/99, La Niña conditions prevailed bringing cooler temperatures and snow to the site. As a result, despite an additional 250 mm of precipitation that winter, total evaporation was slightly less than the previous winter. In contrast, northern temperate continental sites with winters dominated by high pressure systems and cold, clear conditions are dominated by positive $H$ throughout the winter (Blanken et al., 1997). At these sites, water is essentially unavailable for evaporation in the form of snow and ice while transpiration mostly ceases with leaf senescence and canopy dormancy.

Sustained downward $H$ on a 24-h basis over an entire season had not been directly measured using any technique, particularly the eddy covariance method, for periods any longer than a few rainy weeks in spring and summer conditions (Mizutani et al., 1997) prior to this study. In this study, high rates of $\lambda E$ from the wet or partially wet canopy exceeded $\lambda E_{eq}$ and even potential rates (Equation (2.6)) during both daytime and nighttime periods. When the canopy was wet, surface conductance became unlimiting such that evaporation rates were only limited by the atmospheric demand and the supply of energy required to enable water to evaporate. Winter evaporation rates were therefore far from negligible ranging from 9.2 to 18.9 mm per month and 18.3 to 33.4 mm per month after the application of both signal attenuation and Bowen ratio corrections. Significant wet canopy and nighttime $\lambda E$ required a non-zero $D$ and sufficient turbulence. However, $D$ could be as small as 0.005 kPa to support relatively large positive $\lambda E$ with $u_*$ in excess of 0.5 m $s^{-1}$. With our direct measurements of $\lambda E$, evaporation was observed to occur both during rainfall and after. However, there was no evidence of systematically increased rates of evaporation during rainfall for the diurnal periods illustrated or throughout the measurement period.

Certainly these observations support the suggestion that a wet forest canopy may act as a sink for energy (Pearce and Rowe, 1980; Stewart, 1977). In addition, they provide evidence to support the results from interception and micrometeorological studies describing high evaporative losses over tall, rough forests such as the Plynlimon and Thetford forests (Shuttleworth and Calder, 1979; Stewart, 1977; Thom and Oliver, 1977) and nighttime evaporation rates (Pearce and Rowe, 1980) both exceeding radiative energy inputs on a half hour to annual basis.

Water loss to the atmosphere from this canopy was dominated by dry canopy, summer evaporation, primarily through the process of transpiration. Between April and September, total evaporation accounted for 74% of the total 402 mm of water lost to the atmosphere in 1998 with average evaporation rates of 1.57 mm $day^{-1}$ and a maximum rate of 3.56 mm $day^{-1}$. However, evaporation rates were clearly limited by the surface conductance through physiological control of water loss. Evaporation rates from the dry canopy were always much lower than $\lambda E_{eq}$ as illustrated by low midday $\alpha$ values which ranged from 0.20 to 0.55 or 0.30 to 0.70 corrected for signal attenuation and energy budget closure. On a diurnal time scale, $\lambda E$ tended to be in phase with $D$ rather than $R_a$ clearly indicating the importance of limiting $g_c$. Mean daytime $g_c$ was observed to be about 6 mm $s^{-1}$. By the end of the summer, drought stress symptoms associated

with low $\Psi_{soil}$ at about -1 MPa resulted in afternoon $g_c$ low enough (< 4 mm $s^{-1}$) to suppress $\lambda E$ in the late afternoon, bringing these fluxes in phase with $R_a$ and $H$.

Significant relationships were found between $g_c$ and $\Psi_{soil}$, $Q$ and $D$. Canopy conductance was observed to increase with increasing $Q$, increasing $\Psi_{soil}$ and decreasing $D$, indicating the important environmental influences on stomatal control of water loss. However, when $\Psi_{soil}$ was less than -1 MPa, $g_c$ remained low regardless of changes in $D$ suggesting that the trees were experiencing drought stress symptoms late in the summer. The relationship between $g_c$ and $D$ was best described using Equation (4.11), a decreasing hyperbolic function characteristic of a negative feedback response to $D$. This also supported the hypothesis that $g_c$ responds directly to $E$ and only indirectly to $D$ (Monteith, 1995b). Support for the Monteith formulation of $g_c$ (Equation (2.9)) was evident during the late morning hours approximately between 08:00 h and 12:00 h when $g_c$ decreased with increasing $E$. However, $g_c$ and $E$ tended to be positively linearly related for the remainder of the day. This second type of $g_c$ behaviour was indicative of an apparent feedforward response. It was therefore evident that a decreasing hyperbolic relationship between $g_c$ and $D$ did not imply a negatively linear relationship between $g_c$ and $E$. Ultimately, the simple linear relationship between $g_c$ and $E$ put forth by Monteith (1995b) was not enough to describe the behaviour of $g_c$ in the natural environment. This was likely due to the complex nature of the mechanisms involved in stomatal control not encompassed by this hypothesis such as hormonal responses and concurrent carbon assimilation processes, for example.

Results from this study emphasized how the controls on evaporative water loss and energy exchange from a canopy may change abruptly between and within the seasons. As a result, models of temperate areas with both wet and dry climates must include parameterizations that incorporate the varying physical and physiological processes for the control of evaporative fluxes. Inclusion of the physiological control on $\lambda E$ during the summer is critical. Canopy conductance at this site appeared to be well correlated with environmental variables suggesting that fitted empirical models such as the Jarvis-type and semi-empirical stomatal constraint functions would likely be successful. However, these models tend to be specific to a particular vegetation-climate system. As interannual climate variability becomes increasingly pronounced with global change, alluded to here by the contrasting El Niño/La Niña winter weather conditions, the usefulness of these models in predicting how plants will respond to global change is uncertain (Collatz et al., 1991). The emphasis in atmosphere-ecosystem research must remain

on increasing our understanding of the underlying mechanisms controlling energy exchange in order to predict how forest functioning will respond to global climate change.

# 6. REFERENCES

Amiro, B.D., 1990. Drag coefficients and turbulence spectra within three boreal forest canopies. Boundary-Layer Meteorology, 52: 227-246.

Anthoni, P.M., Law, B.E. and Unsworth, M.H., 1999. Carbon and water vapor exchange of an open-canopied ponderosa pine ecosystem. Agricultural and Forest Meteorology, 95: 151-168.

Aston, A.R., 1985. Heat storage in a young eucalypt forest. Agricultural and Forest Meteorology, 35: 281-297.

Baldocchi, D.D., Vogel, C.A. and Hall, B., 1997. Seasonal variation of energy and water vapour exchange rates above and below a boreal jack pine forest canopy. Journal of Geophysical Research, 102(D24): 28939-28951.

Ball, J.T., Woodrow, I.E. and Berry, J.A., 1987. A model predicting stomatal conductance and its contribution to the control of photosynthesis under different environmental conditions. In: J. Biggens (Editor), Progress in Photosynthesis Research. Martinus Nijhoff Publishers, Dordrecht, pp. 221-224.

Barr, G.B., King, K.M., Gillespie, T.J., Den Hartog, G. and Neumann, H.H., 1994. A comparison of Bowen ratio and eddy correlation sensible and latent heat flux measurements above a deciduous forest. Boundary-Layer Meteorology, 71: 21-41.

Bernhofer, C., 1992. Estimating forest evapotranspiration at a non-ideal site. Agricultural and Forest Meteorology, 60: 17-32.

Black, C.A. (Editor), 1965. Methods of Soil Analysis Part 1. Agronomy, No. 9. American Society of Agronomy, Madison, Wisconsin, 770 pp.

Black, T.A., 1999. Personal communication. University of British Columbia, Vancouver, B.C. V6T 1Z4

Black, T.A., Chen, J.M., Lee, X. and Sagar, R.M., 1991. Characteristics of shortwave and longwave irradiances under a Douglas-fir forest stand. Canadian Journal of Forest Research, 21(7): 1020-1028.

Black, T.A. et al., 1996. Annual cycles of water vapour and carbon dioxide fluxes in and above a boreal aspen forest. Global Change Biology, 2: 219-229.

Black, T.A. and Kelliher, F.M., 1989. Processes controlling understory evapotranspiration. Philosophical Transactions of the Royal Society of London, B 324: 207-231.

Blanken, P.D., 1997. Evaporation within and above a boreal aspen forest, University of British Columbia, Vancouver, BC, 185 pp.

Blanken, P.D. et al., 1997. Energy balance and canopy conductance of a boreal aspen forest: Partitioning overstory and understory components. Journal of Geophysical Research, 102(D24): 28915-28927.

Blanken, P.D. et al., 1998. Turbulent flux measurements above and below the overstory of a boreal aspen forest. Boundary-Layer Meteorology, 89: 109-140.

Calder, I.R., 1976. The measurement of water losses from a forested area using a "natural" lysimeter. Journal of Hydrology 30: 311-325.

Calder, I.R., 1996. Water use by forests at the plot and catchment scale. Commonwealth Forestry Review, 75(1): 19-30.

Calder, I.R. and Wright, I.R., 1986. Gamma ray attenuation studies of interception from Sitka spruce: Some evidence for an additional transport mechanism. Water Resources Research, 22(3): 409-417.

Campbell, G.S. and Norman, J.M., 1998. An Introduction to Environmental Biophysics. Springer-Verlag, New York, 286 pp.

Cohen, Y., Kelliher, F.M. and Black, T.A., 1985. Determination of sap flow in Douglas-fir trees using the heat pulse technique. Canadian Journal of Forest Research, 15: 422-428.

Collatz, G.J., Ball, J.T., Grivet, C. and Berry, J.A., 1991. Physiological and environmental regulation of stomatal conductance, photosynthesis and transpiration: a model that includes a laminar boundary layer. Agricultural and Forest Meteorology, 54: 107-136.

Cowan, I.R., 1994. As to the mode of action of the guard cells in dry air. In: E.-D. Schulze and M.M. Caldwell (Editors), Ecophysiology of Photosynthesis. Ecological Studies. Springer-Verlag, New York, pp. 205-229.

de Bruin, H.A.R., 1989. Physical aspects of the planetary boundary layer. In: T.A. Black, D.L. Spittlehouse, M.D. Novak and D.T. Price (Editors), Estimation of Areal Evapotranspiration (Proceedings of a workshop held at Vancouver, BC, Canada, August 1987). IAHS, Vancouver, BC, pp. 117-132.

Denmead, O.T. and Bradley, E.F., 1985. Flux-gradient relationships in a forest canopy. In: B.A. Hutchinson and B.B. Hicks (Editors), The Forest-Atmosphere Interaction. Dordrecht Reidel, Boston, pp. 421-442.

Dewar, R.C., 1995. Interpretation of an empirical model for stomatal conductance in terms of guard cell function. Plant, Cell and Environment, 18: 365-372.

Environment Canada, 1998. Pacific and Yukon Region: El Niño and La Niña. Taylor, Bill. http://www.weatheroffice.com/ElNino/default.html

Farquhar, G.D., 1978. Feedforward responses of stomata to humidity. Australian Journal of Plant Physiology, 5: 787-800.

Foken, T. and Wichura, B., 1996. Tools for quality assessment of surface-based flux measurements. Agricultural and Forest Meteorology, 78: 83-105.

Franks, P.J., Cowan, I.R. and Farquhar, G.D., 1997. The apparent feedforward response of stomata to air vapour pressure deficit: information revealed by different experimental procedures with two rainforest trees. Plant, Cell and Environment, 20: 142-145.

Garratt, J.R. and Francey, R.J., 1978. Bulk characteristics of heat transfer in the unstable , baroclinic atmospheric boundary layer. Boundary-Layer Meteorology, 15: 399-421.

Gash, J.H.C., 1986. A note on estimating the effect of limited fetch on micrometerological evaporation measurements. Boundary-Layer Meteorology, 35: 409-413.

Gash, J.H.C., Valente, F. and David, J.S., 1999. Estimates and measurements of evaporation from wet, sparse pine forest in Portugal. Agricultural and Forest Meteorology, 94: 149-158.

Gillespie, T.J. and Kidd, G.E., 1978. Sensing duration of leaf moisture retention using electrical impedance grids. Canadian Journal of Plant Science, 58: 179-187.

Goulden, M.L. et al., 1997. Physiological responses of a black spruce forest to weather. Journal of Geophysical Research, 102(D24): 28987-28996.

Gramann, U., 1996. Determination of the signal attenuation by the tubing of an infrared gas analysis system used to make eddy-correlation flux measurements. Diplomarbeit Thesis, Universität Karlsruhe, Germany, 125 pp.

Grantz, D.A., 1990. Plant response to atmospheric humidity. Plant, Cell and Environment(13): 667-679.

Greco, S. and Baldocchi, D.D., 1996. Seasonal variations of $CO_2$ and water vapour exchange rates over a temperate deciduous forest. Global Change Biology, 2: 183-197.

Grelle, A., Lundberg, A., Lindroth, A. and Moren, A.S., 1997. Evaporation components of a boreal forest: variations during the growing season. Journal of Hydrology, 197: 70-87.

Herrington, L.P., 1969. On temperatures and heat flow in tree stems. No. 73, Yale University, School of Forestry, New Haven, CT.

Jarvis, P.G., 1976. The interpretation of the variations in leaf water potential and stomatal conductance found in canopies in the field. Philosophical Transactions of the Royal Society of London Series B - Biological Sciences, 273: 593-610.

Jarvis, P.G., James, G.B. and Landsberg, J.J., 1976. Coniferous forest. In: J.L. Monteith (Editor), Vegetation and the Atmosphere. Academic Press, London, pp. 171-240.

Jones, H.G., 1992. Plants and microclimate: a quantitative approach to environmental plant physiology. Cambridge University Press, New York, 428 pp.

Judd, M., 1995. To G or not to G - a cautionary and fluxing tale, WISPAS, 61. HortResearch, Palmerston North, New Zealand.

Kaimal, J.C. and Finnigan, J.J., 1994. Atmospheric Boundary Layer Flows: Their Structure and Measurement. Oxford University Press, New York, 289 pp.

Kaimal, J.C., Wyngaard, J.C., Izumi, Y. and Cote, O.R., 1972. Spectral characteristics of surface layer turbulence. Quarterly Journal of the Royal Meteorological Society, 98: 563-589.

Kelliher, F.M., Leuning, R. and Schulze, E.-D., 1993. Evaporation and canopy characteristics of coniferous forests and grasslands. Oecologia, 95: 153-163.

Kelliher, F.M., Leuning, R., Raupach, M.R. and Schulze, E.-D., 1995. Maximum conductances for evaporation from global vegetation types. Agricultural and Forest Meteorology, 73: 1-16.

Kelliher, F.M. et al., 1998. Evaporation from a central Siberian pine forest. Journal of Hydrology, 205: 279-296.

Klaassen, W., Bosveld, F. and de Water, E., 1998. Water storage and evaporation as constituents of rainfall interception. Journal of Hydrology, 212-213: 36-50.

Klute, A. (Editor), 1986. Methods of Soil Analysis Part 1. Physical and Mineralogical Methods. Agronomy, No. 9. American Society of Agronomy Inc. & Soil Science Society of America Inc., Madison, Wisconsin, 1188 pp.

Kristensen, L., Mann, J., Oncley, S.P. and Wyngaard, J.C., 1997. How close is close enough when measuring scalar fluxes with displaced sensors? Journal of Atmospheric and Oceanic Technology, 14: 814-821.

Laubach, J., Raschendorfer, M., Kreilein, H. and Gravenhorst, G., 1994. Determination of heat and water vapour fluxes above a spruce forest by eddy correlation. Agricultural and Forest Meteorology, 71: 373-401.

Laubach, J. and Teichmann, U., 1996. Measuring energy budget components by eddy correlation: Data corrections and application over low vegetation. Beitr. Phys. Atmosph., 69(2): 307-320.

Leclerc, M.Y. and Thurtell, G.W., 1990. Footprint prediction of scalar fluxes using a Markovian analysis. Boundary-Layer Meteorology, 52: 247-258.

Lee, X., 1998. On micrometeorological observations of surface-air exchange over tall vegetation. Agricultural and Forest Meteorology, 91: 39-49.

Lee, X. and Black, T.A., 1993. Atmospheric turbulence within and above a Douglas-fir stand. Part II: Eddy fluxes of sensible heat and water vapour. Boundary-Layer Meteorology, 64: 369-389.

Leuning, R., 1995. A critical appraisal of a combined stomatal-photosynthesis model for $C_3$ plants. Plant, Cell and Environment, 18: 339-355.

Leyton, L., Reynolds, E.R.C. and Thompson, F.B., 1965. Rainfall interception in forest and moorland. In: W.E. Sopper and H.W. Lull (Editors), Forest Hydrology. Proc. Nat. Sci. Found. Adv. Sci. Sem. Pennsylvania State University, University Park, Pennsylvania, pp. 163-178.

Lhomme, J.-P., 1998. Stomatal control of transpiration: Examination of Monteith's formulation of canopy resistance. Water Resources Research, 34(9): 2301-2308.

LI-COR, I., 1996. LI-6262 $CO_2/H_2O$ Analyzer Instruction Manual. Publication Number 9003-59, LI-COR, Inc., Lincoln, Nebraska.

Lindroth, A., 1985. Canopy conductance of coniferous forests related to climate. Water Resources Research, 21(3): 297-304.

Lindroth, A., 1985. Seasonal and diurnal variation of energy budget components in coniferous forests. Journal of Hydrology, 82: 1-15.

Lloyd, J., 1991. Modelling stomatal responses to environment in *Macadamia integrifolia*. Australian Journal of Plant Physiology, 18: 649-660.

Lohammar, T., Larsen, S., Linder, S. and Falk, S.O., 1980. FAST-simulation models of gaseous exchange in Scots pine. In: T. Persson (Editor), Structure and function of northern coniferous forests - an ecosystem study. Ecological Bulletin, pp. 505-523.

Massman, W.J.J., 1991. The attenuation of concentration fluctuations in turbulent flow through a tube. Journal of Geophysical Research, 96(D8): 15269-15273.

McCaughey, J.H. et al., 1997. Magnitudes and seasonal patterns of energy, water, and carbon exchanges at a boreal young jack pine forest in the BOREAS northern study area. Journal of Geophysical Research, 102(D24): 28997-29007.

McCaughey, J.H. and Saxton, W.L., 1988. Energy balance storage terms in a mixed forest. Agricultural and Forest Meteorology, 44: 1-18.

McGinn, S.M., King, K.M. and Thurtell, G.W., 1989. Reducing dew and frost on the domes of net pyrradiometers. Journal of Atmospheric and Oceanic Technology, 6: 528-531.

McNaughton, K.G. and Black, T.A., 1973. A study of evapotranspiration from a Douglas fir forest using the energy balance approach. Water Resources Research, 9(6): 1579-1590.

McNaughton, K.G. and Jarvis, P.G., 1983. Predicting effects of vegetation changes on transpiration and evaporation. In: T.T. Kozlowski (Editor), Water Deficits and Plant Growth. Academic Press Inc., New York, pp. 1-47.

McNaughton, K.G. and Spriggs, T.W., 1989. An evaluation of the Priestley and Taylor equation and the complementary relationship using results from a mixed-layer model of the convective boundary layer. In: T.A. Black, D.L. Spittlehouse, M.D. Novak and D.T. Price (Editors), Estimation of Areal Evapotranspiration (Proceedings of a workshop held at Vancouver, BC, Canada, August 1987). IAHS, Vancouver, BC, pp. 89-104.

Meesters, A.G.C.A. and Vugts, H.F., 1996. Calculation of heat storage in stems. Agricultural and Forest Meteorology, 78: 181-202.

Meinzer, F.C. et al., 1997. Control of transpiration from the upper canopy of a tropical forest: the role of stomatal, boundary layer and hydraulic architecture components. Plant, Cell and Environment, 20: 1242-1252.

Mizutani, K., Yamanoi, K., Ikeda, T. and Watanabe, T., 1997. Applicability of the eddy correlation method to measure sensible heat transfer to forest under rainfall conditions. Agricultural and Forest Meteorology, 86: 193-203.

Moncrieff, J.B., Malhi, Y. and Leuning, R., 1996. The propagation of errors in long-term measurements of land-atmosphere fluxes of carbon and water. Global Change Biology, 2: 231-240.

Monteith, J.L., 1965. Evaporation and environment. Symp. Soc. Exp. Biol.(XIX): 205-234.

Monteith, J.L., 1995a. Accommodation between transpiring vegetation and the convective boundary layer. Journal of Hydrology, 166: 251-263.

Monteith, J.L., 1995b. A reinterpretation of stomatal responses to humidity. Plant, Cell and Environment, 18: 357-364.

Monteith, J.L. and Unsworth, M.H., 1990. Principles of Environmental Physics. Edward Arnold, London, 291 pp.

Moore, C.J., 1976. Eddy flux measurements above a pine forest. Quarterly Journal of the Royal Meteorological Society, 102: 913-918.

Moore, C.J., 1986. Frequency response corrections for eddy correlation systems. Boundary-Layer Meteorology, 37: 17-35.

Moore, C.J. and Fisch, G., 1986. Estimating heat storage in Amazonian tropical forest. Agricultural and Forest Meteorology, 38: 147-169.

Mott, K.A., Cardon, Z.G. and Berry, J.A., 1993. Asymmetric patchy stomatal closure for the two surfaces of *Xanthium strumarium* L. leaves at low humidity. Plant, Cell and Environment, 16: 25-34.

Mott, K.A. and Parkhurst, D.F., 1991. Stomatal responses to humidity in air and helox. Plant, Cell and Environment, 14: 509-515.

Oke, T. and Hay, J., 1994. The Climate of Vancouver. B.C. Geographical Series, No. 50. University of British Columbia, Vancouver, British Columbia, 84 pp.

Oke, T.R., 1987. Boundary Layer Climates. Methuen, London, 435 pp.

Pataki, D.E., Oren, R., Katul, G. and Sigmon, J., 1998. Canopy conductance of *Pinus taeda, Liquidambar styraciflua* and *Quercus phellos* under varying atmospheric and soil water conditions. Tree Physiology, 18: 307-315.

Pattey, E., Desjardins, R.L. and St-Amour, G., 1997. Mass and energy exchanges over a black spruce forest during key periods of BOREAS 1994. Journal of Geophysical Research, 102(D24): 28967-28975.

Pearce, A.J. and Rowe, L.K., 1980. Nighttime, wet canopy evaporation rates and the water balance of an evergreen mixed forest. Water Resources Research, 16(5): 955-959.

Pojar, J. and MacKinnon, A., 1994. Plants of Coastal British Columbia. Lone Pine Publishing, Vancouver, British Columbia.

Price, D.T. and Black, T.A., 1990. Effects of short-term variation in weather on diurnal canopy $CO_2$ flux and evapotranspiration of a juvenile Douglas-fir stand. Agricultural and Forest Meteorology, 50: 139-158.

Priestley, C.H.B. and Taylor, R.J., 1972. On the assessment of surface heat flux and evaporation using large-scale parameters. Mon. Weather Rev., 100: 81-92.

Rutter, A.J., 1967. An analysis of evaportion from a stand of Scots pine. In: W.E. Sopper and H.W. Lull (Editors), International Symposium on Forest Hydrology. Pergamon Press, New York, pp. 403-417.

Rutter, A.J., Kershaw, K.A., Robins, P.C. and Morton, A.J., 1971. A predictive model of rainfall interception in forests, I. Derivation of the model from observations in a plantation of corsican pine. Agricultural and Forest Meteorology, 9: 367-384.

Saliendra, N.Z., Sperry, J.S. and Comstock, J.P., 1995. Influence of leaf water status on stomatal response to humidity, hydraulic conductance, and soil drought in *Betula occidentalis*. Planta, 196: 357-366.

Schapp, M.G., Bouten, W. and Verstraten, J.M., 1997. Forest floor water content dynamics in a Douglas fir stand. Journal of Hydrology, 201: 367-383.

Schuepp, P.H., Leclerc, M.Y., MacPherson, J.I. and Desjardins, R.L., 1990. Footprint prediction of scalar fluxes from analytical solutions of the diffusion equation. Boundary-Layer Meteorology, 50: 355-373.

Schulze, E.-D., Lange, O.L., Bushbom, U., Kappen, L. and Evenari, M., 1972. Stomatal responses to changes in humidity in plants growing in the desert. Planta, 108: 259-270.

Sheriff, D.W., 1984. Epidermal tranpiration and stomatal responses to humidity: some hypotheses explored. Plant, Cell and Environment, 7: 669-677.

Shuttleworth, W.J. and Calder, I.R., 1979. Has the Priestly-Taylor equation any relevance to forest evaporation? Journal of Applied Meteorology, 18: 639-646.

Simpson, I., 1996. Trace gas exchange and the validity of similarity theory in the roughness sublayer above forests, University of Guelph, Guelph, Ontario, 205 pp.

Singh, B. and Szeicz, G., 1979. The effect of intercepted rainfall on the water balance of a hardwood forest. Water Resources Research, 14(1): 131-138.

Smith, J. and Campbell, D., 1999. Eddy covariance measurements of water vapour and $CO_2$ fluxes in a Waikato peat bog, WISPAS, 73. Hort Research, Palmerston North, New Zealand.

Stewart, J.B., 1977. Evaporation from the wet canopy of a pine forest. Water Resources Research, 13(6): 915-921.

Stewart, J.B., 1988. Modelling surface conductance of pine forest. Agricultural and Forest Meteorology, 43: 19-35.

Stewart, J.B. and Thom, A.S., 1973. Energy budgets in pine forest. Quarterly Journal of the Royal Meteorological Society, 99: 154-170.

Stull, R.B., 1988. An Introduction to Boundary Layer Meteorology. Kluwer Academic Publishers, Dordrecht, 666 pp.

Tan, C.S. and Black, T.A., 1976. Factors affecting the canopy resistance of a Douglas-fir forest. Boundary-Layer Meteorology, 10: 475-488.

Tan, C.S., Black, T.A. and Nnyamah, J.U., 1977. Characteristics of stomatal diffusion resistance in a Douglas fir forest exposed to soil water deficits. Canadian Journal of Forest Research, 7(4): 595-604.

Tan, C.S., Black, T.A. and Nnyamah, J.U., 1978. A simple diffusion model of transpiration applied to a thinned Douglas-fir stand. Ecology, 59(6): 1221-1229.

Tanner, B.D., Swiatek, E. and Greene, J.P., 1993. Density fluctuations and use of the krypton hygrometer in surface flux measurements, 1993 National Conference on Irrigation and Drainage Engineering, Irrigation and Drainage Division, American Society of Civil Engineers. ASCE, Park City, Utah, pp. 945-952

Tanner, C.B. and Thurtell, G.W., 1969. Anemoclinometer measurements of Reynolds stress and heat transport in the atmospheric surface layer. ECOM 66-G22-F, University of Wisconsin, Madison, Wisconsin.

Teklehaimanot, Z. and Jarvis, P.G., 1991. Direct measurement of evaporation of intercepted water from forest canopies. Journal of Applied Ecology, 28: 603-618.

The MathWorks, I., 1996. Using MATLAB, Version 5. The MathWorks, Inc., Natick, MA.

Thom, A.S. and Oliver, H.R., 1977. On Penman's equation for estimating regional evaporation. Quarterly Journal of the Royal Meteorological Society, 103: 345-357.

Thompson, M.A., Campbell, D.I. and Spronken-Smith, R.A., 1999. Evaporation from natural and modified raised peat bogs in New Zealand. Agricultural and Forest Meteorology, 95: 85-98.

Valente, F., David, J.S. and Gash, J.H.C., 1997. Modelling interception loss for two sparse eucalypt and pine forests in central Portugal using reformulated Rutter and Gash analytical models. Journal of Hydrology, 190: 141-162.

van Genuchten, M.T., 1980. A closed-form equation for predicting the hydraulic conductivity of unsaturated soils. Soil Sci. Am. J., 44: 892-898.

Verma, S.B., 1989. Aerodynamic resistances to transfers of heat, mass and momentum. In: T.A. Black, D.L. Spittlehouse, M.D. Novak and D.T. Price (Editors), Estimation of Areal Evapotranspiration (Proceedings of a workshop held at Vancouver, BC, Canada, August 1987). IAHS, Vancouver, BC, pp. 13-20.

Webb, E.K., Pearman, G.I. and Leuning, R., 1980. Correction of flux measurements for density effects due to heat and water vapor transfer. Quarterly Journal of the Royal Meteorological Society 106: 85-100.

Wilson, J.D. and Schuepp, P.H., 1987. Reports of group discussions. In: T.A. Black, D.L. Spittlehouse, M.D. Novak and D.T. Price (Editors), Estimation of Areal Evapotranspiration (Proceedings of a workshop held at Vancouver, BC, Canada, August 1987). IAHS, Vancouver, BC, pp. 287-290.

Wong, S.C., Cowan, I.R. and Farquhar, G.D., 1979. Stomatal conductance correlates with photosynthetic capacity. Nature, 282: 424-426.

World Meteorological Organization, 1999. El Niño/La Niña Update. WMO. http://www.wmo.ch/nino/updat.html

Yang, P.C., 1998. Carbon dioxide flux within and above a boreal aspen forest, University of British Columbia, Vancouver, BC, 234 pp.

## APPENDIX A: IRGA CALIBRATION AND MEASUREMENT EQUATIONS

Measurements of $CO_2$ and $H_2O$ were obtained using an IRGA running in absolute mode with $N_2$ gas supplied at 60 cc $min^{-1}$ through the reference cell and sampled air pulled through the sample cell at ~ 9.5 L $min^{-1}$. Each night, the IRGA was calibrated for $CO_2$ measurements by supplying $N_2$ gas (with zero $CO_2$ and $H_2O$ concentration) pulled through the sample cell for 1 min followed by a span gas with 350 μmol/mol of dry air. During each calibration, voltage readings of $CO_2$ and $H_2O$ were recorded along with sample cell pressure ($P_s$) and optical bench temperature ($T_s$). Temperature and pressure were converted to units of °C and kPa from a mV output using LI-6262 specifications. The calibration span gas concentration ($\chi'_{\text{c-calibration}}$) in mole fraction units was converted to a voltage following (LI-COR, 1996),

$$\chi_{c-calibration} = \frac{\chi'_{c-calibration}}{T_s / T_{cal}} \tag{A.1}$$

$$V_{c-calibation} = \frac{f(\chi_{c-calibation})}{101.3 / P_s} \tag{A.2}$$

where $\chi_{\text{c-calibration}}$ is the temperature corrected mole fraction of the span calibration gas, $T_{cal}$ is the temperature of the factory polynomial determination (°C), $f(\chi_{\text{c-calibration}})$ is the inverse 5$^{th}$ order polynomial to convert mole fraction $CO_2$ to voltage (mV) and $V_{c\text{-}calibration}$ is the voltage of the span calibration gas. A calibration gain for $CO_2$ ($gain_{co_2}$) was then calculated in the following manner,

$$gain_{CO_2} = \frac{V_{c-calibration}}{V_c - V_{c-offset}} \tag{A.3}$$

where $V_c$ is the voltage reading during the calibration procedure. This gain was applied to both $H_2O$ and $CO_2$ measurements under the assumption that the changes in calibration were the same. This was confirmed with independent measurements from a dew point hygrometer and a krypton hygrometer (see Section 3.2.1). The offsets for $CO_2$ ($offset_{co_2}$) and $H_2O$ ($offset_{H_2O}$) were the voltage readings from the LI-6262 recorded while $N_2$ was run through the sample cell.

Generally, the relative change in the gain over a period of 10 to 20 days was less than 0.2%. As a result, calibration coefficients were revised only when significant changes were observed with sensor drift or after tank or instrument changes resulting in new coefficients about once every 3 to 5 weeks on average. Instabilities in calibration coefficients due to temperature changes were minimized using a thermostatted box for the IRGA on the tower. Pressure and

temperature measured in the sample cell were used in corrections to account for differences from calibration conditions and were calculated for water vapour measurements as (LI-COR, 1996),

$$C_P = \left(\frac{101.3}{P_s}\right)^{0.9} \tag{A.4}$$

$$C_T = \frac{T_s}{T_{cal}} \tag{A.5}$$

Calibration coefficients were then applied to the voltage readings for $H_2O$ ($V_w'$) and $CO_2$ in addition to the above corrections in the following manner (shown are the conversion equations for $H_2O$ calculations) (LI-COR, 1996),

$$V_w = \left(V_w^{'} + offset_{H_2O}\right) \times gain_{C_2O} \times C_P \tag{A.6}$$

$$\chi_{ww}(\text{mmol / mol wet air}) = f\left(V_w\right) \times P_T \tag{A.7}$$

where $f\left(V_w\right)$ is the IRGA 5$^{th}$ order polynomial applied to voltage readings and $\chi_{ww}$ is the mole fraction for $H_2O$ in mmol/mol of wet air. Finally, the $H_2O$ mole fraction ($\chi_w$) was determined for dry air as,

$$\chi_w(\text{mmol / mol dry air}) = \frac{\chi_{ww}}{1 - \chi_{ww}/1000}. \tag{A.8}$$

## APPENDIX B: WATER RELEASE CURVES AND TEXTURE ANALYSIS

Soil water release curves were determined for 10 sampled cores of soil using a pressure plate apparatus (Klute, 1986) and fitted using van Genuchten's (1980) relationship stated as,

$$\theta_v = \frac{(\theta_{sat} - a)}{\left[1 + \left(b|\Psi_{soil}|\right)^c\right]^{1-\frac{1}{c}}} + a \qquad \text{(B.1)}$$

where $a$, $b$, and $c$ are coefficients determined using non-linear regression, $\theta_v$ is the volumetric water content, $\Psi_{soil}$ is the soil matric potential and $\theta_{sat}$ is the saturated volumetric water content equivalent to the porosity for each of the samples determined from bulk density measurements. Results using nine applied pressures ranging from -25 to -300 kPa are shown in Fig. B.1. For the lower soil layer from cores taken at 70 cm and 50 cm depths, $\theta_{sat}$ = 0.38, $a$ = -1409.94, $b$ = 7267.91, and $c$ = 1.000020494 with an $R^2$ = 0.80. The upper soil layer determined from cores from 50 cm, 30 cm, 14 cm and 6 cm depths was found to have $\theta_{sat}$ = 0.46, $a$ = -1465.57, $b$ = 8634.54, and $c$ = 1.000021519 with an $R^2$ = 0.82.

A relationship between $\theta_v$ and $\Psi_{soil}$ was not found for the surface layer as the sampled core gained weight throughout the pressure plate tests. It appeared that some plant material continued to grow during this time.

Texture of the upper soil layers down to 40 cm were determined using the hydrometer method to be a sandy loam texture while lower layers were sand. Results are shown in Table B.1. These texture results support grouping the upper and lower soil layers together for the retention curve analysis.

Table B.1 Soil texture analysis results using the hydrometer method. Four mineral soil samples were taken for this analysis from 3-4 cm below the surface, 30-40 cm, 50-55 cm and 80 cm. Results are shown for two replicates using the same soil samples.

| | Soil core depths | | | |
|---|---|---|---|---|
| Analysis #1 | 3-4cm | 30-40cm | 50-55cm | 80cm |
| clay (%) | 1.63 | 0.46 | 0.12 | 0.11 |
| sand (%) | 77.15 | 81.04 | 87.12 | 92.5 |
| silt (%) | 21.23 | 18.5 | 12.75 | 7.39 |
| Classification | Loamy Sand | Loamy Sand | Sand | Sand |
| | | | | |
| Analysis #2 | 3-4cm | 30-40cm | 50-55cm | 80cm |
| clay (%) | 4.34 | 2.70 | 0.00 | 0.90 |
| sand (%) | 71.69 | 74.45 | 86.92 | 92.49 |
| silt (%) | 23.97 | 22.84 | 13.08 | 6.61 |
| Classification | Loamy Sand | Loamy Sand | Sand | Sand |

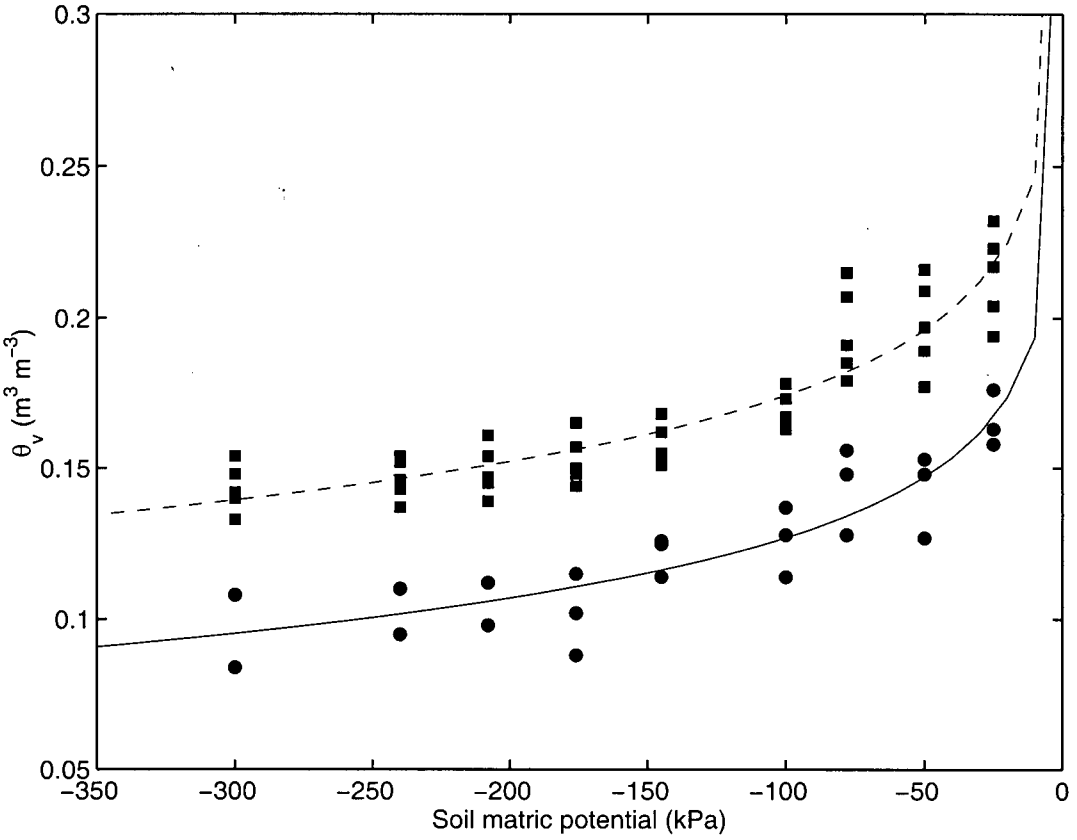


Fig. B.1 The relationship between volumetric water content ($\theta_v$) and soil matric potential ($\Psi_{soil}$) applied in the laboratory to mineral soil cores collected from 70 cm and 50 cm depths (●) and from 50 cm, 30 cm, 14 cm and 6 cm depths (■). The lowest levels (70 and 50 cm) were associated with sand textured soil while the upper levels were a loamy sand. Individual core samples are shown with fitted van Genuchten (1980) functions on grouped data using non-linear regression.

## APPENDIX C: CANOPY STORAGE CAPACITY AND THE FREE THROUGHFALL COEFFICIENT

The Leyton et al. (1965) method for calculating canopy storage capacity ($S$) is shown in Fig. C.1 where throughfall per storm event is related to gross rainfall per storm event. A storm event is a series of half hours with measurable rainfall not separated by more than 2 hours of dry conditions (Klaassen et al., 1998). This avoided defining storms as rain events that began with a partially wet canopy and avoided intermittent rain events from being joined (Klaassen et al., 1998). For storms with total rainfall less than $S$, throughfall increases proportionally as a function of the fraction of rainfall which does not touch the canopy on the way down, known as the free throughfall coefficient ($p$). This may be represented as $\sum P_{th} = p\sum P$. For storms with rainfall greater than $S$, it is assumed that the scatter of points represents variable evaporation from the wet canopy. The upper envelope of these points ideally represents, $\sum P_{th} = \sum P - S$ where evaporation is assumed to be zero. Fig. C.1 illustrates however, that this is not the case as evaporation does continue during rainfall. The canopy storage capacity is then determined as the negative intercept of the y axis.

Using 17 storm events recorded from May 16, 1998 to November 23, 1998 and April 20, 1999 to May 31, 1999 (Fig. C.1), $S$ was estimated to be 1.0 mm, while $p$ was found to be 0.28 using a regression fitted to 20 storms with total rainfall less than 1.0 mm.

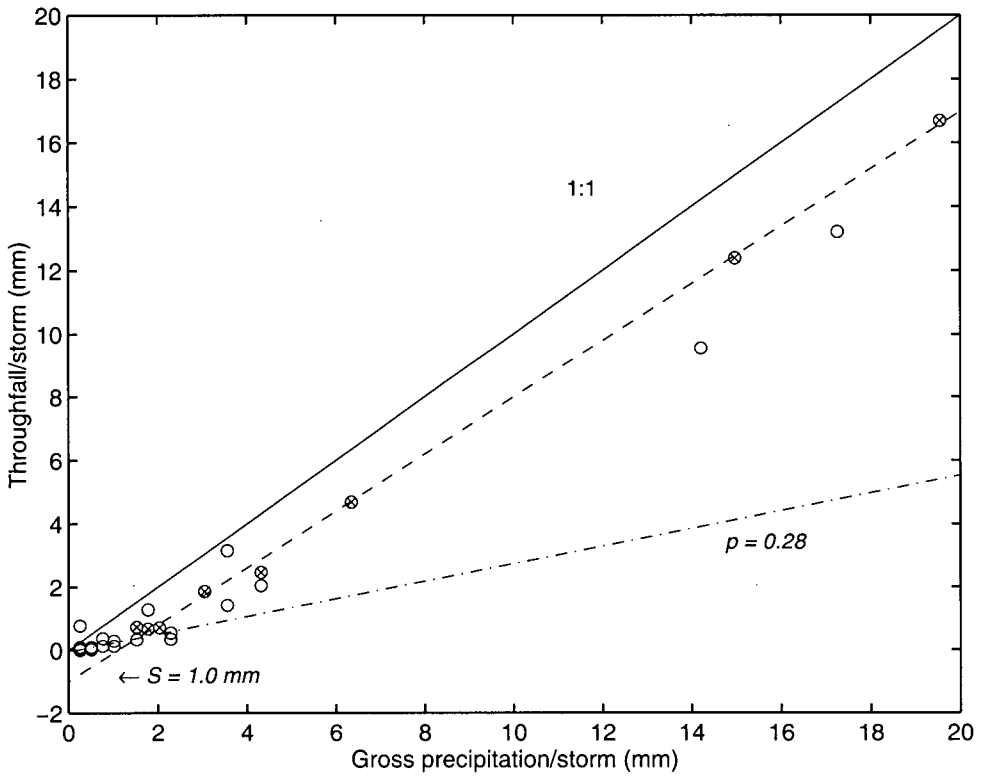


Fig. C.1 The relationship between throughfall and rainfall on a per storm basis for May 16 to November 23, 1998 and April 20 to May 31, 1999. Data from 5 sets of troughs were averaged to give throughfall estimates while gross precipitation was determined with a tipping bucket rain gauge at 27 m on the main triangular tower. Following Leyton et al. (1965), canopy storage capacity ($S$) is 1.0 mm and the free throughfall coefficent ($p$) is 0.28.

## APPENDIX D: TREE BOLE HEAT STORAGE

### Tree form factor:

The tree form factor, $F_f$ used in Equation (3.18) was calculated as the ratio of "true" volume to volume of a cylinder using the diameter at breast height, $d_{bh}$ and total tree height, $h$ as follows,

$$F_f = \frac{\pi \sum_{i=1}^{n-1} \left(d_i^2 + d_{i+1}^2\right)\left(h_i - h_{i+1}\right)/8}{\pi (d_{bh}/2)h} \qquad \text{(D.1)}$$

where $n$ = 10, $d_i$ is the diameter of each section at height $h_i$ given in Table D.1.

Table D.1 Tree bole diameters ($d_i$) associated with 10 heights ($h_i$) up a reference Douglas-fir tree near the scaffold tower at the Campbell River site.

| Height (m) | 0 | 1.30 | 1.63 | 1.88 | 3.00 | 10.67 | 19.82 | 22.87 | 25.91 | 28.96 |
|---|---|---|---|---|---|---|---|---|---|---|
| Diameter (m) | 0.42 | 0.32 | 0.33 | 0.31 | 0.30 | 0.24 | 0.16 | 0.13 | 0.06 | 0 |

$F_f$ was determined to be 0.4871 using the measurements listed in Table D.1 from a Douglas-fir reference tree 29 m tall with a $d_{bh}$ of 0.315 m located adjacent to the scaffold tower. A volume correction was applied to $S_t$ to account for the difference in area of the reference tree used to calculate $F_f$ and the mean tree area within the stand and was simply a ratio of the area of the mean tree using a radius = 0.2374 m to the area of the measured tree using a radius of 0.164 for tree #1 and 0.15 m for tree # 2 (the reference tree).

### Tree bole temperature measurements at crown heights:

The effect of including measurements of tree bole temperature above 3 m at a second height of 27 m is illustrated in Fig. D.1. At 27 m, tree temperatures at these shallow depths of 2 and 28 mm exhibited a greater diurnal amplitude and less damped variations in temperature as a function of insolation of the trunk surface. Below the canopy, little light was able to penetrate and cause these effects. However, the volume of the tree experiencing these conditions at 27 m was a small proportion of the total tree due to bole taper and the dense nature of the canopy. As a result, tree bole heat storage did not show large deviations from that calculated using only the 3 m temperature measurements.

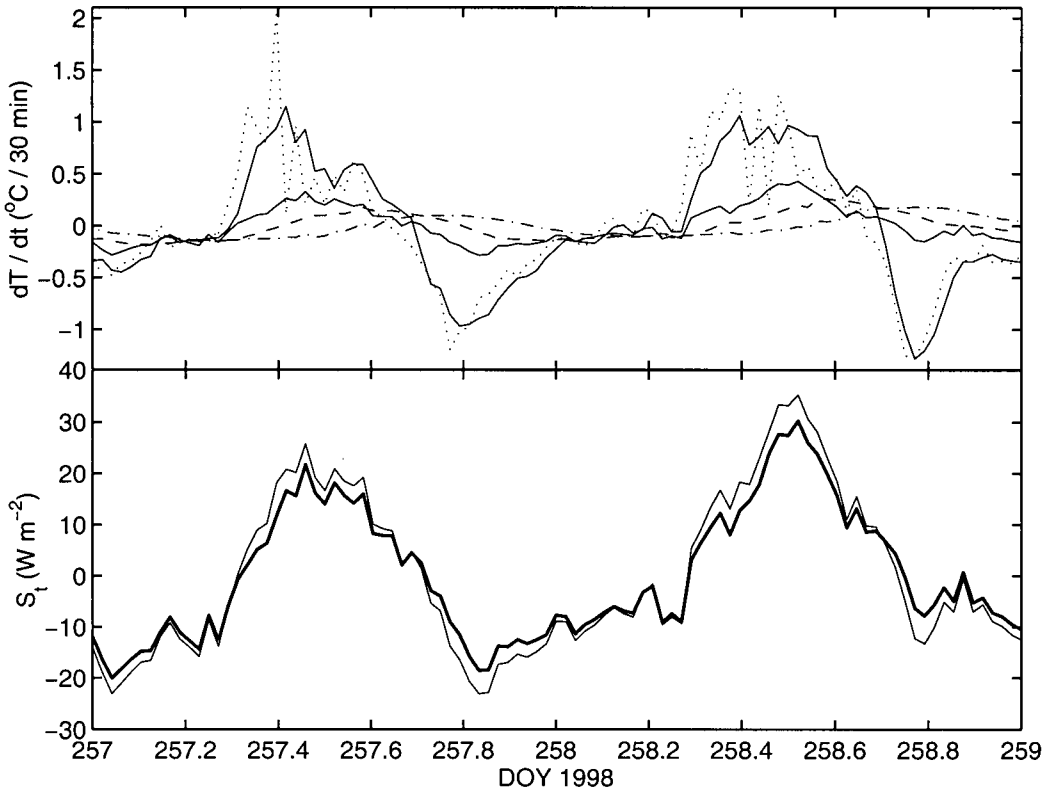


Fig. D.1 Changes in tree temperature with time within tree #2 at 3 m above the ground, 2 mm (solid line), 50 mm (dashed), and 150 mm deep (dash-dotted) and at 27 m above the ground 2 mm (dotted line) and 27.9 mm deep (solid line with large variation)(top panel). The resultant tree heat storage using the direct method with both levels (light solid line) and with only the bottom level (heavy solid line)is shown in the bottom panel.

**Herrington's surface heat flux model:**

Given that a tree bole can be approximated by a cylinder, Herrington (1969) solved the equation for heat conduction in a cylinder using tree surface temperature as the boundary condition presumed to be sinusoidal and expressed as a periodic function of time. Herrington (1969) then assumed an absence of heat flow in the axial and tangential directions and an absence of heat production or removal in the bole. The first two assumptions are more likely to hold in a closed canopy where less insolation of the tree bole surface would occur. The third assumption is valid if heat generation due to cellular respiration is negligible and the generation or removal of heat via the transpiration stream which depends on the relative warmth of the

source and the sink can also be considered negligible. This applies when the model is applied above a certain critical tree height above the ground which acts as a source and sink.

The heat conduction equation for a tree can be expressed as,

$$C_t \frac{\partial T}{\partial t} = k \frac{\partial^2 T}{\partial r^2} + \frac{1}{r} \frac{\partial T}{\partial r} \tag{D.2}$$

where $T$ is temperature, $t$ is time, $r$ is the tree radius, $C_t$ is volumetric heat capacity of the tree and $k$ is the thermal conductivity.

The surface heat flux ($q$) across the bole surface is,

$$q = k \left. \frac{\partial T_t}{\partial r} \right|_{r=0} \tag{D.3}$$

where $T_t$ is tree surface temperature. Differentiation of Equation (D.3) with the solution to Equation (D.2) using a sinusoidal temperature function as the boundary condition leads to the equation for the surface heat flux in the form,

$$\mathrm{q} = k\Delta \mathrm{T_t} \Gamma \sqrt{\frac{\omega}{\kappa}} \cos(\omega \mathrm{t} + \phi - \beta) \tag{D.4}$$

where $\Gamma$ is the gain and quantifies the ratio of the amplitude of heat flux across the surface of a cylinder to that of a semi-infinite slab while $\beta$ is the phase lead of the heat flux into a cylinder (Herrington, 1969). $\kappa$ is the thermal diffusivity of wood, $\omega$ is the angular velocity and $\phi$ is the phase lag in radians. Equation (D.4) undergoes a final assumption asserting that boles of a large enough diameter are well approximated by an infinite slab. As a result, $\Gamma = 1$ and $\beta = \pi/4$ (Herrington, 1969). The basis for this approximation is that as the bole radius becomes greater than the penetration depth of the heat, the heat storage becomes a function of the surface area rather than the bole volume (Meesters and Vugts, 1996). Equation (D.4) is then multiplied by a representative tree surface area and stand density to obtain $S_t$ in W $m^{-2}$ (Herrington, 1969).

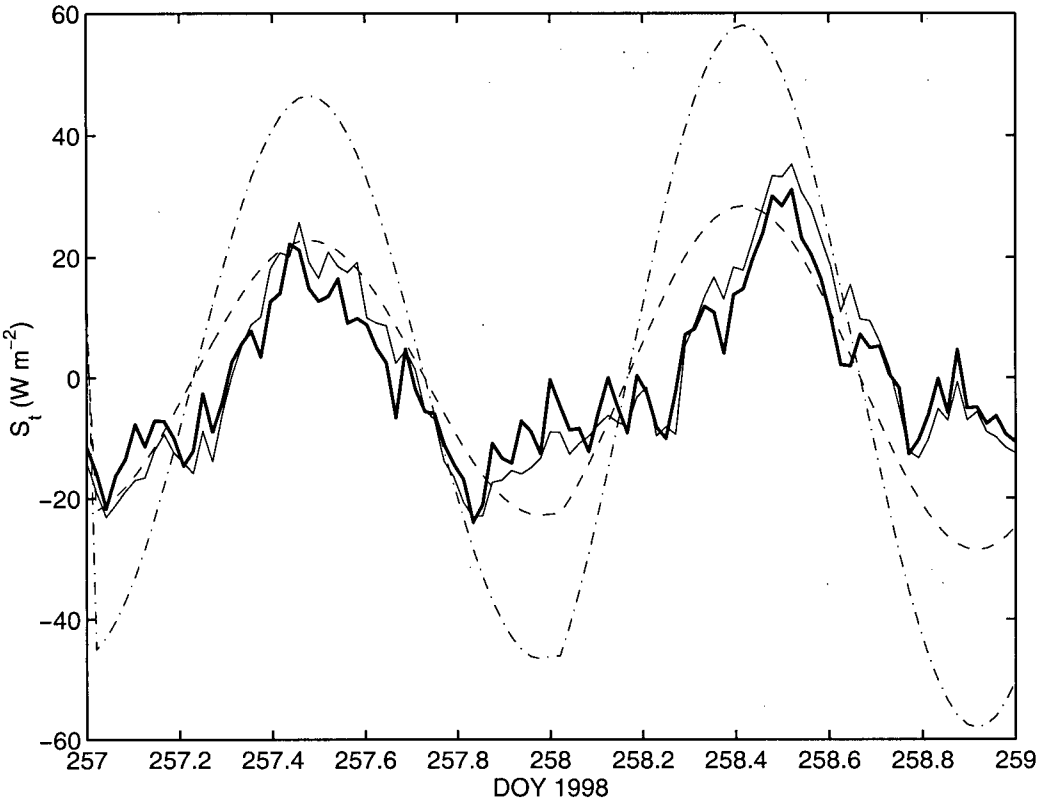


Fig. D.2 Comparison of Herrington's method and the direct method for the calculation of tree heat storage term, $S_t$. Herrington's method with a tree form factor, $F_f = 0.49$ (dashed line) and without (dash-dotted line) is shown with the direct method as outlined in Section 3.5.4 for reference tree #1 (heavy solid line) and for reference tree #2 (thin solid line).

A comparison of Herrington's method and the direct method of calculating tree heat storage is illustrated in Fig. D.2. The stand at the Campbell River site appeared to be well suited to Herrington's method for the calculation of tree bole heat storage once a correction for the taper in the bole was accounted for. This was primarily likely a function of the dense, closed nature of this canopy despite the somewhat too narrow boles for the infinite slab assumption to hold.

## APPENDIX E: CALCULATION OF THE AREA UNDER THE SEMI-LOG PRESENTATION OF COSPECTRAL CURVES

Cospectra were calculated using the method outlined in Section 3.5.1. The resultant frequency range was divided into 85 logarithmically spaced intervals and cospectral estimates ($S_{wx}(n)$) within each interval were bin averaged. The area under the cospectral semilog curve was calculated using the following method,

$$\text{Area} = \int S(n)\, dn$$

$$\text{Area} = \int nS(n) \frac{dn}{n}$$

$$\text{Area} = \int nS(n)\, d\ln n \qquad \text{(E.1)}$$

$$\text{Area} = \sum_{i=1}^{n} \left[ S(n_i)\, \Delta \ln n_i \right]$$

$$\text{Area} = 2.303 \sum_{i=1}^{n} \left[ S(n_i)\, \Delta \log n_i \right]$$

Therefore, when the cospectral curve was normalized by frequency and total covariance ($n\, S_{wx}(n)/\sigma_{wx}^2$), the area under the curve was expected to be 1 and the calculated value would be $1 \div 2.303 = 0.43$ using Equation (E.1).

## APPENDIX F: CALCULATION OF HIGH FREQUENCY FLUX LOSS

The total loss of flux from signal attenuation in the high frequency range may be determined by separating the contributions to the total flux into high frequency and low frequency ranges. This is done for a flux with loss ($\overline{w'\chi'_{w\ loss}}$) and without loss ($\overline{w'\chi'_{w}}$) in the high frequency range,

$$\overline{w'\chi'_{w}} = \overline{w'\chi'_{w\ low}} + \overline{w'\chi'_{w\ high}} \tag{F.1}$$

$$\overline{w'\chi'_{w\ loss}} = \overline{w'\chi'_{w\ loss-low}} + \overline{w'\chi'_{w\ loss-high}} \tag{F.2}$$

where $\overline{w'\chi'_{w}}$ is the total flux partitioned into the low or high frequency range as indicated by the subscripts. It can be assumed that $\overline{w'\chi'_{w\ loss-low}} = \overline{w'\chi'_{w\ low}}$. The difference between Equations (F.1) and (F.2) results in,

$$\overline{w'\chi'_{w}} - \overline{w'\chi'_{w\ loss}} = \overline{w'\chi'_{w\ high}} - \overline{w'\chi'_{w\ loss-high}} \tag{F.3}$$

The proportion of flux attributable to the high frequency range for both situations may be expressed as,

$$a = \frac{\overline{w'\chi'_{w\ loss-high}}}{\overline{w'\chi'_{w\ loss}}} \tag{F.4}$$

$$b = \frac{\overline{w'\chi'_{w\ high}}}{\overline{w'\chi'_{w}}} \tag{F.5}$$

and substituted into Equation (F.3) for,

$$R = \frac{\overline{w'\chi'_{w\ loss}}}{\overline{w'\chi'_{w}}} = \frac{1-b}{1-a} \tag{F.6}$$

such that the underestimation of the $\lambda E$ due to signal attenuation in the sampling tube may be quantified. The percent flux lost is then found as 1 - $R$.

## APPENDIX G: EFFECTS OF HIGH HUMIDITY VS. RAINFALL ON IRGA SIGNAL ATTENUATION

High humidity rather than rainfall was the condition necessary to observe increased slopes in $\chi_w$ power spectra due to $\chi_w$ signal attenuation presumably from adsorption/desorption of water vapour within the sampling tube. Fig. G.1 illustrates the power spectra for $\chi_w$ and $w\chi_w$ cospectra for ideal weather, high humidity and rainfall and high humidity only conditions. Details regarding the first two cases on June 8, 1998 and July 14, 1998 are given in Table 4.1. The high humidity period of October 26, 1998 was composed of 25 half hours during the daytime with mean RH = 100%. During this time, mean $u_* = 0.31$ m s$^{-1}$, u = 1.56 m s$^{-1}$, $\lambda E = 12$ W m$^{-2}$, $H$ = -11 W m$^{-2}$ and $R_a = 41$ W m$^{-2}$. Closure was poor at -12.3% and conditions were stable with $\zeta$ = 0.09.

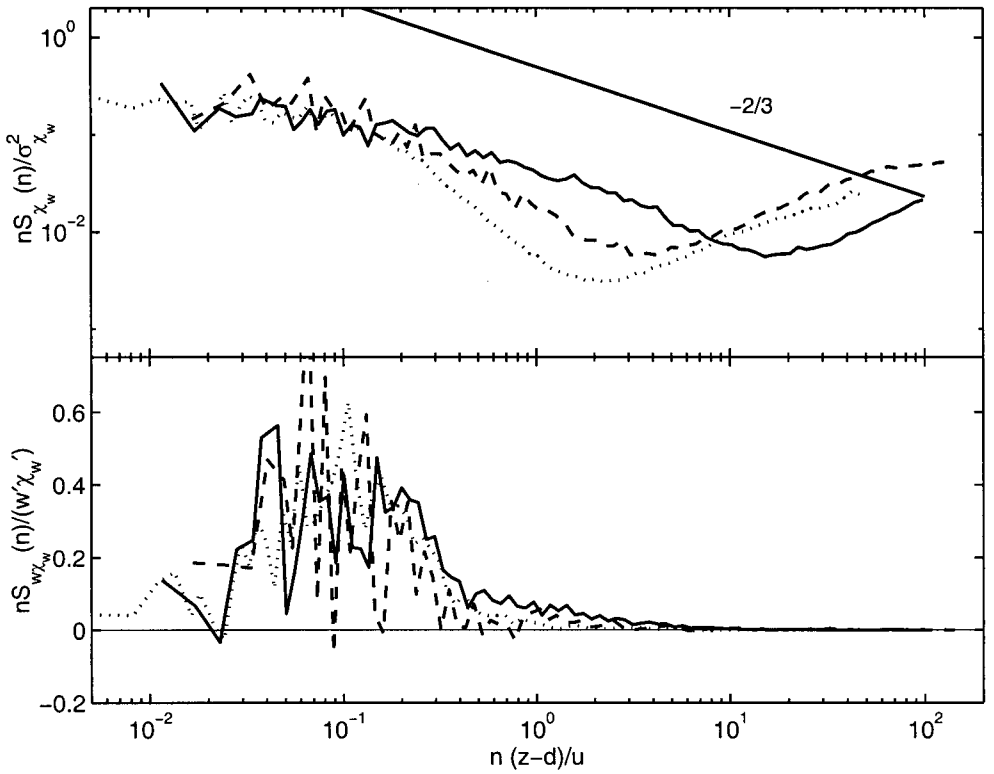


Fig. G.1 Normalized logarithmic power spectra for the water vapour mixing ratio ($\chi_w$) (top panel) and normalized semi-logarithmic cospectra for $w\chi_w$ (bottom panel) measured with a LI-6262 IRGA under daytime conditions experiencing zero rainfall on June 8, 1998 (solid line), heavy rainfall on July 14, 1998 (dotted line) (see Table 4.1) and high humidity with no rainfall October 26, 1998 (dashed line). The expected -2/3 slope is shown for the inertial subrange. The non-dimensional frequency was derived using the mean wind speed for the three conditions recorded during these measurements, 2.26, 4.77, and 1.56 m $s^{-1}$, respectively and the difference between the measurement height and the zero-plane displacement height, $z$ -$d$, 22.2 m.

## APPENDIX H: EFFECTS OF IMPROVED HEATING AND CLEAN TUBING ON IRGA SIGNAL ATTENUATION

On June 9, 1999, the sampling tube and thermostatted box housing the IRGA on the tower was replaced with a new system with clean tubing and improved heating of all components including the sample filter. Note that delay times were reduced to 0.67 s (14 samples) with the equipment replacement. The effects of humidity were shown to be significantly minimized after these changes took place (Fig. H.1). Measurements of $\chi_w$ during ideal weather conditions, conditions experiencing high humidity and rainfall and only high humidity (see Table H.1) were compared with measurements made using the old system during ideal conditions on June 8, 1998 (Table 4.1). Unfortunately, it was difficult to determine from these observations whether improvements in heating or cleanliness of the tubing and filter components were the cause of the improved signals during high humidity conditions.

As suggested by other research groups (Judd, 1995; Smith and Campbell, 1999), dirty tubing may result in significant $\chi_w$ signal attenuation problems. Certainly, in high humidity conditions, dirt particles within the sampling tube would only aggravate the tendency for water vapour to adsorb and desorb on the sampling tube walls. Fig. H.1 does indicate that the sampling tube used for measurements during ideal conditions on June 8, 1998, one year prior to the installation of the new system, was not so contaminated to cause attenuation of the $\chi_w$ signal as compared to measurements during ideal conditions on June 14, 1999.

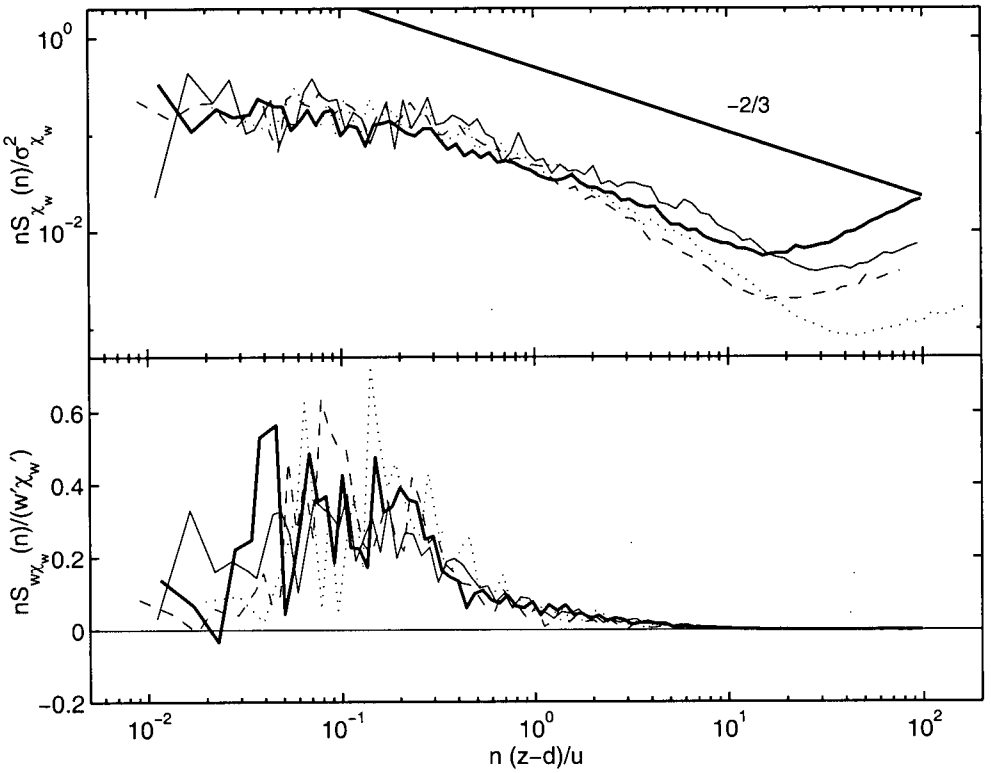


Fig. H. 2 Normalized logarithmic power spectra for the water vapour mixing ratio ($\chi_w$) (top panel) and normalized semi-logarithmic cospectra for $w\chi_w$ (bottom panel). The performance of the LI-6262 with the original sampling tube and thermostatted box under daytime conditions experiencing zero rainfall on June 8, 1998 (heavy solid line) (Table 4.1) is compared with measurements made using a new sampling tube and improved heating system during clear, dry conditions on June 14, 1999 (light solid line), humid, dry conditions on June 28, 1999 (dashed line) and heavy rainfall conditions on June 27, 1999 (dotted line)(Table H.1). The expected -2/3 slope is shown for the inertial subrange. The non-dimensional frequency was derived using the mean wind speed for the three conditions recorded during these measurements, 2.26, 1.98, 2.89, and 1.49 m $s^{-1}$, respectively and the difference between the measurement height and the zero-plane displacement height, *z-d*, 22.2 m.

Table H.2 Mean energy budget, weather conditions and turbulence conditions measured during sessions chosen for spectral analysis after a new sampling tube and improved heating system were installed. Overbars indicate means followed by ± 1 SE. The half hours used for mean spectra calculations ($n$) were recorded during the daytime (when $S\downarrow > 0$).

| Case | Ideal, new tube | High humidity, new tube | Heavy rain, new tube |
|---|---|---|---|
| Study | June 14, 1999 | June 28, 1999 | June 27, 1999 |
| No. of half hours | 5 | 20 | 19 |
| $\overline{P}$ (mm/30 min) | 0.0 ± 0.0 | 0.0 ± 0.0 | 1.38 ± 0.37 |
| $P_{max}$ (mm/30 min) | 0.0 | 0.0 | 3.81 |
| $\overline{u}$ (m s$^{-1}$) | 1.98 ± 0.42 | 2.89 ± 0.10 | 1.49 ± 0.17 |
| $\overline{u_*}$ (m s$^{-1}$) | 0.43 ± 0.09 | 0.61 ± 0.03 | 0.23 ± 0.02 |
| $\overline{\zeta}$ | -0.863 ± 0.181 | 0.006 ± 0.006 | -0.256 ± 0.284 |
| $\overline{\mathrm{RH}}$ (%) | 48.3 ± 1.5 | 97.0 ± 1.0 | 98.6 ± 0.8 |
| $\overline{H}$ (W m$^{-2}$) | 403.8 ± 24.3 | -10.8 ± 4.8 | -3.1 ± 6.4 |
| $\overline{\lambda E}$ (W m$^{-2}$) | 140.7 ± 14.2 | 90.0 ± 5.7 | 66.8 ± 10.0 |
| $\overline{R_a}$ (W m$^{-2}$) | 582.9 ± 23.8 | 113.2 ± 13.7 | 123.4 ± 19.8 |
| $\overline{\left(\frac{H+\lambda E}{R_a}\right)}$ (%) | 91.0 ± 7.8 | 60.0 ± 2.4 | 52.3 ± 5.6 |

## APPENDIX I: EFFECTS OF DELAY TIME ON $w\chi_w$ COSPECTRA

Fig. I.1 illustrates the change in $w\chi_w$ cospectra after digitally lagging the signals from the sonic anemometer by 1.1 s (23 samples). This allows $w$ signal to remain in phase with the $\chi_w$ signal delayed due to the time required for the air streams drawn in through the 4 m of sampling tube to reach the IRGA. In this selection of half hours from the ideal conditions case study on June 8, 1998 (see Table 4.1), little effect due to delay is observed in the low frequency range while the effect becomes significant beyond 0.1 Hz as the $w\chi_w$ cospectral curve becomes negative (see top panel Fig. I.1). This indicates a delay-induced shift in $\chi_w$ fluctuations in the high frequency range resulting in an erroneous negative correlation between $w$ and $\chi_w$. These effects are also evident in the log-log presentation as the $w\chi_w$ cospectra drops from the expected -4/3 slope around the same frequency range (bottom panel Fig. I.1). Similar results have been shown by Laubach and Teichmann (1996) who calculated a 10% loss of flux when the delay time was reduced to 63% of the true value. By calculating the quadrature spectrum, Laubach and Teichmann (1996) illustrated how the phase relation between the two variables changed using various delay times. Underestimated delay times tended to result in a significant negative high-frequency quadrature spectrum confirming the occurrence of an erroneous negative correlation. In general, any delay time error reduces the magnitude of the covariances (Laubach and Teichmann, 1996).

Delay times are computed on a half hour basis by maximizing the cross-correlation between $T$ measured by the sonic anemometer and the scalar in question such as $\chi_w$. An alternate method is to simply maximize the covariance between $w$ and the scalar (Kelliher et al., 1998). By bringing the high frequency $\chi_w$ time series forward by 23 samples (equivalent to 1.1 s), all seven half hourly $\overline{w'\chi_w'}$ from the ideal case study were increased from the original $\overline{w'\chi_w'}$ by 2.21% up to 9.97% with an average increase of 5.33%. This procedure also illustrates how the time delay associated with each half hour tends to vary slightly. However, the final $\overline{w'\chi_w'}$ generally differs by less than 1% as the delay time varies by ± 4 samples (0.2 s).

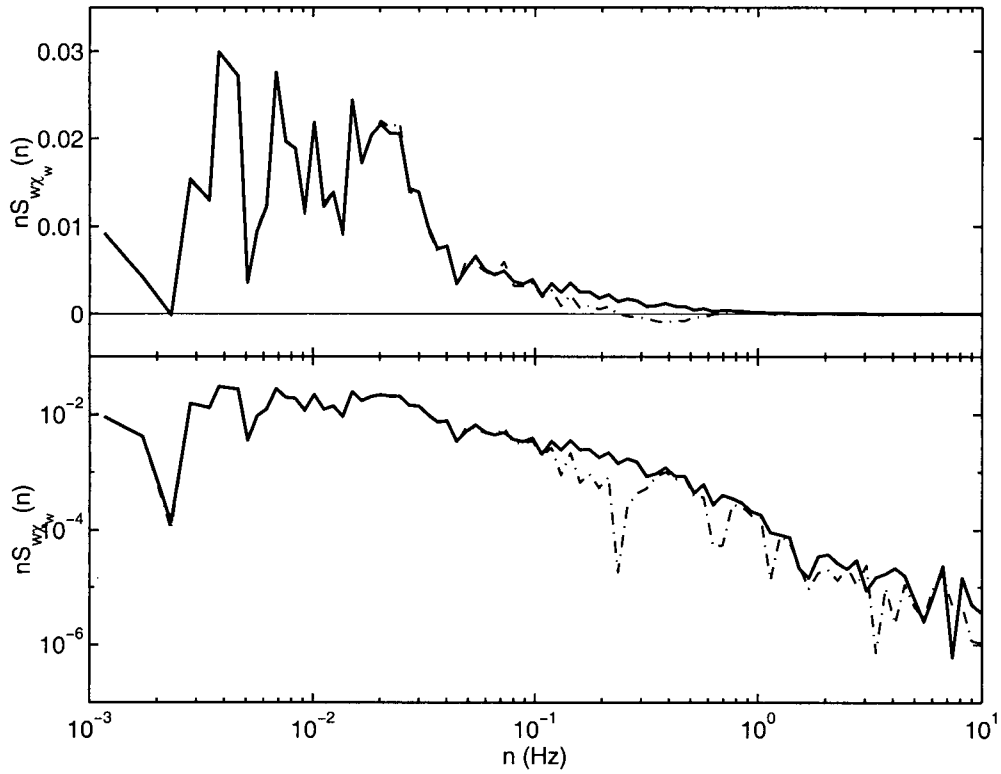


Fig. I.1 $w\chi_w$ cospectra against frequency ($n$) in semilog presentation (top panel) and log-log presentation (bottom panel) demonstrating the effect of delay time. Data is a mean of 7 half hours measured during clear, dry conditions June 8, 1998 between 08:30 h and 14:30 h (ideal case study, see Table 4.1). Cospectra of $w\chi_w$ without the delay time correction (dash-dotted line) illustrate an apparent high frequency loss of flux in contrast to cospectra of $w\chi_w$ with a delay time of 1.1 sec (equivalent to 23 samples) (heavy solid line).